Interactions in waveguide quantum electrodynamics

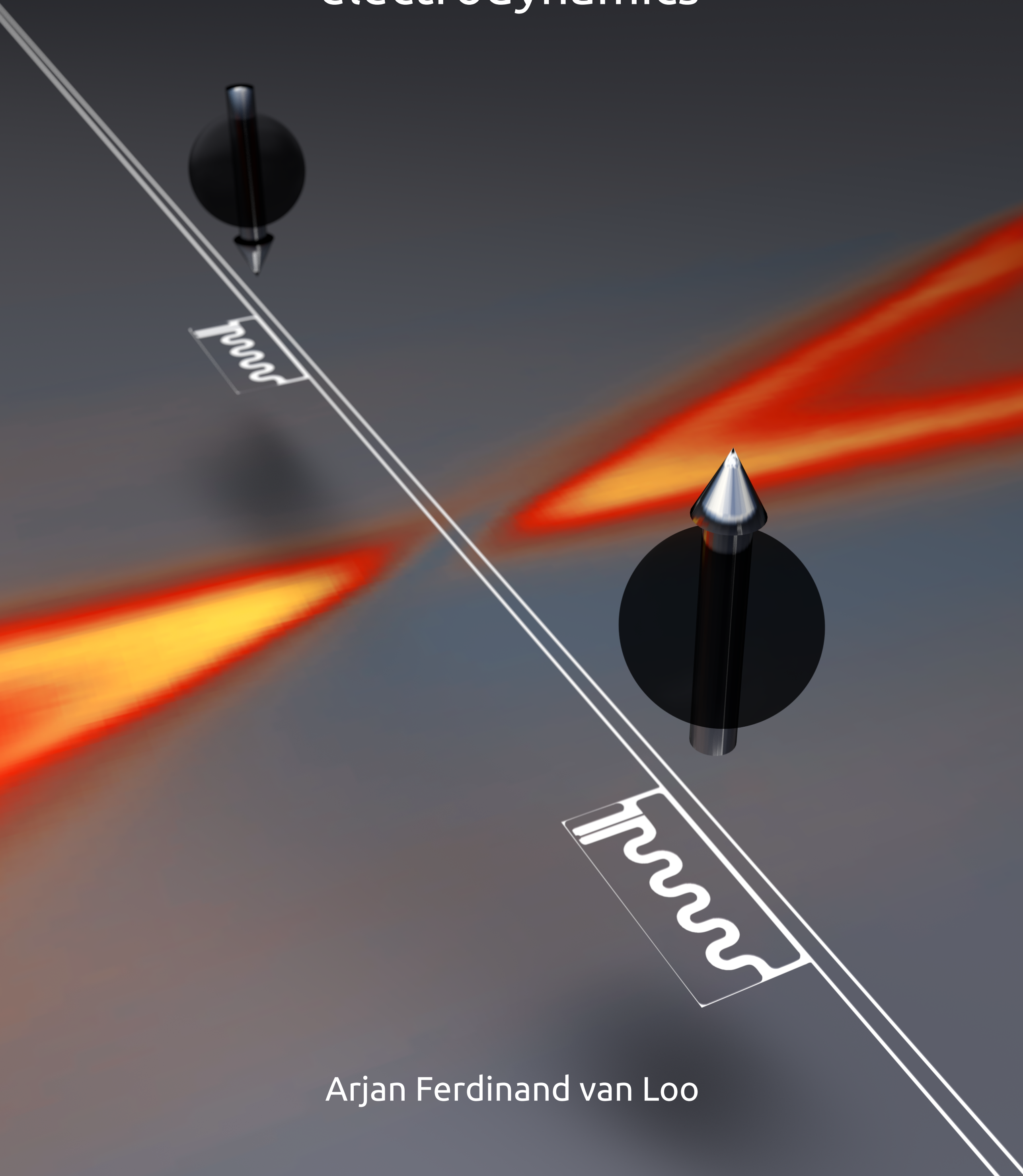

Arjan Ferdinand van Loo

DISS. ETH NO. 21838

Interactions in waveguide quantum electrodynamics

A dissertation submitted to

ETH ZURICH

for the degree of

Doctor of Sciences

presented by

Arjan Ferdinand van Loo

MSc., TUDelft

born July 19, 1984

citizen of the Netherlands

accepted on the recommendation of

Prof. Dr. Andreas Wallraff, examiner
Prof. Dr. Ataç Imamoğlu, co-examiner

2014

Abstract

Superconducting qubits present a completely artificial platform in which quantum behaviour can be investigated. The tunability of the properties of such a system, either in fabrication or in-situ, makes them suitable for a variety of experiments. Research groups around the world are now using superconducting qubits to make steps towards building a quantum computer, to investigate atom-photon interactions, and scientists are starting to use superconducting qubits to simulate other quantum systems.

In this thesis, superconducting transmon qubits are coupled to an open transmission line in order to investigate the coupling of distant qubits via photons, analogous to how distant atoms couple in open space. This research departs from previous experiments on superconducting qubits, in which the qubits where either placed in a resonator, coupling them to a single mode, or in which the qubits were placed in free space and are coupled by being in very close proximity.

First, experiments were done to characterize the properties of a single transmon qubit in an open transmission line. The high reflection coefficient at low drive powers implies a high coupling between the line and the qubit.

When investigating the interactions between multiple qubits, we use the ability to tune the transition frequencies of the qubits as a means to vary the effective distance between the qubits, allowing us to investigate the photon-mediated interactions versus effective distance.

Tuning two qubits into resonance and measuring the elastically scattered radiation, we find no anti-crossing which would be indicative of an exchange interaction, but instead interference patterns that can be replicated by semi-classical models which treat the individual qubits quantum mechanically, but in which all photon-mediated interaction is due to interference.

Using a high-bandwidth analog-to-digital converter and the fast electronics provided by a Virtex-6 FPGA, resonance fluorescence measurements can be performed in order to investigate the spectrum of inelastically scattered radiation. When tuning two qubits into resonance, the spectrum depends on the effective inter-qubit separation. We observe that when the qubits are three quarters of their emission wavelength apart, a low-power resonance fluorescence measurement reveals a level splitting due to an exchange interaction. When the qubits are tuned one wavelength apart, a dark- and a bright state emerge, with the dark state living a factor 100 longer than the bright state. Both phenomena can be understood from intuitive arguments. A quantitative understanding of these phenomena was developed in collaboration with theorists. The theory is based on a master equation, in which the qubit-qubit interactions appear as a second-order effect from qubit-photon interactions. This theory predicts the same interaction phenomena as observed in experiment, and moreover predicts them to be oscillatory in the inter-qubit distance.

Zusammenfassung

Supraleitende Qubits stellen eine neuartige durch Menschenhand geschaffene Möglichkeit dar, um quantenmechanisches Verhalten zu untersuchen. Durch die grosse Auswahl an realisierbaren Eigenschaften solcher Systeme, entweder im Fabrikationsprozess oder durch Parametereinstellung bei ihrer Verwendung, eignen sie sich für eine Vielzahl von Experimenten. Forschungsgruppen rund um die Welt benutzen heutzutage supraleitende Qubits, um erste Schritte in Richtung des Baus eines Quantencomputers zu bewerkstelligen, um Wechselwirkung zwischen Photonen und Atomen zu untersuchen und Wissenschaftler fangen an supraleitende Qubits zur Simulation von anderen Quantensystemen zu verwenden.

In dieser Doktorarbeit wurde eine spezielle Art von supraleitenden Qubits, sogenannte Transmonqubits, kapazitiv an eine Transmissionsleitung für Mikrowellenphotonen gekoppelt. Ziel war die Wechselwirkung zwischen räumlich entfernten Qubits mittels Photonen zu untersuchen, in Analogie zur Untersuchung der Kopplung zwischen Atomen im freien Raum. Dies unterscheidet diese Forschungsarbeit von früheren Experimenten, bei denen die Qubits sich in einer Mikrowellenkavität befanden und mit einer einzelnen Mode des Resonators wechselwirkten oder bei denen die Qubits sich im freien Raum sehr Nahe beieinander befanden und dadurch miteinander gekoppelt wurden.

Erste Experimente wurden durchgeführt um die Eigenschaften eines einzelnen in der Nähe einer Transmissionsleitung realisierten Transmons zu charakterisieren. Der hohe Reflektionskoeffizient des Mikrowellenfeldes in der Transmissionsleitung bei niedriger eingestrahlter Leistung lässt auf eine starke Kopplung zwischen den beiden Systemen aus Qubit und Transmissionsleitung schliessen.

Bei der Untersuchung der Wechselwirkung zwischen mehreren Qubits benutzen wir die Möglichkeit die Übergangsfrequenz der Qubits zu verändern, was einer Veränderung des effektiven Abstands zwischen den Qubits gleichkommt und uns die Möglichkeit eröffnet die durch die Photonen ver-

mittelte Kopplung in Abhängigkeit vom effektiven Abstand zu untersuchen. Wenn die Qubits in Resonanz gebracht werden und wir die elastisch gestreute Mikrowellenstrahlung mittels der Transmissionsleitung messen, finden wir keine anticrossings. Dies wäre ein Indiz für Austauschwechselwirkung zwischen den Qubits. Wir beobachten stattdessen Interferenzmuster, die mit einem semiklassischen Models beschrieben werden können, das die einzelnen Qubits quantenmechanisch, aber die durch die Photonen hervorgerufene Wechselwirkung auf Grund von Interferenz berücksichtigt.

Unter Verwendung eines Analogdigitalwandlers mit hoher Bandbreite und schneller Elektronik, die mit einem Virtex-6 FPGA realisiert wurde, konnten Resonanzfluoreszenzmessungen durchgeführt werden, um das Spektrum der unelastisch gestreuten Mikrowellenstrahlung zu untersuchen. Wenn zwei Qubits in Resonanz gebracht werden, hängt das Spektrum vom effektiven Abstand der Qubits ab. Wir beobachten im Fall eines Qubitabstands von dreiviertel Mal ihrer Emissionswellenlänge bei Resonanzfluoreszenzmessung mit kleiner Mikrowellenleistung eine Aufspaltung der Qubitenergieniveaus auf Grund von Austauschwechselwirkung. Wenn der effektive Qubitabstand auf eine volle Wellenlänge eingestellt wird, tritt ein dark state und ein bright state auf, wobei die Lebenszeit des dark states um den Faktor 100 länger ist, als die des bright states. Beide Phänomene können mittels eines anschaulichen Bildes erklärt werden.

Ein quantitatives Verständnis dieser Phänomene wurde in Zusammenarbeit mit theoretischen Physikern entwickelt. Die theoretische Beschreibung basiert auf einer Mastergleichung, in der die Qubit Qubit Wechselwirkung als ein Effekt zweiter Ordnung der Qubit Photonen Wechselwirkung auftritt. Diese Theorie sagt die gleichen Wechselwirkungsphänomene voraus, die auch im Experiment beobachtet wurden und prognostiziert, dass die Kopplungsstärke oszillierend vom Abstand zwischen den Qubits abhängt.

Contents

1 Introduction 1

1 Introduction

Quantum mechanics is a very capricious theory. Even a century after its foundations were laid, its predictions of how nature behaves at small energy scales continue to confuse and baffle those who learn about it. The difficulties in developing an intuition for the ways of quantum physics are best summarized by David Mermin's answer to the question how to interpret quantum mechanics: 'Shut up and calculate'. However, it turns out that quantum mechanics quickly becomes hard to calculate when the system under consideration is larger than just a few elementary particles.

The fact that nature on small scales behaves so weird that surrealist art looks normal in comparison makes quantum mechanics so interesting to investigate. An example of quantum weirdness is a single particle that is spread out in space, effectively being at many different positions at once, until its position is measured, upon which it will have one fixed position. A second example is that particles in a specific type of state that is called 'entangled' show instantaneous correlated behaviour at a distance, defying the Einsteinian belief that correlations, like information, must travel no faster than the speed of light. However, maybe the biggest philosophical repercussion of quantum mechanics is that it obliterates possibility of a deterministic world. (It is interesting to note that this blow to determinism came almost at the same time as Gödel's incompleteness theorem [Gödel31], which proves that for any sufficiently complete set of axioms forming a logical language, that language will contain statements that cannot be proven to be true or false. This dealt a similarly crushing blow to the philosophy of logic and mathematics.)

Because it is so hard to develop an intuition for quantum mechanics, it is still possible to find an experimental system behaving in a surprising way, even though the fundamental laws are well known. The weirdness of quantum mechanics, and the reluctance of physicists to believe its predictions, are one of the reasons for it remaining an object of intense research.

Theoretically, physicists still hope to find a more satisfying, more understandable theory of nature that shows the same high level of agreement to experimentally observed phenomena as quantum mechanics. This dissatisfaction leads to theoretical investigation towards more intuitive underlying principles from which quantum mechanics would emerge, and to efforts to find other interpretations of the laws of quantum mechanics. On the experimental side, the Bell test [Bell64], which would ascertain that there are no hidden variables that would lead back to a predictable version of nature, is still investigated intensely. So far quantum mechanics has always been proven right by experimental Bell tests, but no test has been done that closes all possible loopholes. Thus, performing a loophole-free Bell test remains a holy grail in experimental quantum physics.

1.1 Quantum two-level systems

Another motivation for experimentally investigating quantum mechanics is that it presents the ultimate challenge in engineering. Inspired by the famous words of Feynman: “There is plenty of room at the bottom”, uttered during a lecture Caltech in 1959, physicists, both theoretical and experimental, have been trying to get closer to controlling single atoms and photons, have been investigating how they interact, and have been trying to engineer quantum systems with well-defined interactions. The simplest quantum system to study is a two-level system. These systems are called quantum bits, or qubits for short, and are the quantum-mechanical counterpart of the classical two-valued bit. Some properties of qubits are rather different from classical bits. For example, whereas a classical bit can have the value 1 or 0, the qubit can hold both of these values at once (called a superposition state), but it can for example have ’more’ of the value 0 than 1. All possible states of a qubit can be described by

$$|\psi\rangle = \alpha|0\rangle + \beta|1\rangle, \tag{1.1}$$

where α and β are complex numbers with $|\alpha|^2 + |\beta|^2 = 1$. The state of a qubit can be visualized as a position on a sphere, as shown in Fig. 1.1. Another difference between classical and quantum bits is how the information scales with the number of bits. A system of n qubits can be in a superposition of 2^n different states. That means that to describe such a state, we would need 2^n complex numbers. Since the number of atoms in the

universe is estimated to be smaller than 2^{500}, a 500-qubit memory contains more information than any conceivable classical memory could store, not even if we were able to store one complex number on each atom in the universe. These are not the only differences between a classical and a quantum bit, but rather than giving a grossly oversimplified and incomplete account here, we refer the reader to the excellent introduction given in [Nielsen00].
Quantum two-level systems come in many different shapes, with many different properties. A few examples of qubits under intense investigation are so-called photonic qubits, where the properties of a photon implement a qubit [Kok07], quantum dots, where a single electron spin is trapped in a small volume in a 2-dimensional electron gas, carbon nanotube or nanowire, defined by an applied electrostatic potential [Hanson08], ions trapped in a field, cold atoms trapped in a periodic potential [Ritsch13], or nitrogen-vacancy centers in diamonds [Doherty13]. The latter example exhibits the extraordinary property of maintaining the coherence of its qubits for significant amounts of time even at room temperature. Finally, in this work we will be concerned with superconducting circuits that behave like a qubit [Clarke08].

Superconducting qubits make use of the fact that electrons in a superconductor pair up into Cooper pairs, which are bosons. These bosons condense into a single ground state, a phenomenon known as Bose-Einstein condensation. The collective of all Cooper pairs can be described by a single wave-function, characterized by the order parameter φ [Tinkham96]. It is because of this extraordinary property of superconductors that a macroscopic device can behave quantum-mechanically as a two-level system. Because these qubits are implemented as man-made circuits, the properties of the qubits can be adapted to fit specific experiments, giving the experimenter an amount of control over the experimental system which is absent in other qubit technologies.

The research done with qubits (of any type) is mainly focused on three goals: quantum computing, quantum simulations, and quantum optics. A short introduction to each of these is presented below.

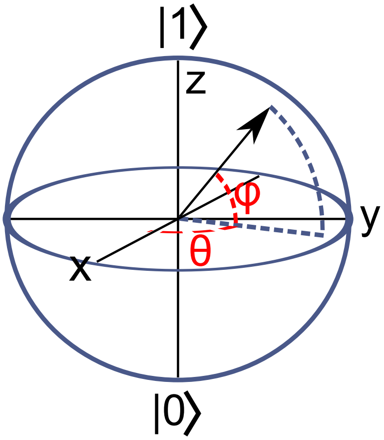

Figure 1.1: The state of a qubit can be visualised as a unit vector pointing from the center of a sphere to any position on its surface. The coordinates, here chosen to be θ and φ determine the qubit state.

1.1.1 Quantum computing

In quantum computing, the strange behaviour of quantum mechanics – such as the ‘spooky action at a distance’ Einstein did not believe in, causing him to construct the thought experiment known as the EPR paradox [Einstein35] – is harnessed to perform certain computations much more efficiently than classical computers. The most famous example of this is Shor’s algorithm [Shor97], which causes an exponential speedup in finding the prime factors of a number compared to present-day algorithms running on classical computers. Getting Shor’s algorithm to work on a quantum computer is a highly relevant goal, as current encryption technologies are based on the fact that classical computers are inefficient at calculating prime factors. A sufficiently large quantum computer running Shor’s algorithm could break current encryption methods, rendering online banking unsafe, and making online privacy even more questionable than it already is. However, to run such an algorithm is a huge challenge as it needs thousands of qubits with low information loss. It is believed that error correction will have to be implemented to make running Shor’s algorithm a possibility.

Current state-of-the-art quantum computing experiments use just a few qubits. It seems, therefore, that running a technologically relevant version of Shor's algorithm will need much improvement in quantum computing technology.

Other quantum algorithms include a database search known as Grover's algorithm [Grover96] and an algorithm to solve systems of linear equations [Harrow09]. Another very interesting new possibility is the recent work done on quantum machine learning [Lloyd13, Rebentrost13], which could warrant privacy in large databases – users would be able to obtain information about patterns in the database without having access to specific details. For example, a database storing DNA would allow users to access the prevalence of certain pieces of genetic code without allowing access to the DNA of any individual. This application of quantum technology is made more appealing by the fact that it would need only tens of qubits for its implementation, and therefore presents a goal much closer to the cutting edge of quantum technology than implementing Shor's algorithm for encryption-sized primes. However, which things can be done using a quantum computer and which cannot is very much an open question, and it is expected that many more quantum algorithms will be found.

The computing power of a quantum computer compared to a conventional computer is however still unknown, and of great interest to computer scientists. The quantum computer can efficiently factor numbers, which is a problem in complexity class NP (problems which cannot be solved efficiently, but of which the solutions can be efficiently checked), and which can hence not be efficiently solved on classical computers with current-day algorithms. This does not prove that the quantum computer is more powerful than its classical counterpart as it is hard to prove that no classical algorithms exist that are also able to efficiently factor numbers. Another complexity class is NP-complete. If a solution is found for any NP-complete problem, that solution can be adapted to solve all other problems in NP. It is hoped that a quantum algorithm will be found that can solve an NP-complete problem. A famous example of a problem in the NP-complete class is the travelling salesman problem.

Another interesting computer science question that could be solved by a quantum computer is as follows: classical computers can efficiently solve the class of BPP problems (problems that can be solved in polynomial time to a limited precision). This class is a subset of the larger complexity class PSPACE, which comprises problems that can be solved by a finite-sized computer in unlimited time. It remains an open question whether the size of these complexity classes is actually different. We define a third complexity class which we call BQP, which contains the class of problems efficiently solvable on a quantum compute. It is known that BQP must lie within BPP. If quantum computers are in fact more powerful than classical computers, this would imply that BQP $>$ BPP, and therefore that BPP $\neq$ PSPACE. The equality of these two complexity classes is a long-standing open question in computer science. For a more complete overview of quantum computing and some of the most famous algorithms, see [Nielsen00].

1.1.2 Quantum simulation

Using quantum systems to simulate other quantum systems is an idea famously coined by Feynman [Feynman82]. Since it is very hard to calculate anything about a quantum mechanical system involving more than just a few atoms or photons using classical computers, the idea is to instead use quantum mechanical systems over which we have some amount of control for simulating other quantum systems which are less accessible. The original proposal of Feynman mentioned the simulation of field theories using spins in a solid state system. A more recent proposal [Jordan12] contains such an algorithm, and predicts future algorithms simulating the standard model of physics.

1.1.3 Quantum optics

The field of quantum optics focuses on the interaction between light and matter, and is studied using a myriad of systems such as cavity QED, quantum dots, NV-centers and more recently superconducting qubits. Qubits, consisting of only two levels, can be seen as the most simple version of an atom. When using an artificial system such as a superconducting qubit, qubits are therefore sometimes called artificial atoms. Artificial atoms or qubits, like natural atoms, absorb and emit radiation at the same energy as the energy difference between its ground state and excited state. As such, artificial atoms present a fully engineered system with which the fundamental interactions between light and matter can be investigated. In this thesis, we will focus on research in this direction. More explicitly, we will be investigating the interaction of two of these artificial atoms which are placed some distance apart in a one-dimensional space.

Performing quantum optics experiments using superconducting qubits is a relatively new trend, which started with strongly coupling a qubit to a resonator [Wallraff04]. The strength of the interaction between microwave photons and a superconducting qubit opens up a range of experiments not easily done with other qubit technologies. Moreover, the availability and maturity of radio-frequency technology due to its prevalence in industry has been a great boon to the development of experiments in microwave quantum optics and quantum computing.

Since the demonstration of strong coupling between a superconducting qubit and microwave photons, examples of quantum optics experiments using superconducting qubits include the observation of the Lamb shift [Fragner08], investigating the statistics of microwave photons [Bozyigit11, Eichler11], performing the Hong-Ou-Mandel experiment at microwave frequencies [Lang13], shaping microwave photons [Pechal13, Srinivasan13], and observing resonance fluorescence and electromagnetically induced transparency for a qubit coupled to a transmission line [Astafiev10a, Abdumalikov10].

1.2 Josephson junctions

In order to make a qubit, it is imperative to be able to address two specific energy levels of a quantum system selectively. Therefore, the system needs to be nonlinear, such that its eigenenergies exhibit an anharmonic structure. In superconductors, such a nonlinearity is readily available in the Josephson junction.

In 1962, Josephson predicted that a superconductor interrupted by a non-superconducting layer has the following zero-voltage current [Josephson62].

$$I_s = I_c \sin\varphi, \tag{1.2}$$

in which I_c denotes the critical current – the maximum supercurrent the Josephson Junction can sustain – and φ is the gauge-invariant phase difference across the junction. He also predicted that the relation between the phase difference over such a Josephson junction is related to the voltage by:

$$\frac{d\varphi}{dt} = \frac{2eV}{\hbar}. \tag{1.3}$$

The energy building up in the junction due to the transport through it is then calculated by using equation (1.2) and (1.3) as:

$$E_{jj} = \int_0^t I_s V dt = \frac{\hbar I_c}{2e} \int_0^t \sin\varphi \frac{d\varphi}{dt} dt = \frac{\hbar I_c}{2e}(1 - \cos\varphi), \qquad (1.4)$$

where the value of the integration constant was determined by the assumption that no energy should be stored in the junction when there is no phase difference across it. The prefactor $\hbar I_c/2e$ is also known as the Josephson energy E_J.

If a voltage develops over a junction, equation (1.4) is not enough to describe the physics of it. To understand the transport through a realistic Josephson junction, the so-called RCSJ model is used. The acronym stands for 'resistively and capacitively shunted junction', which is exactly what the model entails. The direct transport through the weak link is modeled as a resistive transport path parallel to the ideal junction, while the superconducting leads on both sides of the non-superconductor form a capacitor (Fig. 1.2). In the case of aluminium / aluminium-oxide / aluminium S-I-S junctions – which will be the junctions used for the experiments presented here – the value of the resistor, which determines the amount of dissipation in the junction, can be approximated to be infinite. These junctions

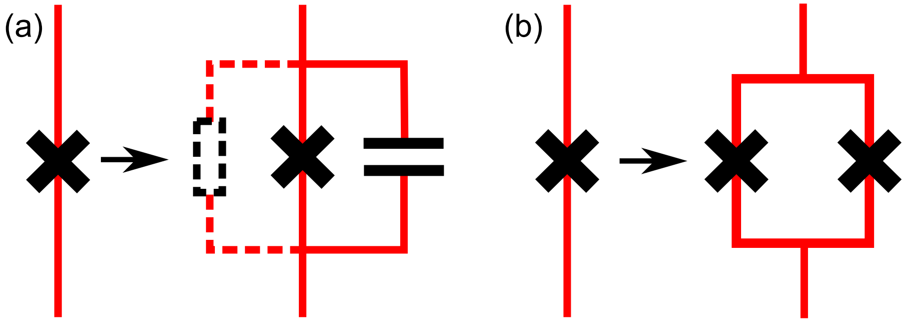

Figure 1.2: (a) A realistic Josephson junction is described by the RCSJ model: transport through it is equal to transport through an ideal junction, a resistor and a capacitor in parallel. (b) Two Josephson junctions in parallel create a superconducting quantum interference device or SQuID.

are then described by an ideal junction placed in parallel to a capacitor. The energy developed by the capacitor when a voltage is applied over the junction is described by:

$$E_{cj} = \frac{1}{2}CV^2 = \frac{C}{2}\left(\frac{\hbar}{2e}\right)^2 \dot{\varphi}^2 = \frac{C}{2}\left(\frac{\Phi_0}{2\pi}\right)^2 \dot{\varphi}^2, \tag{1.5}$$

where the dot on the φ denotes taking the time derivative, and $\Phi_0 \equiv h/2e$ is the flux quantum. For more on Josephson junctions, an excellent treatment is given in [Tinkham96].

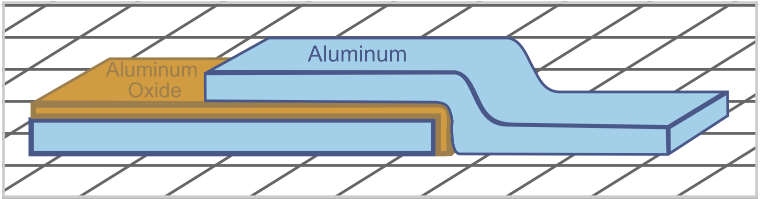

Figure 1.3: A Josephson junction can be created by shadow evaporation: a layer of aluminium is evaporated onto a substrate (the grid in this figure) through a mask. The aluminium is allowed to oxidize for a controlled time. The angle of evaporation is changed before evaporating a second layer of aluminium, creating a displacement between the two layers leading to a partial overlap. This results in a superconductor-insulator-superconductor interface in which Cooper pairs tunnel through the insulator.

1.3 Superconducting quantum interference devices

We will now give a short introduction to superconducting quantum interference devices or SQuIDs (we will drop the capitals in the following). A squid consists of two junctions in parallel (Fig. 1.2b). The transport in a squid can be divided into a circular current and a current through the squid:

$$I_{sq} = I_c(\sin\varphi_1 + \sin\varphi_2) \qquad I_{cir} = \frac{I_c}{2}(\sin\varphi_1 - \sin\varphi_2), \tag{1.6}$$

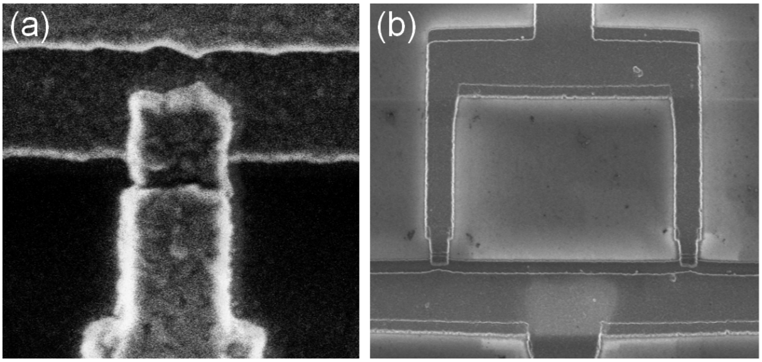

Figure 1.4: Scanning electron microscopy images for (a) a Josephson junction and (b) a superconducting quantum interference device or squid. Images courtesy of Arkady Fedorov.

where we assume the junctions to be identical. We can now use the fact that the flux through the loop is quantized: the circulating current acts to shield some of the flux through the squid loop such that the remaining net flux is an integer amount of flux quanta. When the self-inductance of the loop can be neglected, this can be written as $\varphi_1 - \varphi_2 = 2\pi\phi/\Phi_0$ with ϕ the flux through the loop. Applying this to (1.6) results in new expressions for the current through the squid:

$$\begin{aligned} I_{sq} &= 2I_c \cos(\pi\phi/\Phi_0)\sin(\varphi_1 - \pi\phi/\Phi_0) \\ I_{cir} &= I_c \sin(\pi\phi/\Phi_0)\cos(\varphi_1 - \pi\phi/\Phi_0), \end{aligned} \tag{1.7}$$

from which we see that the maximum current through the squid is given by

$$I_{sq,max} = 2I_c \left|\cos\left(\frac{\pi\phi}{\Phi_0}\right)\right|. \tag{1.8}$$

Comparing these relations to the equations describing a Josephson junction, we see that the squid is equivalent to a Josephson junction with a flux-tunable critical current.

1.4 Superconducting qubits

Having the Josephson Junction as a nonlinear element, it is possible to build various types of superconducting qubits, such as phase qubits, flux qubits

[Orlando99], charge qubits [Büttiker87] and the closely related transmon qubits [Koch07], and more recently fluxonium qubits [Manucharyan09]. A good treatise describing several of these qubits is given in [Wendin05]. Here, we will be dealing with the transmon qubit which is a special type of Cooper pair box. Hence, the Cooper pair box will be introduced first, after which the transmon regime will be explained.

1.4.1 Cooper pair box

For the experiments we will be discussing, the transmon qubit was used. To understand the transmon qubits, we first need to understand the Cooper pair box qubit. The Cooper pair box was one of the earliest qubits, being proposed in 1987 [Büttiker87], and first measured in 1998 [Bouchiat98]. In this section we will introduce the Cooper pair box, and in the next section we will discuss the transmon regime.
The simplest version of the Cooper pair box consists of a voltage source connected in series to a capacitor and a Josephson junction (see Fig. 1.5a). A charge island is formed between the junction and capacitor. For a system consisting of a capacitor and a junction, the Kirchhoff laws dictate that the currents arriving at the island must add up to zero. We equate the current due to the capacitors $I = \dot{Q} = C_J\dot{V}$ with the current due to the junction

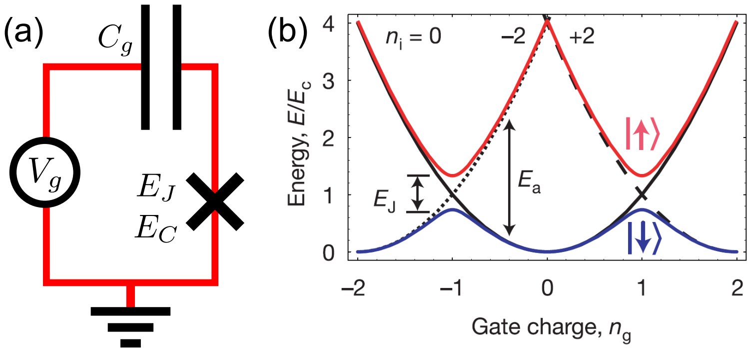

Figure 1.5: (a) Simplified schematic of a Cooper pair box. (b) Energy level diagram from the first two levels of a Cooper pair box. Figure from [Wallraff04].

(1.2), and write the variables into flux using (1.3) and $\phi = \varphi \frac{\Phi_0}{2\pi}$ to get:

$$I = \frac{d}{dt}Q = C_J \ddot{\phi} = -I_c \sin\left(\frac{2\pi\phi}{\Phi_0}\right). \tag{1.9}$$

We have assumed the voltage due to the voltage source to be constant. It should be kept in mind here that the charge on the island is quantized as we are dealing with Cooper pairs in a superconductor ($Q = 2eN$, $N \in \mathbb{Z}$). We compare (1.9) with the Euler-Lagrange equation

$$\frac{\partial}{\partial t}\frac{\partial L}{\partial \dot{x}} = \frac{\partial L}{\partial x}, \tag{1.10}$$

where x is the canonical coordinate of choice. Here, we choose to use the flux ϕ as a canonical coordinate. The shape of (1.10) strongly resembles the two rightmost terms in (1.9). Integrating (1.9) according to (1.10), we find the Lagrangian of this system.

$$L = \frac{C_J \dot{\phi}^2}{2} + I_c \frac{\Phi_0}{2\pi} \cos\varphi. \tag{1.11}$$

In this integration, we can introduce an extra term which is constant in order to take the electrostatic energy due to the constant voltage V_g from the voltage source into account. The energy stored in the capacitor due to this voltage is equal to $C_g(V_g - V)^2/2$, where V is the voltage over the junction, equal to $\dot{\phi}$. This alters the Lagrangian to read

$$L = \frac{C_\Sigma}{2}\left(\dot{\phi} - \frac{C_g}{C_\Sigma}V_g\right)^2 + I_c \frac{\Phi_0}{2\pi}\cos\varphi, \tag{1.12}$$

with $C_\Sigma = C_J + C_g$. We can then find the canonical momentum conjugate to ϕ:

$$\frac{\partial L}{\partial \dot{\phi}} = C_\Sigma \dot{\phi} - C_g V_g = Q = 2eN_{tot}, \tag{1.13}$$

with Q the charge on the island, and N_{tot} the total number of charges on the island $N_{tot} = N - N_g$, with N_g a constant amount of charge caused by the voltage source. The Hamiltonian of the system is given by:

$$\hat{H}_{CPB} = \sum \frac{\partial L}{\partial \dot{\phi}}\dot{\phi} - L = \frac{C_\Sigma}{2}\dot{\phi}^2 + \frac{C_g}{2}V_g^2 - \frac{I_0\Phi_0}{2\pi}\cos(\hat{\varphi}). \tag{1.14}$$

We can rewrite $\dot{\phi}$ in terms of Q, the conjugate variable to ϕ, as $\dot{\phi} = (Q + C_g V_g)/C_\Sigma$. Using this, the Hamiltonian becomes:

$$\hat{H}_{CPB} = \sum \frac{\partial L}{\partial \dot{\phi}} \dot{\phi} - L = \frac{1}{2C_\Sigma} (Q + C_g V_g)^2 - \frac{I_0 \Phi_0}{2\pi} \cos(\hat{\varphi}), \tag{1.15}$$

where we have used the fact that it is allowed to add a constant term to a Hamiltonian, and have added a term $-C_g V_g^2/2$. We now define $E_C \equiv (e)^2/2C_\Sigma$, the energy needed to move a charge across a capacitor, and use that the energy associated with moving a Cooper pair across a junction is $E_J = \frac{I_c \Phi_0}{2\pi}$. Furthermore, we use the relation between $\dot{\phi}$ and N to write the charge part of the Hamiltonian as a function of N, and define the charge number due to the gate voltage as $N_g \equiv -C_g V_g/2e$. These modifications alter the expression for the Hamiltonian to read

$$\hat{H}_{CPB} = 4E_C(\hat{N} - N_g)^2 - E_J \cos(\hat{\varphi}). \tag{1.16}$$

We can impose the usual commutation relation. We rewrite the commutation relation into the variables N and φ, the number of Cooper pairs on the island and the phase across the junction

$$[\hat{\phi}, \hat{Q}] = i\hbar \rightarrow [\hat{\varphi}, \hat{N}] = i. \tag{1.17}$$

To find the eigenenergies of this system, we have to solve

$$\hat{H}_{CPB}|n\rangle = E_k|n\rangle. \tag{1.18}$$

Before discussing the solutions of (1.18), we discuss a useful modification of the Cooper pair box qubit. This modification is to use a squid instead of a single junction. Replacing the junction in our equation with squids is a simple procedure, as a squid loop with two identical junctions is equivalent to a single junction with a flux-dependent Josephson energy $E_J(\phi) = E_{J,max}|\cos(\pi\phi/\Phi_0)|$, with $E_{J,max} = 2E_{Js}$, E_{Js} being the single-junction Josephson energy. A Cooper pair box thus modified is sometimes referred to as a ‘split Cooper pair box’. As can be seen from (1.13), the number and phase operators have a similar relation to each other as the position and momentum operator of a quantum oscillator. It might therefore not be surprising to find that the number operator in the phase basis can be expressed as

$$\hat{N} = -i\frac{\partial}{\partial \hat{\varphi}}, \tag{1.19}$$

similar to the usual momentum operator in the position basis. The eigenvalue problem to be solved to find the spectrum of the Cooper pair box (1.18) is then defined by multiplying Schrödinger's equation from the left by $\langle\varphi|$

$$E_n\langle\varphi|n\rangle = \langle\varphi|\hat{H}_{CPB}|\hat{n}\rangle \rightarrow$$
$$E_n\psi_n(\varphi) = \left(4E_C\left(-i\frac{\partial}{\partial\hat{\varphi}} - N_g\right)^2 - E_J(\hat{\phi})\cos(\hat{\varphi})\right)\psi_n(\varphi), \quad (1.20)$$

with $\psi_n(\varphi)$ the wavefunction of eigenstate n in the phase basis. This differential equation has a known solution in the Mathieu equations (for details, see [Cottet02]), which provides us both with the eigenenergies E_n and wavefunctions ψ_n.

Although the phase basis allows for analytically solving the Hamiltonian, the charge basis is more intuitive to look at, and relatively easy to calculate numerically. The eigenvalue problem can now be stated as $\hat{N}|n\rangle = N|n\rangle$, where we remember that N denotes the number of Cooper pairs on the island, which is quantized ($N \in \mathbb{Z}$). As usual, the states of canonical momenta are related to each other by Fourier transform

$$|n\rangle = \frac{1}{2\pi}\int_0^{2\pi} \mathrm{e}^{-i\hat{N}\hat{\varphi}}|\varphi\rangle d\varphi, \quad (1.21)$$

from which it follows that

$$\mathrm{e}^{\pm i\hat{\varphi}}|n\rangle = |n \mp 1\rangle. \quad (1.22)$$

The Cooper pair box Hamiltonian can then be written completely in the charge basis as

$$\hat{H}_{CPB} = \sum_N \left(4E_C(N-N_g)^2|n\rangle\langle n| - \frac{E_J}{2}(|n\rangle\langle n+1| + |n+1\rangle\langle n|)\right). \quad (1.23)$$

The first few eigenenergies are plotted in Fig. 1.5b as a function of the tunable gate charge N_g. The transition energy is seen to depend strongly on the offset charge N_g. This means that charge fluctuations will strongly influence the qubit. The sensitivity of the Cooper pair box to charge noise is a problematic property when trying to build a quantum computer. However, when tuning N_g to integer numbers, $\partial E/\partial N_g \to 0$ so that at these points the qubit is insensitive to small changes in N_g to first order. The Cooper pair box is therefore often operated at this point, colloquially known as its sweet spot. At the sweet spot, the transition energy of the qubit is minimal and equal to E_J. When a split Cooper pair box is used, this minimal transition energy can be varied by changing the flux through the squid loop.

1.4.2 The transmon regime

The transmon qubit is a Cooper pair box which is modified by placing a capacitor in parallel to the squid loop (Fig. 1.6). This changes the ratio between E_J and E_C [Koch07]. The Hamiltonian for the system does not change, except that in the expression for E_C the capacitor term is replaced by the equivalent combination of the capacitors in parallel to the junction. The effect of changing this ratio is shown in Fig. 1.7. The change in transition energy due to a change in offset charge (the charge dispersion) decreases exponentially with increasing ratio of E_J/E_C, making the transmon very insensitive to charge noise at E_J/E_C ratios of the order of 50. The transition energy of the transmon then only depends on the flux through the squid loop. For transmon qubits, which have a high ratio of E_J/E_C due to the extra capacitor, the energy levels can be approximated by

$$E_{ge} \approx \sqrt{8E_C E_{J,max} \left|\cos\left(\frac{\pi\phi}{\Phi_0}\right)\right|} - E_C. \tag{1.24}$$

This comes at the cost of anharmonicity, which increases algebraically with E_C/E_J. Typical numbers for the anharmonicity (defined here as $\omega_{ef} - \omega_{ge}$, with g, e and f denoting the ground, first excited and second excited state respectively) are around 300 MHz, much smaller than typical transition frequencies, which are usually in the GHz range. This means that if we want to use this system as a qubit, only addressing the lowest two energy states, we have to take special care not to drive the transition between the first and second excited state. This sets a limit on the frequencies that can be involved in coherently driving qubit transitions. Much effort has been put into finding pulse shapes that minimize the loss of information about the qubit state due to the presence of higher levels, with the most commonly used pulse shape being the DRAG-Gauss pulse described in [Motzoi09].

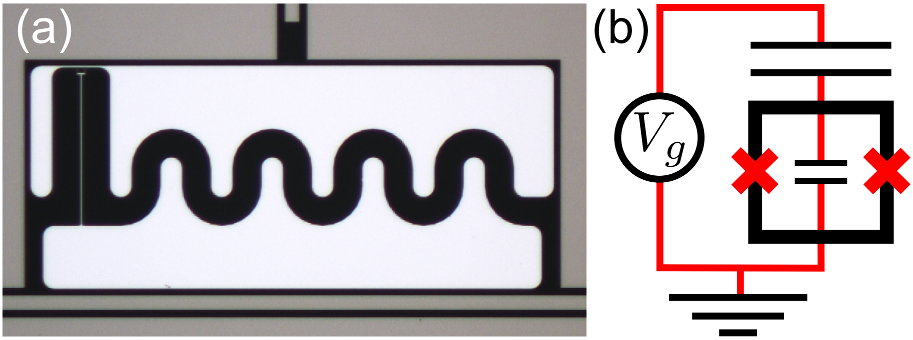

Figure 1.6: (a) An optical microscope picture of a recent transmon design. In recent transmon designs, the capacitor gap size was increased to reduce the field density between the capacitor plates, which is hoped to decrease coupling of the field to two-level fluctuators. (b) The circuit diagram of a transmon qubit is almost identical to that for a split Cooper pair box, except for the large capacitor in parallel to the squid.

1.4.3 The two-level approximation

When talking about quantum bits, we inherently imply that our quantum system has two levels. As we have discussed, the transmon is only weakly anharmonic, and therefore care needs to be taken to stay in the subsystem spanned by its lowest two eigenenergies. If we are sufficient careful such that we can ignore the presence of higher levels, we can use a more elegant description for the transmon qubit

$$\hat{H} = \frac{\hbar\omega_{ge}}{2}\hat{\sigma}_z, \tag{1.25}$$

where the Larmor frequency ω_{ge} is given by (1.24).

1.5 A qubit in a resonator – the Jaynes-Cummings model

To use a transmon for experiments, we have to be able to address it and read it out. The most used method for that is to place it in a coplanar

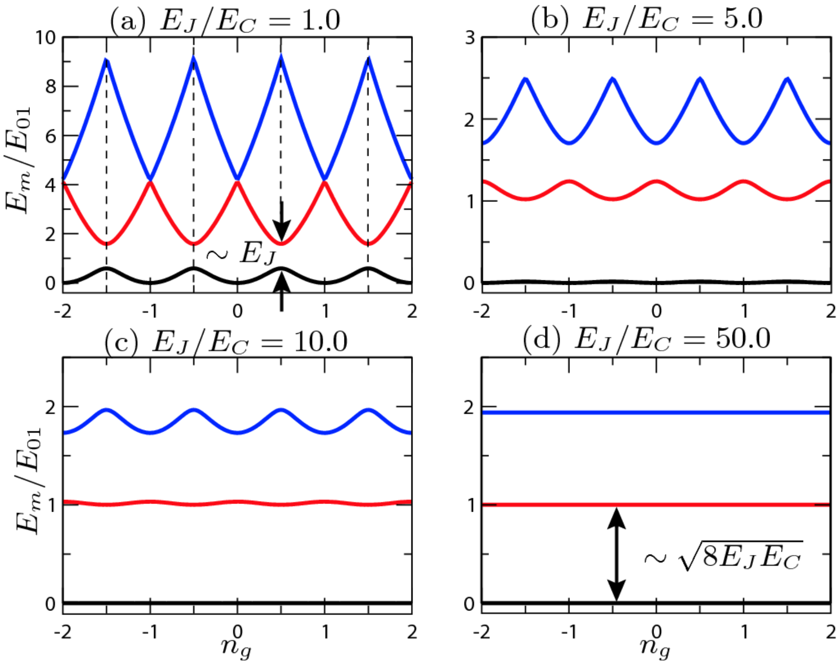

Figure 1.7: The first three energy levels of a transmon qubit for different ratios of E_J/E_C. The change in in transition frequency as a function of charge goes down exponentially with increasing E_J/E_C, while the anharmonicity decreases algebraically. The image is from [Koch07].

waveguide resonator (coplanar waveguide transmission lines will be introduced in 3.1.1). The resonator, formed by interrupting the center conductor of a coplanar waveguide transmission line in two places (see 1.8a), supports only modes of light at integer multiples of its fundamental frequency, which is set by its spatial dimensions. This allows for coupling a qubit to a single mode of light via dipole coupling. This system is a completely man-made analogue to cavity quantum electrodynamics (cavity QED) [Haroche89], where an atom (or multiple atoms) are strongly coupled to a single mode of light contained by a high-finesse cavity. This artificial analogue, where both the cavity and the atoms are replaced by superconducting circuits, is called circuit QED. The coupling between a single mode of light and a two-level system is of great fundamental interest, and due to the relative simplicity of the system it can be described very elegantly by the Jaynes-Cummings Hamiltonian [Jaynes63]:

$$\hat{H}_{JC} = \frac{\hbar\omega_{ge}}{2}\hat{\sigma}_z + \hbar\omega_r\left(\hat{a}^\dagger\hat{a} + \frac{1}{2}\right) + \hbar g\left(\hat{a}^\dagger\hat{\sigma}^- + \hat{\sigma}^+\hat{a}\right), \tag{1.26}$$

where ω_{ge} is the transition frequency of the atom or qubit (we will use the terms 'atoms' and 'qubits' interchangeably here for quantum two-level systems) and ω_r is the resonator frequency. $\hat{\sigma}^+$ and $\hat{\sigma}^-$ denote the atomic raising and lowering operators, and $\hat{a}$ and $\hat{a}^\dagger$ the photonic annihilation and creation operators, respectively. g denotes the coupling strength between the atoms and photons. In the last term we see that if the coupling between the photons and the atom is not zero, a photon can be absorbed resulting in the atom being excited, and that the atom can relax from the excited state resulting in the creation of a photon.

Another advantage to placing the qubit in a coplanar waveguide is that its electrodynamic environment is dominated by the resonator mode. The noise in the transmission line which is not at the frequency of the resonator gets rejected by the resonator, and therefore does not couple to the qubit. This is known as Purcell protection [Purcell46].

1.6 Multiple qubits in a resonator: the Tavis-Cummings model

In (1.26) we described the coupling between a single atom and a single mode of light using the Jaynes-Cummings model. For multiple atoms, there is another model named after its inventors Tavis and Cummings [Tavis68].

$$\hat{H}_{TC} = \hbar\omega_r\hat{a}^\dagger\hat{a} + \sum_j\left(\frac{\hbar\omega_j}{2}\hat{\sigma}_{z,j} + \hbar g_j(\hat{a}^\dagger\hat{\sigma}_j^- + \hat{\sigma}_j^+\hat{a})\right). \tag{1.27}$$

The only difference with (1.26) is that we sum over all j qubits positioned in the resonator. In 1.8b such a system is depicted schematically.

We have now described a single qubit in a resonator in equation (1.26) and multiple qubits in a resonator in equation (1.27), but there are still

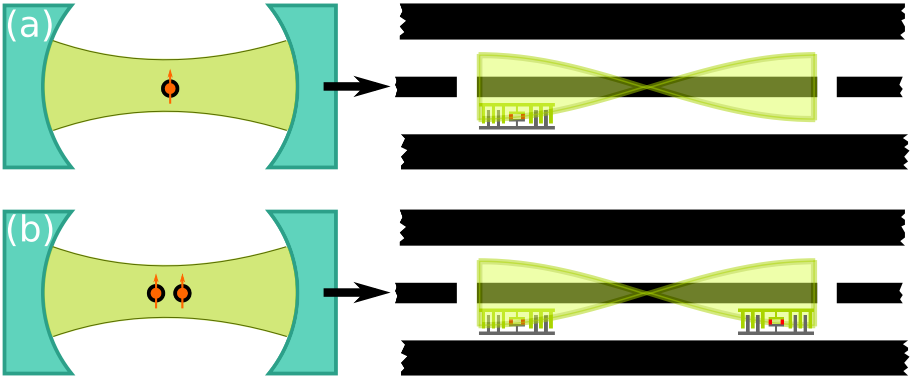

Figure 1.8: The coupling of two-level systems to a single mode of light has been studied in cavity QED using atoms and high-finesse optical cavities, and analogously in circuit QED using superconducing qubits and coplanar waveguide transmission line resonators. A system of one qubit coupled to one photonic mode (a) is described by the Jaynes-Cummings model. Having two or more qubits (b) is described by the Tavis-Cummings model.

more combinations of resonators and qubits, such as the Jaynes-Cummings-Hubbard model which describes many coupled cavities which each house one qubit. In state of the art circuit QED experiments, there is usually a mix of having multiple coupled resonators (not necessarily resonant), each of which can have more than one qubit. An example of such a sample is shown in 1.9.

1.7 The 3D cavity

Another environment to embed superconducting qubits in has recently received much attention: the so-called 3D cavity [Paik11]. These resonators consist of a block of metal with a cigar-shaped cavity machined out. Due to the much bigger mode volume in these cavities, the electric field density is much smaller, resulting in better coherence properties of the qubits through a decreased coupling of the field to two-level fluctuators. On the other hand, the size of the capacitor plates of the transmon qubit(s) needs

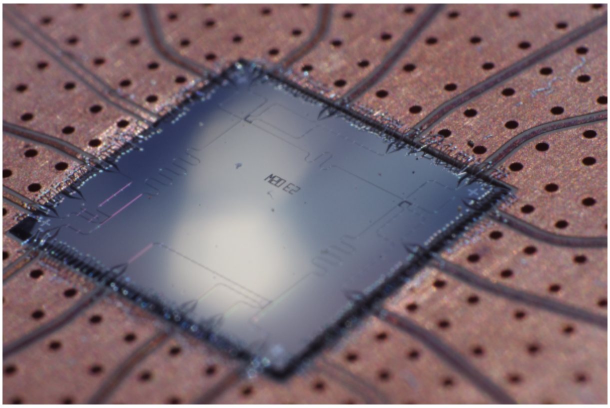

Figure 1.9: State-of-the art circuit QED experiments use multiple resonators and multiple qubits. This chip, used for teleporting the state of a qubit [Steffen13], features three resonators and four qubits, two of which are shared between two resonators.

to be increased to still achieve a strong coupling between the cavity mode and the qubit. Since there is usually no direct way to locally apply small fluxes to a squid loop, these qubits consist of a single junction between two large capacitor plates. While it is technologically harder to selectively address and read out qubits in such an architecture, the much higher coherence times ($T_1 \approx 100\ \mu$s [Rigetti12] instead of a few μs in traditional circuit QED experiments) have made sure that superconducting qubits in 3D cavities are being researched in labs around the world.

1.8 Qubits in an open transmission line

Another possibility is to place the qubit in an open transmission line. This was first suggested by Shen [Shen05b], and first experimentally implemented by Astafiev and coworkers [Astafiev10a], who used a flux qubit coupled to a transmission line by means of kinetic inductance. What makes this system so interesting for experimental investigation is that it is completely analogous to having a real atom in a one-dimensional space. However, using superconducting qubits and transmission lines makes it much easier to construct such a one-dimensional space, and to achieve a strong coupling between the photons propagating in the one-dimensional continuum and the artificial atom. After the initial experiments, which measured resonance fluorescence of a single artificial atom [Astafiev10a], the same group has measured time-resolved dynamics [Abdumalikov11] and electromagnetically induced transparency [Abdumalikov10] in the same system. Furthermore, the Per Delsing group used a single transmon in an open transmission line to measure the giant cross-kerr effect [Hoi13a], to measure the second order correlation functions [Hoi12], and to implement a single-photon router [Hoi11].

In this work we will concern ourselves with multiple qubits in a transmission line. Such a system is particularly well-suited for studying photon-mediated interactions between distant quantum systems in an open environment. Research on such systems was previously done in trapped ions [DeVoe96], but interaction effects were small. When atoms interact in a 3D space, the probability of a photon emitted by atom A to hit atom B is given by the solid angle formed by the scattering cross-section of atom B divided by 4π, the solid angle of the full spherical shell. If the two atoms are now placed in a one-dimensional space, the situation changes drastically. A photon emitted by qubit A can now either go left – away from atom B, or right – towards atom B. The probability for a photon emitted by A to hit B is therefore much higher in a one-dimensional space, and does not depend on distance. The interaction effects between atoms due to photon exchange are therefore greatly increased when reducing the dimensionality of the experimental system. Multiple artificial atoms which couple strongly to a shared transmission line thus form an experimental system extremely well suited for studying the interactions of atoms in an open space.

Investigating such a system also seems to be logical from a historical viewpoint, as schematically represented in Fig. 1.10. Interactions between a single photonic mode and an atom were thoroughly experimentally investigated in cavity QED, and later in its on-chip sibling circuit QED. Subsequently, the number of atoms was increased, and the interactions between atoms mediated by a single mode were investigated. Similarly, the number of atoms could be kept constant while increasing the number of modes coupling to the atom. The next logical step, indicated by the grey arrows in Fig. 1.10 is then to investigate the coupling of multiple atoms via multiple photonic modes.

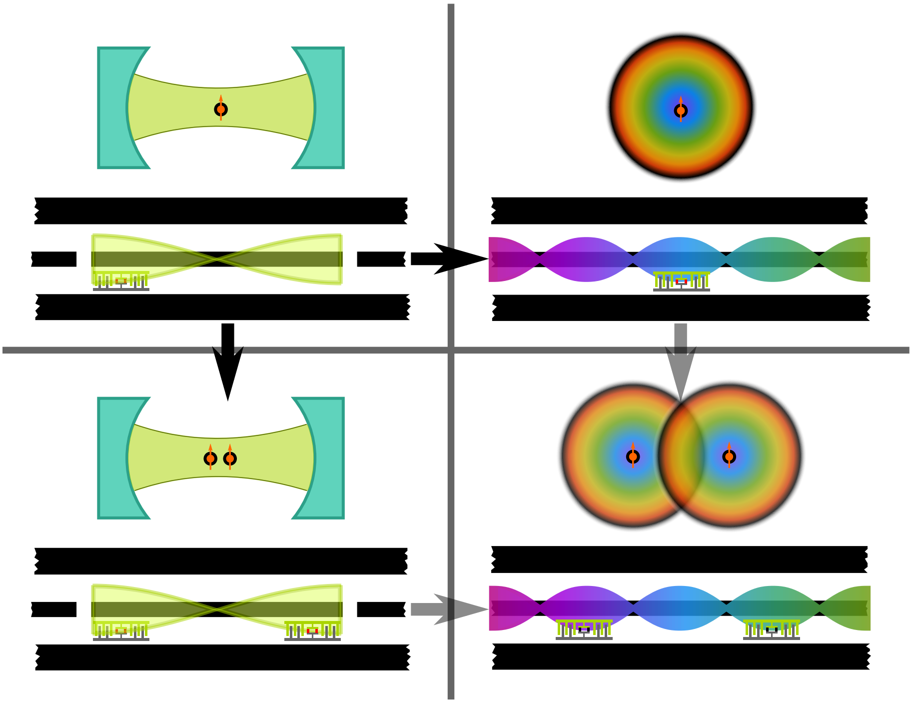

Figure 1.10: First the interactions between a single mode and a single atom were investigated (left upper panel). Experiments looking at interactions between a single mode and multiple atoms (left lower panel) and between a single atom and multiple modes (right upper panel) followed later. Now, we investigate the coupling of multiple atoms to multiple modes.

1.9 The structure of this thesis

This thesis is structured as follows. After the introduction, of which this is the last section, the experimental setup is explained in chapter 2, including several measurement methods used to obtain the experimental results presented later. In chapter 3, expressions are derived for the transmission and reflection coefficients of a single qubit in an open transmission line, and experiments are presented exhibiting the behaviour of a single quantum system coupling to a continuum of modes. In chapter 4, we will use the expressions for single qubits to construct a transfer-matrix-based theory to explain the elastic scattering properties of two qubits in a transmission line. In chapter 5, we will explain the full quantum mechanical theory of N qubits in a transmission line, followed by experimental results that confirm the predictions of this theory. In chapter 6, we allow ourselves to speculate about the future experiments and technologies building on this work.

2 Experimental setup and measurement techniques

Performing measurements on quantum systems always presents a challenge. Quantum phenomena are most apparent at small scales, and a quantum system is often easily perturbed by the thermal environment or by the act of measuring it. Much care must be taken to reduce noise as much as possible, and to improve the signal-to-noise ratio where possible. In our experimental setup, several precautions are taken to reduce unwanted interactions between the quantum system and the environment, which otherwise would result in a loss of information about our quantum system leaking out to the environment.

One way to reduce the coupling of the environment to the quantum system involves placing the qubits in a magnetic shield made out of a nickel-iron alloy with high magnetic permeability (see Fig. 2.1a). This reduces the coupling of stray magnetic fields (for example magnetic fields caused by magnets in other experiments) to the qubits. To reduce the coupling of external microwave radiation and thermal radiation to the sample, we embed it in a closely fitting copper box which we call sample box. The different parts of the sample box are shown in Fig. 2.1b,c. The printed circuit board (PCB) containing the sample (labeled with ‘4’ in 2.1) is fixed to the first part (‘1’ in 2.1), which also houses the coils used for applying magnetic fields to the qubits. The second part (part ‘2’ in Fig. 2.1) fits closely around the chip and the coplanar waveguides on the PCB to prevent the formation of whispering gallery modes. The third part (part ‘3’ in 2.1) affixes the total assembly to the cryostat and contains adaptors for connecting the sample to the microwave lines, which are used for manipulating and measuring the quantum system. The total assembly – the sample bonded onto the PCB, and the PCB mounted inside the sample box, is fixed inside a dilution cryostat which cools the chip down to temperatures between 40 to 90 mK, in order to make sure that the thermal energy of the immediate environment is much smaller than the qubits' transition energy ($k_B T \ll \hbar\omega_{ge}$).

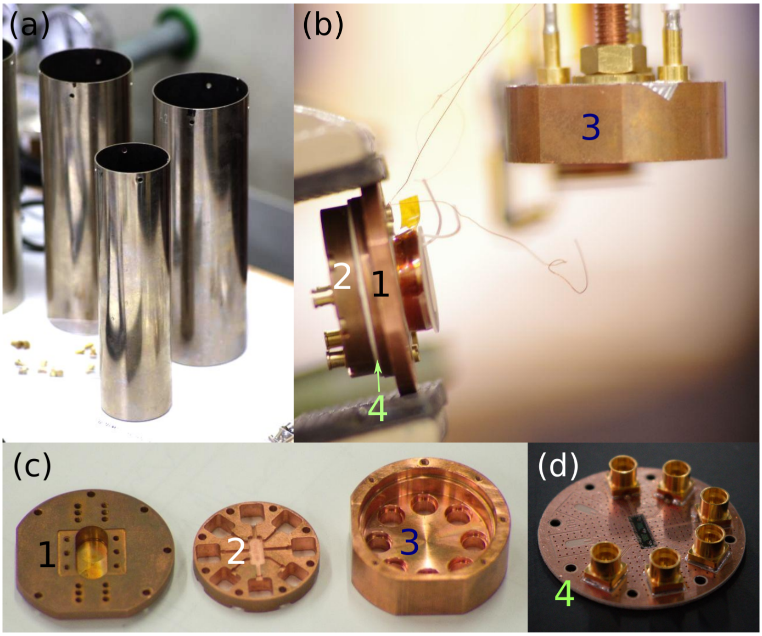

Figure 2.1: Protecting the sample: (a) the sample box is placed in a shield made out of a high magnetic permeability alloy. The sample, mounted on a printed circuit board (d) is put into a tightly fitting sample box (b,c). The sample box consists of three parts. The printed circuit board with sample and the coils for magnetic biasing are mounted on part one (d). Part two closely covers the sample and lines to avoid whispering gallery modes. Part three closes the assembly and allows for microwave cables to connect.

2.1 Magnetic biasing of the qubits

For most experiments, the qubits need to be tuned to specific frequencies. As discussed in section 1.4.2, the transmon eigenenergies depend on the flux through the squid loop. There are two different strategies in common use for applying flux to the qubit. The first strategy involves placing small superconducting coils close to the qubits, with a specific coil preferably coupling much stronger to one qubit than to the other qubits. The second strategy involves fabricating a local flux control line on the chip close to the squid loop. The current through a straight line causes a cylindrical magnetic field around it, changing the flux through nearby squid loops. This second strategy has two advantages: it generally allows for very fast flux pulses, tuning the qubit frequencies in nanoseconds, and moreover is usually more qubit-selective. A disadvantage is that applying a current through non-superconducting parts of the setup can heat up the sample, especially when such a current is applied continuously. When applied for very short times, one has to very carefully characterize the lines through which the currents are applied, lest the pulse shape at the qubit be different from the desired pulse shape.

For the experiments presented here we were interested in a static tuning of the qubit transition frequencies, and thus we used superconducting coils mounted below the chip. A voltage is applied at room temperature to a home-made voltage-to-current converter which also acts as a low-pass filter (see Fig. 2.2). The total resistance of the converter is designed to convert the range of the voltage source (-20 to 20 Volts) to a flux through the nearest qubit in the order of two flux quanta. The capacitor serves to route high-frequency noise to ground.

In practice, each qubit will be affected by the magnetic field due to any single coil. To still be able to tune the qubits separately, the coupling between each qubit and each coil must be known, such that cross-coupling effects can be compensated for. In order to do that, the mutual inductances between all coils and qubits need to be known. They are measured by by sweeping the voltages on each coil one by one and fitting the qubit curves, the fitting parameters being the mutual inductances between each qubit and coil (N*M inductances for N coils and M qubits) and the flux offsets from the environment (M offsets for M qubits). One such measurement with fit curves is shown in Fig. 2.3. For three qubits, we have the following relation between the voltages applied by the room-temperature voltage source and the fluxes seen by the qubit:

$$\begin{pmatrix}\phi_1\\ \phi_2\\ \phi_3\end{pmatrix} = \begin{pmatrix}M_{11} & M_{12} & M_{13}\\ M_{21} & M_{22} & M_{23}\\ M_{31} & M_{32} & M_{33}\end{pmatrix} \cdot \begin{pmatrix}V_1\\ V_2\\ V_3\end{pmatrix} + \begin{pmatrix}\Phi_1\\ \Phi_2\\ \Phi_3\end{pmatrix}, \tag{2.1}$$

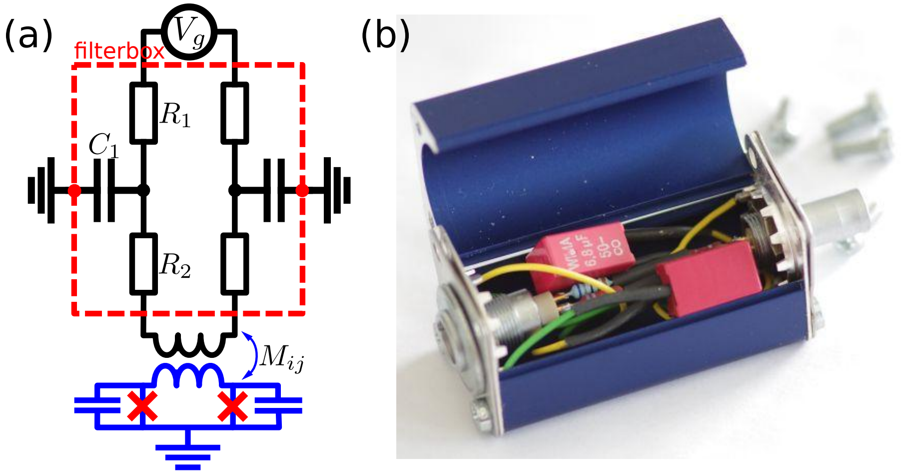

Figure 2.2: (a) The schematic of a voltage-to-current converter and filter, containing two resistors in series and a capacitor to ground for each of its two lines. Here we show only the inductance between coil i and qubit j, but each coil couples to each qubit. (b) When soldering such a filter, care must be taken not to have any contact between the two lines.

where M_{ij} denotes the mutual inductance between qubit i and coil j. Using the approximate identity for calculating the qubit transition frequencies (1.24), we have for qubit j

$$\omega_{eg,j} \approx \sqrt{8E_{C,j}E_{Jmax,j}\left|\cos\left(\frac{\pi}{\Phi_0}(\mathbf{M}\cdot\vec{V}+\vec{\Phi})_j\right)\right|} - E_{C,j}, \tag{2.2}$$

where $\mathbf{M}$ is the matrix of mutual inductances, $\vec{V}$ the vector of voltages on the coils, and $\vec{\Phi}$ the vector of flux offsets at the qubits. While (2.2) shows the approximate expression for finding the qubit frequencies from the fluxes for clarity, for the experiments presented later we used the Mathieu functions to calculate the exact qubit frequencies (up to the assumption that the junctions in the squid are equal).

Full control over the individual qubit fluxes is only possible if the number of coils used for biasing the qubits is at least equal to the number of qubits.

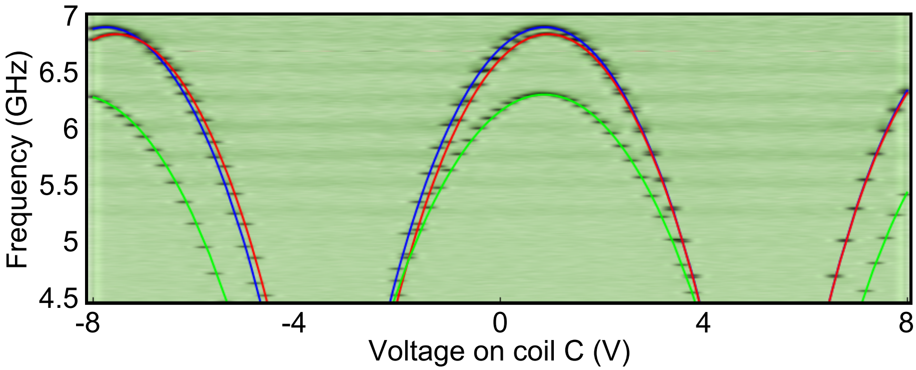

Figure 2.3: Spectroscopy for three qubits while sweeping the voltage over one coil. Color denotes the transmitted power through the system. The continuous lines are manual fits used to determine the mutual inductances between coils and qubits. Here, the voltage over the big coil was swept, which has a similar mutual inductance with each qubit.

Three different coil sizes where available for the experiments presented in this thesis. The so-called 'big coils' usually couple to all qubits with almost equal strength since the coil size is bigger than the chip size. There are also 'small coils', of which two can be placed in the cutout in the sample holder (see Fig. 2.4a), and which couple much more strongly to the qubits they are placed closest to due to their smaller size. Usually, one or two small coils are placed in the cutout on the sample box, after which a big coil is mounted on top. Finally, there are so-called 'tiny' coils available, of which three fit in the cutout in the sample holder. These, together with one big coil, can be used to individually tune up to four qubits.

The qubits regularly need to be tuned to specific frequencies for a specific experiment. Inverting (2.2), the qubits can simultaneously be tuned to arbitrary frequencies. An example of this control is given in Fig. 2.5 where we have used two qubits to draw $|\psi\rangle$ in frequency space. The precision of this procedure depends on the resolution of the voltage source and the shape of the mutual inductance matrix. In the presented experiments, the resolution of the voltage source resulted in a resolution of ~ 1 MHz in the

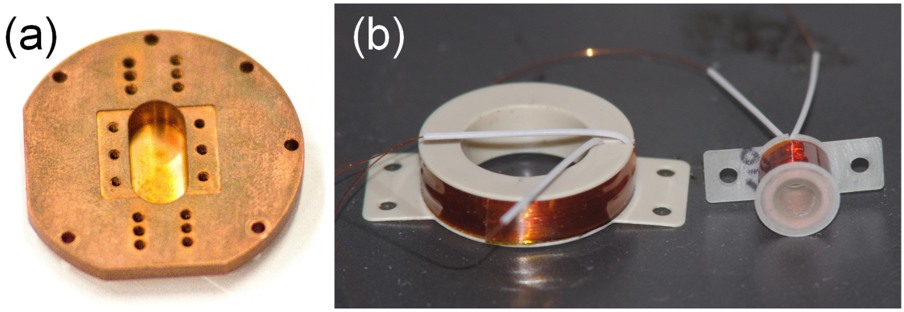

Figure 2.4: (a) There is a cutout in the bottom of the sample holder, which can hold either two 'small' or three 'tiny' coils. The big coil is then mounted on top. (b) A big and a small coil.

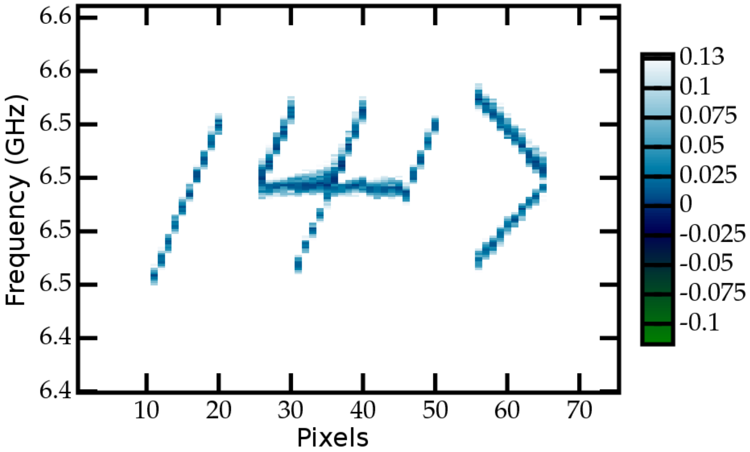

Figure 2.5: After finding the mutual inductances between coils and qubits and the flux offsets for each qubit, the qubits can be tuned to arbitrary frequencies. Here two qubits were used to write $|\psi\rangle$ in a spectroscopy plot. The color scale was tuned to increase the clarity of the picture. When the spectroscopy tone is not resonant with a qubit, the transmittance $|t|^2 \sim 1$.

frequency of the qubit coupled most strongly to this coil. When tuning multiple qubits, the uncertainty in the qubit frequencies due to limited voltage source precision is increased, as any qubit will be affected by the limited resolution in setting each coil. One way to improve the resolution is to use multiple voltage sources per coil, with the second source being connected to a filter box with a higher resistances, resulting in smaller currents at the coils. These first source would then be used for coarse-grained flux-tuning of the qubit, after which the second source would be used to fine-tune the qubit to the right frequency. A disadvantage of this method would be the increased noise resulting from using two voltage sources and two resistive filter boxes.

2.2 Microwave setup

The transition energy of the qubit is in the microwave regime. From an engineering point of view, having a system sensitive to RF frequencies is an advantage due to the availability of high-quality RF sources and components. However, a disadvantage is that such low frequencies necessitate cooling down the sample to millikelvin temperatures to ensure that $\hbar\omega \gg k_B T$. The microwave setup can be considered to consist of three parts: the first part contains lines and components between the microwave sources and the dilution refrigerator, the second part consists of the lines and components within the dilution refrigerator, and a third part connects output lines from the cryostat to a down-conversion setup and finally to an analog-to-digital converter and data-acquisition card.

2.2.1 Driving the qubits

For most experiments presented in this work, the qubits were driven via the transmission line. Due to the symmetric setup with circulators on either side of the sample (Fig. 2.8), both reflected and transmitted fields can be measured (Fig. 2.9). The generators are connected to the dilution refrigerator as in Fig. 2.6.

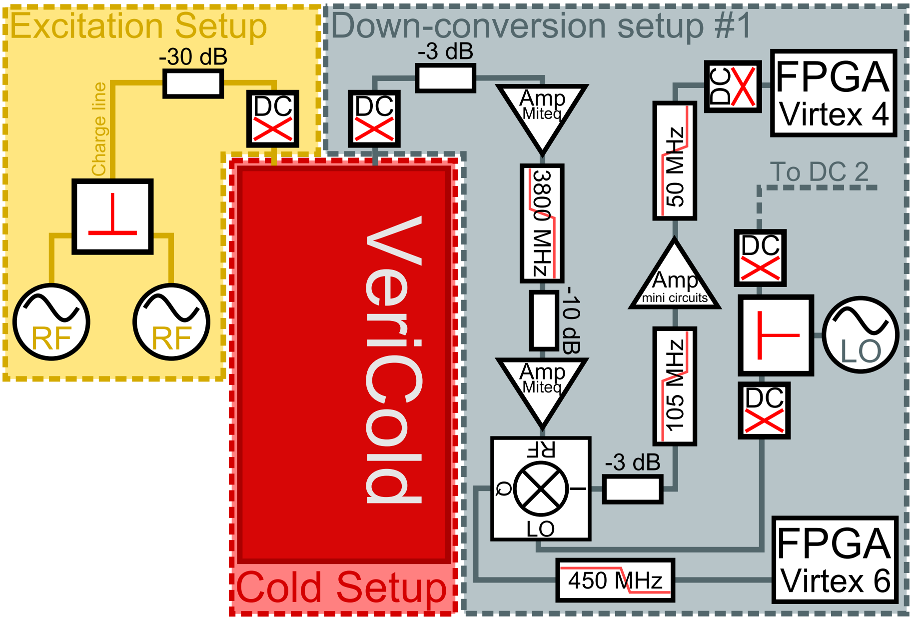

Figure 2.6: A schematic for the microwave setup used for driving and measuring the quantum system. Only one down-conversion board is shown. The second board is identical except that it has no connection to the Virtex-6 FPGA. The two different FPGA's were used for different measurements, for details see text.

2.2.2 Cold setup – reducing the Johnson-Nyquist noise

The superconducting circuits under investigation are cooled down to temperatures of 40 to 90 mK, reducing thermal noise due to the environment. However, the electronics used for controlling and measuring the quantum system cannot be cooled down to these temperatures. The room temperature control electronics exhibit room temperature noise characteristics, which would randomize the quantum system if placed in direct contact. To prevent that, we use high-amplitude signals at room temperature, such that the signal-to-noise ratio is high, and attenuate that signal at lower temperatures. Each time the signal is attenuated, so is the noise. But each attenuator also adds its own (50Ω-equivalent) noise at its own physical

Figure 2.7: To reduce noise, the incoming signal is passed through attenuators which are thermalized to local dilution cryostat temperature using copper connections. This is done at the 4K, 0.1K and base stage.

temperature (an attenuator can be described in the framework of quantum mechanics as follows: for an input signal $\hat{a}$ at the attenuator, the output signal is $\sqrt{A}\hat{a} + \sqrt{1-A}\hat{h}$, with $\hat{h}$ the annihilation operator for the noise added by the attenuator and A the attenuation factor). As can be seen in figure 2.8, we attenuate the signal with -20dB or a factor hundred in power at the 4 Kelvin stage, the 0.1 Kelvin stage, and at the baseplate, which was at temperatures between 40 mK and 90 mK during the presented experiments. The noise at the baseplate due to room temperature electronics is 10^{-6} times the room temperature noise plus 10^{-4} times the noise added by the first attenuator, which is equivalent to the noise caused by a 50 Ω resistor at 4K. The attenuators at lower temperatures still add 10^{-2} times the attenuator noise at 0.1K plus attenuator noise at the baseplate. How Johnson Nyquist noise affects the qubit is discussed later in section 3.1.3. A quantum mechanical explanation for Johnson-Nyquist noise (in the low temperature limit) was devised by Caldeira and Leggett [Caldeira83], and a concise introduction is given in [Devoret97].

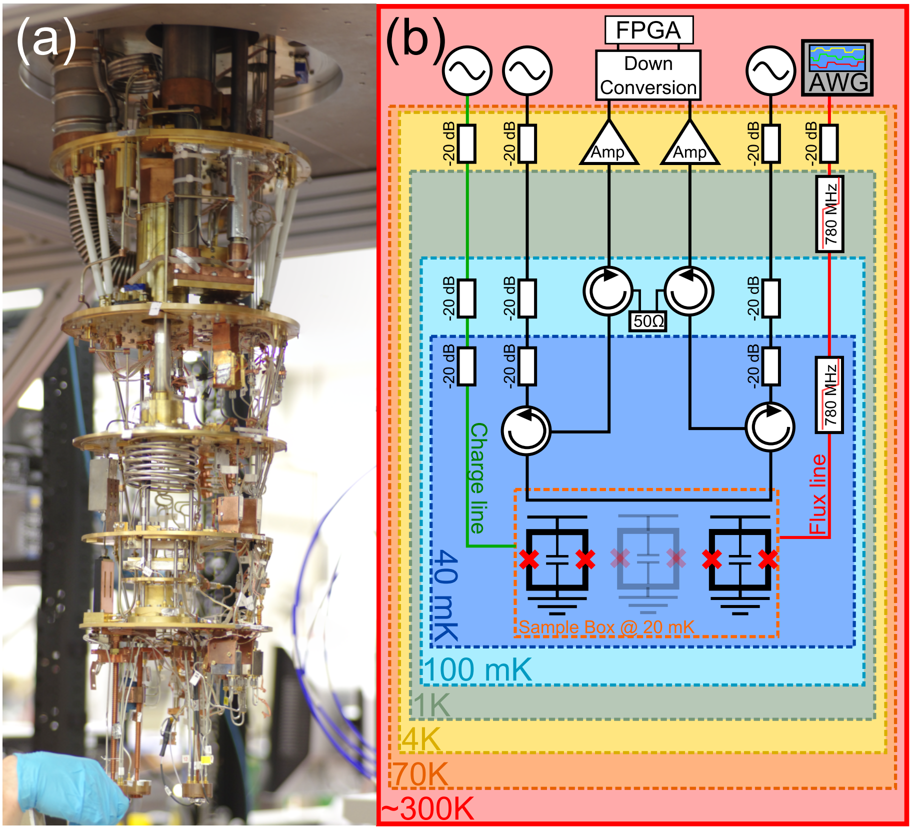

Figure 2.8: (a) The Vericold dilution refrigerator when the shields are taken off. (b) Schematic of the Vericold lines. Here only one charge and flux line are shown as all are identical.

2.2.3 Readout technology

Since research on qubits deals with single quantum systems emitting single photons, the measured signals are necessarily very small in amplitude. The signal-to-noise ratio is typically much smaller than one, and averaging is necessary to obtain a signal which can clearly be distinguished from the noise. However, even if we can average out noise that is fast compared to the measurement time, it still will not result in a usable signal unless the

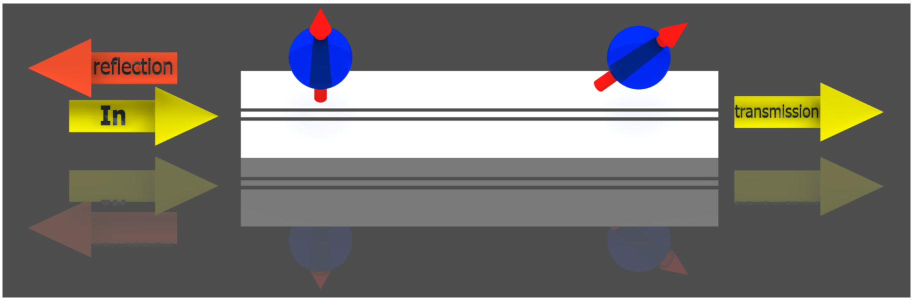

Figure 2.9: Radiation is applied from one side. Both reflection and transmission can be measured.

noise at lower frequencies is relatively small, including known low-frequency disturbances to the system such as temperature or flux drifts. In other words, the system needs to be stable during the entire time over which the measurements are repeated. Hence it is imperative to optimize the signal-to-noise ratio in order to decrease measurement time, and to increase the probability that a measurement can be done within the amount of time the system can be considered to be stable.
As can be seen in figure 2.8, signals coming from the sample are routed towards low-temperature high electron-mobility transistor (HEMT) amplifiers. After amplification, the signal enters the room-temperature down-conversion setup shown in 2.6 in order to perform heterodyne measurements, which are explained in section 2.4.

2.3 Amplification

Because typical signals in our experiments are small, they need to be amplified. It is important to realize what effect this has on the signal. For a signal $\hat{a}$ coming from the sample, an amplifier will magnify this signal by the amplifier gain G, but will also add noise. The commutation relation for the annihilation operator $\hat{a}$ is $[\hat{a}^\dagger, \hat{a}] = 1$. After the amplifier with gain G we have a signal described by signal operator $\hat{s}$. Because the commutator has to be equal to one, this signal operator is not simply given by $\sqrt{G}\hat{a}$. We have to add another term proportional to the creation operator $\hat{h}^\dagger$ of the added noise: $\hat{s}(t) = \sqrt{G}\hat{a}(t) + \sqrt{G-1}\hat{h}^\dagger(t)$ (Fig. 2.10). By adding this second term, with $\hat{h}^\dagger$ the fluctuation creation operator, the commutator $[\hat{s}^\dagger, \hat{s}]$ is still unity. We can now calculate the power of the noise due to the amplifier from its gain G by setting the signal to zero and calculating the power spectral density. We assume the noise to be thermal. It then follows that the autocorrelation function is $\langle \hat{s}^\dagger(t)\hat{s}(0)\rangle = (G-1)\langle \hat{h}(t)\hat{h}^\dagger(0)\rangle$. The thermal noise is approximately white, and contains no correlation between its values at different times. Therefore we have that $\left\langle \hat{h}(t)\hat{h}^\dagger(t)\right\rangle = \delta(t)(N+1)$, and the autocorrelation function of the signal is $\left\langle \hat{s}^\dagger(t)\hat{s}\right\rangle = (G-1)\delta(t)(N+1)$. The power spectral density of the noise, which is given by the Fourier transform of its autocorrelation function, is then $S(\omega) = (G-1)(N+1)$, with N the number of noise photons.

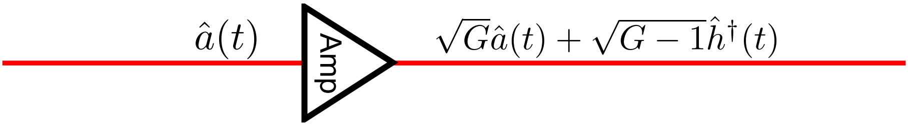

Figure 2.10: An amplifier provides gain, increasing the signal amplitude, but simultaneously adds noise.

2.4 Heterodyne measurements

The coherently scattered light is detected using a heterodyne measurement scheme. A circulator was placed on either side of the sample, so that radiation could be applied and measured from both sides of the chip. This way, both the reflected and transmitted fields could be measured. A simplified schematic of the heterodyne measurement setup is shown in figure 2.11. The full warm part of the measurement system is given in figure 2.6. The electric field at the output of the system is proportional to $\vec{E}(t) \propto \frac{1}{2}\left(\hat{a}(t) + \hat{a}^\dagger(t)\right)$. If we look at a mode of the field at frequency ω we can write the field in the Heisenberg picture as $(\hat{a}(t)e^{-i\omega t} + \hat{a}^\dagger(t)e^{i\omega t})/2$, with $\hat{a}(t)$ changing much slower with time than ω. Such a signal (not limited to a single mode) enters our down-conversion setup at position 1 in figure 2.11. We then perform analog down-conversion by using a mixer to modulate the input signal with an oscillating signal $\cos(\omega_{\mathrm{LO}}t)$, where LO is an acronym for local oscillator. The resulting signal is a multiplication of the two input signals at the mixer. At position 2 in 2.11 we therefore have $\frac{1}{2}(\hat{a}e^{-i(\omega-\omega_{\mathrm{LO}})t} + \hat{a}e^{-i(\omega+\omega_{\mathrm{LO}})t} + \hat{a}^{\dagger}e^{i(\omega-\omega_{\mathrm{LO}})t} + \hat{a}^{\dagger}e^{i(\omega+\omega_{\mathrm{LO}})t})$ (a quantum-mechanical description of a mixer can be obtained by considering it as an attenuator with a time-dependent attenuation factor). The low-pass filter removes the terms containing the sum frequencies, such that we have $\frac{1}{2}(\hat{a}e^{-i(\omega-\omega_{\mathrm{LO}})t}+\hat{a}^{\dagger}e^{i(\omega-\omega_{\mathrm{LO}})t})$ at position 3 in the figure. Finally, in the digital down-conversion (DDC), the signal is digitized, and two copies of the signal are processed in parallel. One copy is multiplied with a cosine function, and we call the result the I quadrature. The other copy is multiplied with a sine function, resulting in the Q quadrature. The signal then gets reconstructed from the quadratures as $I + iQ$. Since we have the identity $e^{i\omega t} \equiv \cos(\omega t) + i\sin(\omega t)$, it is clear that the combination of these operations is identical to multiplying the signal at position 3 in figure 2.11 with $e^{i\omega t}$. If we now choose the frequency of the digital down-conversion equal to $\omega - \omega_{\mathrm{LO}}$, this results in $\frac{1}{2}(\hat{a}+\hat{a}^{\dagger}e^{2i(\omega-\omega_{\mathrm{LO}})t})$. The last of these terms gets digitally filtered out, so that at the end of our measurement chain we have $I + iQ \propto \hat{a}$.

It should be stressed here that the field at the input of the analog-to-digital converter contains both electric and magnetic field contributions. The ADC only measures the real part of the electric fields only, which is akin to measuring a single quadrature of the field. However, as we record an oscillating field as a function of time, we are able to extract both quadratures of the field due to the time-correlations within the signal.

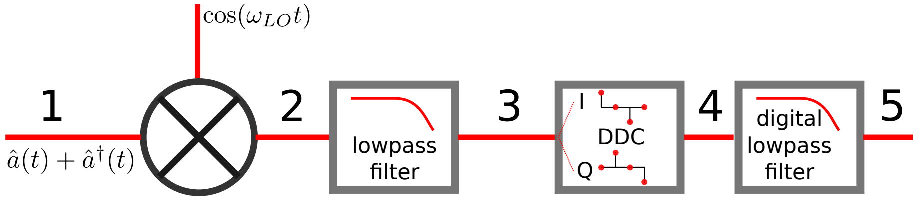

Figure 2.11: A schematic of a heterodyne detection scheme, as explained in section 2.4.

2.5 Coherently scattered radiation

Measurements of coherently scattered radiation were done using the Virtex-4 Field-Programmable Gate Array (FPGA) for data acquisition and processing. The data is digitized at a rate of 100 MHz, or one data point every 10 ns, for 1024 (or 2^{10}) consecutive points. A set of consecutively measured points will be referred to as a trace in the following. These measurements are repeated every 12.5μs. The digital down-conversion (DDC) is done by multiplying the signal with a four-point sine (0,1,0,-1) and cosine (1,0,-1,0) as shown schematically in figure 2.11. This way, only sign-flips and multiplications by 0 are needed, making the DDC computationally very efficient. To get a good signal-to-noise ratio, multiple traces are measured and averaged. The averaged trace gives us the expectation value $\langle \hat{a} \rangle$ as a function of time.
So far we have not discussed noise. We can take into account that any measured signal $\hat{s}$ contains noise by stating $\hat{s} = \hat{a} + \hat{h}^{\dagger}$, where $\hat{a}$ is the signal annihilation operator, and $\hat{h}^{\dagger}$ the noise creation operator. After averaging we then find $\langle \hat{s} \rangle = \langle \hat{a} \rangle + \langle \hat{h}^{\dagger} \rangle$, but since the noise fluctuates randomly around zero, we get that $\left\langle \hat{h}^{\dagger} \right\rangle = 0$, such that only the signal remains.
The act of averaging has a second effect. When the heterodyne detection scheme was explained in section 2.4, we only looked at a single mode of the field at a certain frequency. However, in reality there will be modes at any frequency at the input port of the mixer, some of which will be due to noise, and some of which will be due to the system under investigation. When measuring coherently scattered light, we choose the LO frequency and the frequency at which the DDC is done (also known as the IF or intermediate frequency) such that they add up to the frequency with which we drive the system. Besides coherently scattered radiation, the quantum system can scatter light incoherently. The random phase of such incoherently scattered radiation will cause it to average to zero when the measurement is done many times.
Averaging also affects the bandwidth of radiation that is detected. If a single trace is measured, the bandwidth of radiation that will be detected is set by the length of this trace T. Signals which are detuned from the $\nu_{\mathrm{LO}} + \nu_{\mathrm{IF}}$ by more than $1/T$ will average out, so the measurement bandwidth for this detection scheme is $\sim 1/T$. Increasing the number of averages by N has

the same effect as as increasing the length of the measurement to NT, and therefore reduces the bandwidth to $1/NT$.

2.5.1 Background subtraction

Not only the qubits exhibit frequency-dependent transmission and reflection coefficients. While the components used in our setup are ideally perfectly impedance-matched in their working bandwidth of 4 to 8 GHz, in reality there are always some imperfectly matched cables, and the components often have a frequency-dependant attenuation. To clearly see which signatures in a measurement are due to the qubits, and which are due to impedance mismatches, we subtract the spectrum of the components and lines from the signal. To measure the background spectrum, we tune the qubits out of the bandwidth of our setup, and measure how much of our input signal is transmitted and reflected by the components and lines as a function of frequency. These background transmission and reflection amplitudes can then be used to calculate the transmittance (normalized transmitted power) and reflectance (normalized reflected power) due to the qubits from the measured transmitted and reflected amplitude according to

$$|t|^2_{qubit} = \frac{|t|^2_{measured}}{|r|^2_{bg} + |t|^2_{bg}} \tag{2.3}$$

$$|r|^2_{qubit} = \frac{|r|^2_{measured}}{|r|^2_{bg} + |t|^2_{bg}}. \tag{2.4}$$

The suffix 'bg' denotes background measurements. Typical traces of the background spectra in reflection and transmission are shown in Fig. 2.12.

While we cannot be conclusive based just on the background reflection and transmission, the non-flat background indicates that the qubit might be subject to an electromagnetic environment which does not have the completely uniform density of states that is expected for an open one-dimensional environment. In section 3.1.2 we will come back to this point. It should also be pointed out that it matters which frequencies the qubits are tuned to during the background spectrum measurements. Usually, for measuring background traces, the qubits are tuned to frequencies below the bandwidth such that only one background trace is needed for any measured trace within the bandwidth. However, it makes a difference for the background if a qubit is tuned below or above the measured frequency. The

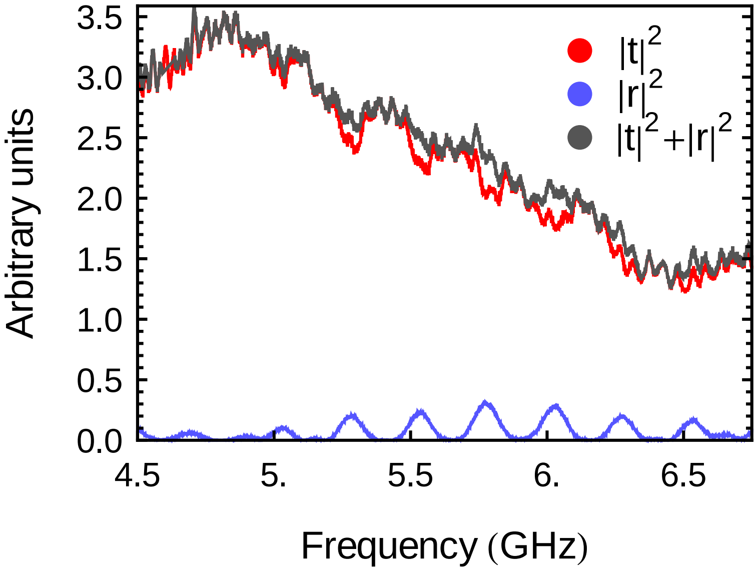

Figure 2.12: The power reflected and transmitted by the lines and components as a function of frequency. The transmitted and reflected powers are not normalized.

qubits can form weak standing modes with any impedance mismatches in the entire setup. Therefore, if the qubits are tuned to low frequencies during a background measurement, harmonics of weak standing modes at these lower frequencies will be included in the background measurement but not in the measurement with the qubit tuned to its frequency of interest. In such a case, part of the background that will be subtracted is not part of the actual background during the experiment. In Fig. 2.13 this is most clearly seen when looking at both sides of the line caused by the lowest-frequency qubit – the ripples in the background are more pronounced on the right side of this qubit than on the left side. The quality of background subtraction is therefore dependent on the specific measurement done. Fig. 2.13 shows a more affected background than is typically the case, usually the ripples in the background are less pronounced after background subtraction. These effects could be prevented by tuning the qubits to higher frequencies during background measurements. The qubits used in the presented experiments, however, did not have high enough maximum transition frequencies, so that we were not able to tune all qubits above the measurement range of interest.

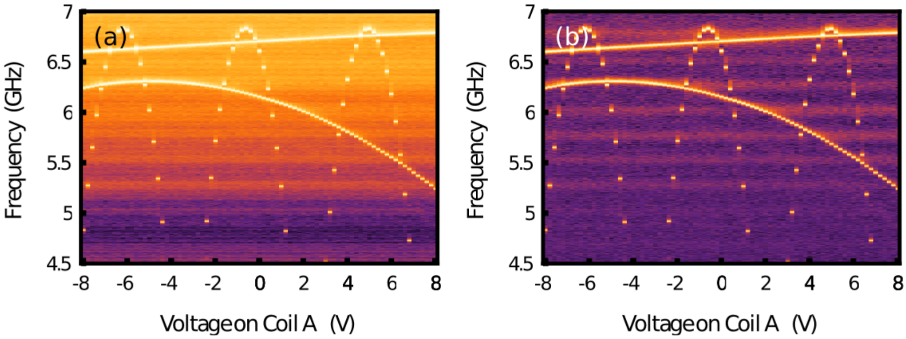

Figure 2.13: The frequencies of three qubits are shown as a function of the voltage applied to coil A before (a) and after (b) background subtraction. The non-uniform background in (b) shows that background subtraction was far from ideal in this case.

2.6 Power spectral density measurements and resonance fluorescence

As mentioned in section 2.5, averaging the measured voltages proportional to $\hat{s}$ causes incoherently scattered light to cancel. This necessarily includes all inelastically scattered light. Inelastically scattered light can however reveal interesting properties of the system under investigation, such as its power spectral density $S(\omega)$.

To understand how to measure power spectral densities, we start off with recalling that after the digital down-conversion but before averaging, we have that $(I + iQ)(t) \propto \hat{s}(t) = \hat{a}(t) + \hat{h}^{\dagger}$. Using the fast electronics of the Virtex-6 FPGA, we perform a fast Fourier transform (FFT) on the data (details are given in section 2.6.3), resulting in $\mathcal{FT}(\hat{s}(t)) = \hat{a}(\omega) + \hat{h}^{\dagger}(\omega)$. We multiply this result with a complex conjugated copy of itself to get $\mathcal{FT}(\hat{s}(t))\cdot$

$\mathcal{FT}(\hat{s}(t))^\dagger = \hat{s}(\omega)\hat{s}^\dagger(\omega) = |\hat{s}(\omega)|^2 = S_{\hat{s}\hat{s}^\dagger}[\omega]$. Using the convolution theorem we know that this is equal to the Fourier transform of the autocorrelation function, which is given by the convolution of a signal with itself: $R_{ss^\dagger}(\tau) = (\hat{s}(t) \star \hat{s}^\dagger(-t))(\tau) = \int_{-\infty}^{\infty} \hat{s}(t)\hat{s}^\dagger(t-\tau)$. Our system is assumed to be time-translation invariant, as we expect the system to reach a steady state well within the measurement time, such that $\langle \hat{s}(t)\hat{s}^\dagger(t-\tau)\rangle = \langle \hat{s}(\tau)\hat{s}^\dagger(0)\rangle$. We can write out the relation between the power spectral density function and the autocorrelation function as

$$S_{\hat{s}\hat{s}^\dagger}[\omega] = \mathcal{FT}\left[\left\langle \hat{s}\hat{s}^\dagger \right\rangle\right] = \mathcal{FT}\left[R_{ss^\dagger}(\tau)\right] \tag{2.5}$$

Writing the field operators in their signal and noise creation and annihilation operators, we have $R_{ss^\dagger}(\tau) = R_{aa^\dagger}(\tau) + R_{ah}(\tau) + R_{a^\dagger h^\dagger}(\tau) + R_{h^\dagger h}(\tau)$. The signal and noise are independent such that $\langle \hat{a}\hat{h}\rangle = \langle \hat{a}\rangle\langle \hat{h}\rangle$, and since $\langle h\rangle = 0$, only the autocorrelation terms for the signal and noise remain. The experiment is then repeated many times and averaged, after which we obtain the expected autocorrelation functions $\langle \hat{s}\hat{s}^\dagger\rangle = \langle \hat{a}\hat{a}^\dagger\rangle + \langle \hat{h}^\dagger\hat{h}\rangle$, or, using the linear nature of the Fourier transform, we obtain the power spectral densities $\langle S_{\hat{s}\hat{s}^\dagger}[\omega]\rangle = \langle S_{\hat{a}\hat{a}^\dagger}[\omega]\rangle + \langle S_{\hat{h}^\dagger\hat{h}}[\omega]\rangle$. For a more rigorous and complete account of how PSD measurements are performed in our experimental setup, we refer to [Lang11].

2.6.1 Diffmode measurements

In experiments where a quantum signal is amplified by a HEMT amplifier before it is measured, the noise is usually much bigger than the signal. This is due to the HEMT amplifier. We therefore expect the signal of interest $R_{\hat{a}\hat{a}^\dagger}$ to be drowned in the autocorrelation of the noise $R_{\hat{h}^\dagger\hat{h}}$. To counteract this, we use a measurement mode known as 'diffmode'. In diffmode, for each set of parameters, we first measure the autocorrelation function of the system with the drive switched on, yielding $\langle \hat{a}\hat{a}^\dagger\rangle + \langle \hat{h}^\dagger\hat{h}\rangle$, and then repeat the measurement with the drive tone off, yielding $\langle \hat{h}^\dagger\hat{h}\rangle$. Where diffmode differs from usual measurements is that when adding the Power spectral densities in order to obtain a result proportional to the average, each trace is multiplied by a factor -1^n, with n the trace number, where we start counting at 0. In other words, each background trace gets subtracted from the preceding signal trace to give $\langle \hat{a}\hat{a}^\dagger\rangle$.

The practical implementation of diffmode is as follows. The timing and

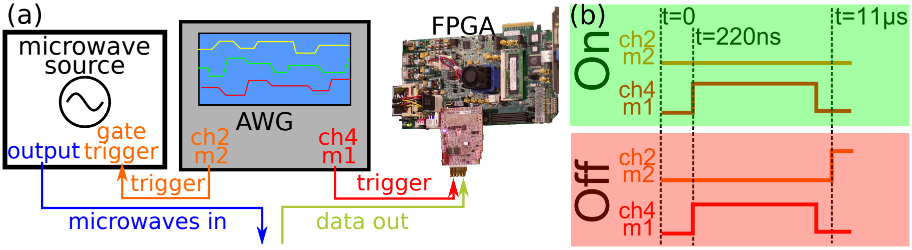

Figure 2.14: (a) An AWG, a microwave source and an FPGA are used to perform diffmode measurements. (b) Pulse schematic for diffmode measurements.

triggering is done by a pattern which is loaded onto an arbitrary waveform generator (AWG). The triggers, generated at the ’marker’ channels of the AWG, are connected to the microwave source and the FPGA (Fig. 2.14). The trigger input on the microwave source is set to ‘inverted’, such that a low level on the marker results in the microwave source being switched on, and vice versa. Typical rise times of the output signal of the microwave generator are less than 100 ns, and the times it takes for it to react to a trigger can be as long as 200 ns. The diffmode trigger sequence consists of two patterns. The first pattern starts with the microwave source already on. After 220 ns, the FPGA is triggered to start its measurement, for which any trigger length longer than 8 ns can be used. The Virtex-6 FPGA measures for 8192 ns. The measurement stops, and the source stays on until the end of the pattern. The second pattern starts 12.5 μs after the start of the first pattern. It switches the microwave source off at the start of the pattern (at $t = 0$), and the FPGA is triggered to measure at $t = 220$ ns. 8192 ns later, the FPGA stops measuring. At $t = 11\mu$s, the microwave generator is switched back on, which is $\approx 1.7\mu$s before the next measurement, such that the rise time of the microwave source is not seen in the next measurement.

We have now shown how we measure $\langle S(\omega)\rangle = \left\langle \mathcal{FT}\left[\left\langle \hat{a}(\tau)\hat{a}^\dagger(0)\right\rangle\right]\right\rangle$, but it is not yet clear what measuring a power spectral density reveals about the dynamics of the artificial atoms. In order to investigate that, we need to look at the derivation of resonance fluorescence, which is lengthy but widely available in the literature. For the full derivation we refer to standard quantum optics textbooks [Scully97, Loudon00, Yamamoto99]. Here we limit ourselves to a summarized recipe for deriving resonance fluorescence, mostly in order to emphasize the conditions that have to be met by our system for the derivation to be valid - i.e. to make sure the measured result is equal to resonance fluorescence.

To calculate resonance fluorescence, one starts with the optical Bloch equations (see also section 3.1.4), which are solved for an atom initially in the ground state. The quantum regression theorem is used to get the two-time correlation functions for the atomic operators, where it is assumed that the system under investigation has evolved to a steady state. This sets the condition that the system should be measured after the drive has been on for a time much longer than any timescale involved in the dynamics of our system. Deriving the quantum regression theorem for finding the time-dependence of two-time averages $\langle \hat{Q}_i(t)\hat{Q}_k(t')\rangle$ (with $\hat{Q}_i$ any operator) only requires that $\langle \hat{h}_i(t)\hat{Q}_k(t')\rangle = 0$, with $\hat{h}$ the fluctuation operator (see [Yamamoto99], section 7.4). This condition is met for noise with very short correlation times, which for our system was already assumed earlier in this chapter. Thus, all conditions necessary for resonance fluorescence to be equal to the power spectral density of our system are met.

2.6.2 Background subtraction for power spectral density measurements

While using the diffmode measurement method results in measuring the power spectral density of the signal only, excluding noise, the data is still deformed by an effective filter imposed on the signal by the various frequency-dependent attenuation and gain factors due to all microwave components between sample and FPGA. We will call this the 'background filter'. To counteract for that, we measure the spectrum of the background filter separately and divide it out. The background filter can be measured by switching off diffmode, switching off the drive tone, but leaving the LO tone on in order to make sure that the background filter is measured around the right frequency. We are thus measuring the noise as deformed by this filter function. The effect of the filter is divided out by simply dividing a measured power spectral density by the power spectral density of the background filter. An example of a typical filter function is shown in figure 2.15.

To summarize the two procedures used to separate our signal from the noise: diffmode subtracts the power spectral density of the noise from each measurement. Another separate measurement is done without a signal to measure the frequency-dependent gain of the setup. The result of the diff-mode measurement is divided by this second measurement.

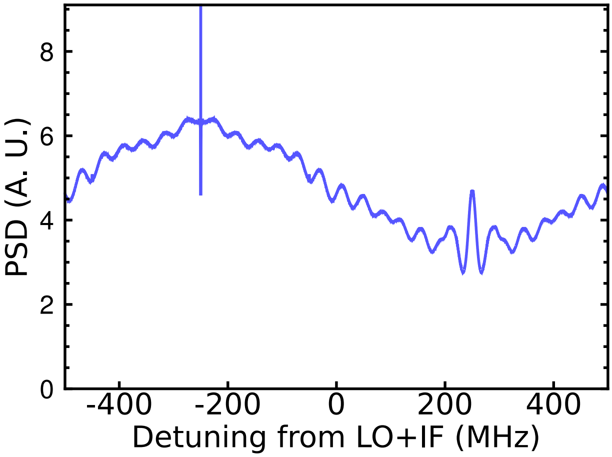

Figure 2.15: The signal from the sample goes through an effective filter due to the frequency-dependant attenuation of the microwave components between the sample and the ADC, and is modified by the analog and digital down-conversion. The spectrum of a typical 'background filter' is plotted. The LO frequency was set to 4.75 GHz.

2.6.3 Dividing and conquering the Fourier transform

To perform the Fourier Transform, we used the line connecting the sample to the Virtex-6 FPGA in figure 2.6. This line is connected to an analog-to-digital converter with a 1 GHz sampling rate. One time-trace, measured with the Virtex-6, is 8192 or 2^{13} ns long. The Virtex-6 itself has a clock speed of 125 MHz, and therefore cannot process the incoming data stream directly. Instead, the data is split into eight parallel channels of 125 MHz bandwidth which are Fourier transformed separately and recombined using the Cooley-Tukey algorithm. This algorithm - based on a recursive divide-and-conquer technique - is usually attributed to Cooley and Tukey

[Cooley65], but an equivalent algorithm was already invented by Gauss in (presumably) 1805 for interpolating movement of celestial bodies, even before Fourier published his groundbreaking work on harmonic analysis. Gauss however did not publish these results during his lifetime, they were instead published in his collected works after he passed away [Gauss66].
How such an algorithm works is not hard to see. We will show it below for unraveling the Fourier transform in two strands. To unravel into eight strands, simply apply the same procedure twice more on all resulting strands. To apply a full Fourier Transform, keep unraveling until arriving at size-two discrete Fourier Transforms.
The unraveling of the Fourier Transform is much like opening a zipper: we split the DFT into a part with even and a part with odd indices

$$\begin{aligned}\tilde{X}_k &= \sum_{n=0}^{N-1} x_n e^{-i\frac{2\pi}{N}nk} \\ &= \sum_{m=0}^{N/2-1} x_{2m} e^{-i\frac{2\pi}{N}(2m)k} + \sum_{m=0}^{N/2-1} x_{2m+1} e^{-i\frac{2\pi}{N}(2m+1)k}.\end{aligned} \tag{2.6}$$

In the last term, the '+1' in the exponent can be factored out to give

$$\tilde{X}_k = \sum_{n=0}^{N/2-1} x_{2m} e^{-i\frac{2\pi}{N/2}mk} + e^{-i\frac{2\pi}{N}k} \sum_{n=0}^{N/2-1} x_{2m+1} e^{-i\frac{2\pi}{N/2}mk} = \tilde{E}_k + e^{-i\frac{2\pi}{N}k}\tilde{O}_k, \tag{2.7}$$

where $\tilde{E}_k$ denotes the Fourier transform on the even components of $\vec{x}$ and $\tilde{O}_k$ is the transformation applied on the odd components. The number of components in $\tilde{X}_k$ is now however only $N/2$. To get all N components, we use that the DFT is periodic in N: $\tilde{X}_{k+N} = \tilde{X}_k$ [Oppenheim97]. That this property holds can be seen immediately from the definition in (2.6): adding N to any index k is equivalent to multiplying the expression by $e^{-\frac{2\pi i}{N}N} = 1$. Similarly, when the DFT goes from index $k = 0, \cdots, N/2 - 1$, the periodicity of the DFT imposes that $\tilde{X}_{k+N/2} = \tilde{X}_k$. The phase factor in front of the odd components in (2.7), for components $N/2 - 1 < k < N$ changes to $e^{-\frac{2\pi i}{N}(k+N/2)} = e^{-\frac{2\pi i}{N}k} \cdot e^{i\pi} = -e^{-\frac{2\pi i}{N}k}$. Therefore, for $k \geq N/2$, the result of the Fourier transform is the same as in (2.7), except for a minus sign in front of the odd part

$$\tilde{X}_k = \begin{cases} \tilde{E}_k + e^{-\frac{2\pi i}{N}k}\tilde{O}_k & k < N/2 \\ \tilde{E}_k - e^{-\frac{2\pi i}{N}k}\tilde{O}_{k-N/2} & k \geq N/2 \end{cases} . \tag{2.8}$$

Thus, due to the periodicity of the DFT, after splitting the data into two strands, only half of the number of components needs to be calculated. Moreover, this splitting up can be applied recursively. This way of calculating a DFT is therefore more efficient than simply performing a DFT on the entire data.

The algorithm used by the FPGA running Xilinx's implementations of FFT is a so-called radix-2 butterfly streaming FFT [Xilinx11]. Here streaming denotes that the FFT results are generated while the time-domain data is coming in. The 'radix-2 butterfly' denotes the most simple variant of a Cooley-Tukey algorithm: butterfly denotes recursively going down until arriving at two-point DFTs, 'radix 2' denotes unzipping the data in two equal even/odd strands at each recursion. For more details on how the Virtex-6 FPGA is programmed to enable for high-bandwidth Power Spectral Density measurements, see [Salathé11].

2.7 A note on using charge lines in waveguide QED

The results presented in this thesis were obtained on a sample that did not contain charge lines (local control lines used to apply high-frequency electric fields to individually manipulate qubits). While charge lines have been implemented in a later sample (shown in Fig. 2.16), that particular sample did not produce interesting results. It did however clarify that much care must be taken when designing a sample containing qubits in an open transmission line with charge lines. When charge lines are used in circuit QED, the resonator rejects off-resonant tones, and therefore the charge line only couples to the qubit it is directly connected to without coupling strongly to other qubits. However, in an open transmission line, there is no such rejection, and therefore the charge line couples relatively strongly to all qubits. There seems to be no obvious way to prevent this, but a second charge line could be used to apply radiation which could destructively interfere with the radiation from the first charge line leaking into the transmission line via a qubit. Tuning the phase and amplitude of the second charge line, it should be possible to completely cancel the radiation coupled into the transmission line by the first charge line. We propose to fabricate extra charge lines that couple directly to the open transmission line, with the express purpose of cancelling microwave radiation leaking into the transmission line via a charge-line-driven qubit.

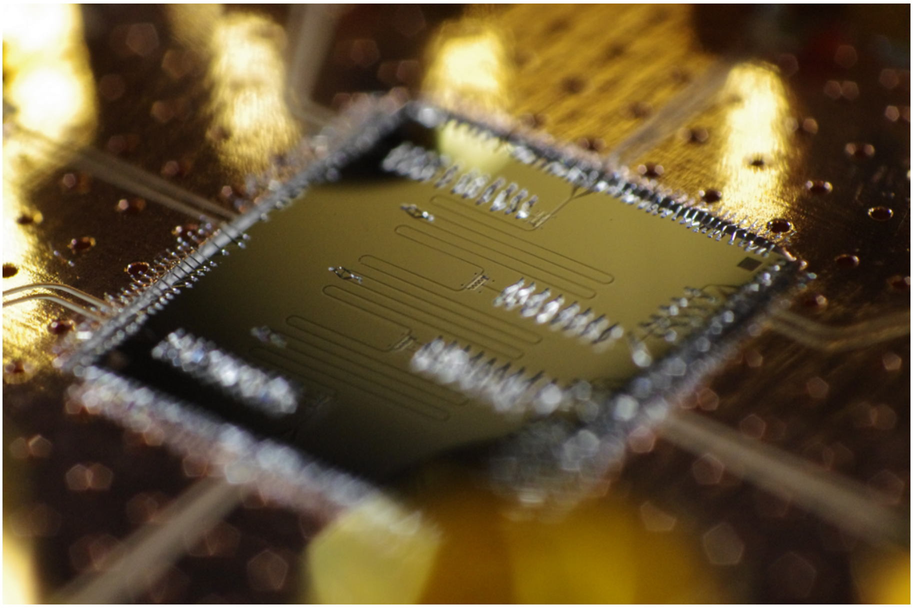

Figure 2.16: A waveguide QED sample with charge lines. Wire bonds were used to equalize the potential at the ground planes on opposite sides of charge lines and the open transmission line.

3 A single qubit in a transmission line

In this chapter, we first present the theory for a single qubit in a transmission line, after which we show the experimental results, and how they compare to theory.

3.1 Theory of a single qubit in a transmission line

In this section, we derive the reflection and transmission coefficient of a Transmon qubit in a transmission line. We will start by considering the circuit for a transmission line and see how the telegraph equations are affected by introducing the qubit as a dipole. We solve the 1D wave equation for the total voltage; the sum of the driving voltage and the voltage due to the dipole rotating in the AC field. To find the magnitude of this 'scattering' voltage, we find a relation between the noise-induced relaxation and the atomic dipole moment. Then we find the expectation value of the atomic lowering operator, which we achieve by finding the steady state solution of the optical Bloch equations for our system. Combining these results, we get an expression for the reflection coefficient of a qubit in a line. The result turns out to be the same as for a flux qubit [Astafiev10a] in a transmission line, even though the details in the derivation are not identical. We have followed the reasoning by Astafiev in this chapter to arrive at an expression for the single-qubit reflection coefficient. Another way to arrive at the same results is shown in [Peropadre13].

3.1.1 The 1D wave equation for a qubit in a transmission line

A coplanar waveguide transmission line can be modeled by a lumped element circuit as shown in figure 3.1. A lossless transmission line is governed

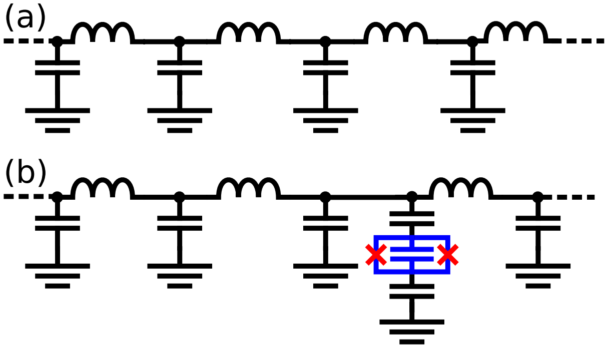

Figure 3.1: (a) Lumped-element circuit equivalent of a transmission line. (b) Schematic of a transmission line with a transmon qubit (blue) embedded in it. The red crosses are the Josephson Junctions.

by the telegraph equations [Pozar93]:

$$\begin{aligned}\partial_x V &= -l\partial_t I \\ \partial_x I &= -c\partial_t V.\end{aligned} \tag{3.1}$$

Here l and c are the inductance and capacitance of the line per unit length, and ∂_x and ∂_t denote the partial derivatives with respect to x and t. We introduce a superconducting transmon qubit into the transmission line as a dipole with dipole moment ϕ by modifying the telegraph equations to read:

$$\begin{aligned}\partial_x V &= -l\partial_t I + \phi\delta(x) \\ \partial_x I &= -c\partial_t V - \partial_t\phi\delta(x),\end{aligned} \tag{3.2}$$

where ϕ is the dipole moment of our qubit, and $\delta(x)$ is the Kronecker delta function. Taking the partial derivative with respect to x of the first of these, a partial derivative to t of the second of these and recombining, we get the one-dimensional wave equation for our system:

$$\partial_{xx}V - \frac{1}{v^2}\partial_{tt}V = l\partial_{tt}\phi\delta(x), \tag{3.3}$$

where v is the speed of light in the transmission line, given by $v = 1/\sqrt{lc}$, and we have a linear dispersion relation $k = \omega/v$

3.1.2 An atomic dipole in a rotating field

When driving the system with a coherent tone at a single frequency ω, the voltage in the transmission line as a function of time and space is given by

$$V_{\text{in}} = V_0 e^{i(kx-\omega t)}. \tag{3.4}$$

The qubit or dipole, which we place at $x=0$, thus is subjected to a rotating voltage. It will rotate with this input field and in doing so create its own field with magnitude V_{sc} which propagates symmetrically in both directions such that the total voltage is

$$V = V_0 e^{i(kx-\omega t)} + V_{\text{sc}} e^{i(k|x|-\omega t)}. \tag{3.5}$$

Due to the absolute value of x in the rightmost part of this equation, the voltage created by the dipole interferes differently with the input field in the direction of transmission and reflection. It is destructive or constructive for transmission depending on the sign of V_{sc}, which we will find to be negative. In the reflection direction we get a field of the shape $V = e^{-i\omega t}(V_0 e^{ikx} + V_{\text{sc}} e^{-ikx})$, which, when $V_0 \sim V_{\text{sc}}$, is a sinusoidal function in space that rotates in time (Fig. 3.2). After this signal passes through a circulator the input field and scattered field are separated and the reflected field looks like $V_r = V_{\text{sc}} e^{-ikx}$. How complete the destructive interference in transmission is, and how big the reflected signal compared to the input signal, depends then on the magnitude of V_{sc}. To find V_{sc}, we first substitute (3.5) into the one-dimensional wave equation (3.3):

$$\partial_{xx} V - \frac{1}{v^2}\partial_{tt} V = \delta(x) V_{\text{sc}} ik e^{i(k|x|-\omega t)}. \tag{3.6}$$

The atomic dipole, which rotates with the field, can be written as

$$\langle \phi(t) \rangle = \phi_{\text{tr}} \langle \hat{\sigma}_- \rangle e^{-i\omega t}, \tag{3.7}$$

where $\hat{\sigma}^-$ is the atomic lowering operator $|g\rangle\langle e|$, and ϕ_{tr} is the waveguide-QED equivalent of the coupling strength of the qubit to the line

$$\hbar \phi_{\text{tr}} = 2\beta e |\langle i|\hat{n}|k\rangle|, \tag{3.8}$$

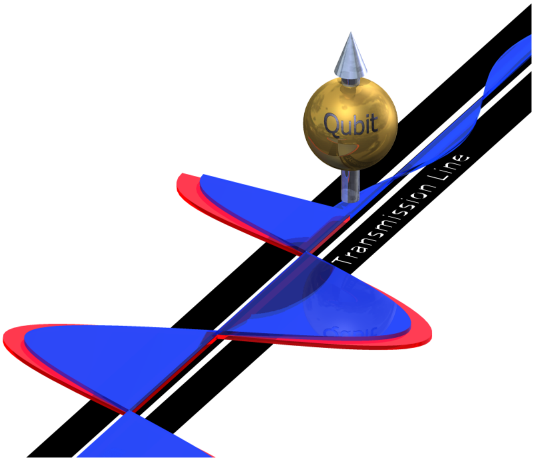

Figure 3.2: The qubit can be seen as a rotating dipole in the applied drive field. Its own field interferes destructively in the onwards (transmission) direction.

with $|\langle i|\hat{n}|k\rangle|$ the transition matrix element coupling state k to state i. When considering transitions between the ground and excited state, this can be written out as

$$\hbar\phi_{\text{tr}} \approx 2^{3/2}\beta e \left(\frac{E_J}{8E_C}\right)^{1/4}, \tag{3.9}$$

with all the variables as in chapter 1. For those familiar with the lingo of circuit QED, (3.9) can be seen to match g/V_{rms} with g as in [Koch07]. Equation (3.7) can be substituted into the right part of equation (3.3) and compared to the result in (3.6) to give

$$ikV_{\text{sc}} = -\omega^2 l\phi_{\text{tr}} \langle\hat{\sigma}_-\rangle\,. \tag{3.10}$$

3.1.3 Relaxation due to Johnson-Nyquist noise

The quantity of light that can be scattered by the artificial atom is intuitively expected to be limited by the relaxation rate – once the atom has absorbed a photon, it will have to emit the photon before it can absorb and emit another. In this system, the main noise is expected to be the Johnson-Nyquist noise due to the transmission line and microwave components, as the qubit is expected to couple much stronger to the transmission line than to noise sources elsewhere.

$$S_{\mathrm{V}}(\omega, T) = 2\hbar\omega \mathrm{Re}[Z] \coth\left(\frac{\hbar\omega}{2k_B T}\right), \tag{3.11}$$

where S_{V} is the spectral density of the voltage noise, ω the frequency under consideration (for relaxation we need only consider noise resonant to the qubit), $Z = \sqrt{l/c}$ the impedance of the transmission line, T the temperature of the noise source and k_B the Boltzmann constant. Even when taking care to thermalize the microwave lines to minimize this noise, the noise temperature of the transmission line will always be higher than the physical temperature of the system, because each attenuation that reduces of noise at a higher temperature adds noise at the temperature of that attenuator (this is discussed in more detail in section 2.2.2). The noise couples to the quantum system :

$$H_{\mathrm{noise}} = \phi_{\mathrm{tr}} V_{\mathrm{noise}} \hat{\sigma}_x. \tag{3.12}$$

The relaxation rate of the qubit can then be obtained using Fermi's golden rule [Sakurai10]:

$$\Gamma_1 = \frac{2\pi}{\hbar} |\langle f|H_{\mathrm{noise}}|i\rangle|^2 \rho_f, \tag{3.13}$$

with i the initial and f the final state, and ρ_f the density of final states. We take the excited state as the initial state, the groundstate as the final state, and go into the rotating frame at the qubit frequency such that the expression simplifies to $\Gamma_1 = \frac{\pi}{\hbar}\phi_{\mathrm{tr}}^2 V_{\mathrm{noise}}^2 \rho_f$. The density of final states is given by $\rho_f = 1/(\hbar d\omega)$, and the definition for the noise spectral density is $\frac{S_{\mathrm{V}}}{2\pi} d\omega = \langle V_{\mathrm{noise}}^2 \rangle$, such that $\Gamma_1 = \frac{\phi_{tr}^2}{2\hbar^2} S_{\mathrm{V}}$. Substituting S_{V} given by expression 3.11, we get

$$\Gamma_1 = \frac{\hbar\phi_{\mathrm{tr}}^2 \omega \mathrm{Re}[Z]}{\hbar^2} \coth\left(\frac{\hbar\omega}{2k_B T}\right). \tag{3.14}$$

We are in the quantum regime where $\hbar\omega \gg k_B T$. If this condition is not met, thermal energy populates the system. We then have that that

$$\Gamma_1 = \frac{\hbar\phi_{\mathrm{tr}}^2 \omega \mathrm{Re}[Z]}{\hbar^2}. \tag{3.15}$$

Substituting this expression into equation (3.10) results in a formula for the scattered voltage in terms of the relaxation rate of the qubit:

$$V_{\mathrm{sc}}(x,t) = i\frac{\hbar\Gamma_1}{\phi_{\mathrm{tr}}}\left\langle\hat{\sigma}_-\right\rangle e^{i(k|x|-\omega t)}. \tag{3.16}$$

3.1.4 Optical Bloch equations

The next step is to find the expectation value of the atomic lowering operator: $\langle\hat{\sigma}^-\rangle = \mathrm{Tr}[\rho\hat{\sigma}^-] = \rho_{21}$. In order to find this expectation value, we will solve the optical Bloch equations under the assumption that our system is in a steady state. We start by writing down the Hamiltonian of a two-level system in a frame rotating with the frequency of a drive tone:

$$\hat{H} = -\frac{\hbar}{2}(\delta\omega\hat{\sigma}_z + \Omega\hat{\sigma}_x), \tag{3.17}$$

where $\hat{\sigma}_x$ and $\hat{\sigma}_z$ are the Pauli matrices, $\delta\omega$ is the detuning between the Larmor frequency of the qubit and the drive frequency, and Ω the drive strength, which is connected to the input voltage through $\hbar\Omega = \phi_{\mathrm{tr}}V_0$. In the presence of losses, the dynamics of the system are captured by a master equation in Lindbladian form:

$$\frac{d\hat{\rho}}{dt} = -\frac{i}{\hbar}[\hat{H},\hat{\rho}] + \mathcal{L}[\hat{\rho}], \tag{3.18}$$

with $\mathcal{L}$ being the Lindblad superoperator, governing the losses. Both relaxation and pure dephasing are expected to play a role in our system. The Lindblad superoperator acting on the density operator $\hat{\rho}$ can then be written out to read:

$$\mathcal{L}[\hat{\rho}] = \frac{\Gamma_1}{2}(2\hat{\sigma}_-\hat{\rho}\hat{\sigma}_+ - \hat{\rho}\hat{\sigma}_+\hat{\sigma}_- - \hat{\sigma}_+\hat{\sigma}_-\hat{\rho}) + \frac{\gamma_\varphi}{2}(\hat{\sigma}_z\hat{\rho}\hat{\sigma}_z - \hat{\rho}), \tag{3.19}$$

where $\hat{\sigma}_- = |e\rangle\langle g|$ is the lowering operator, and $\hat{\sigma}_+ = \hat{\sigma}^{-\dagger}$ the climbing operator. The last term denotes pure dephasing with the pure dephasing rate γ_φ. Using the definition $\Gamma_2 = \frac{\Gamma_1}{2} + \gamma_\varphi$, this can be written in a shorter form:

$$\mathcal{L}[\hat{\rho}] = -\Gamma_1\hat{\sigma}_z\rho_e - \Gamma_2(\hat{\sigma}_+\rho_{eg} + \hat{\sigma}_-\rho_{ge}). \tag{3.20}$$

When substituting equations (3.20) and (3.17) into the master equation (3.18) and writing the $\hat{\sigma}$ terms in matrix form, we get

$$\frac{d\hat{\rho}}{dt} = \frac{i}{2}\begin{pmatrix} \Omega(\rho_{eg}-\rho_{ge}) & \Omega(\rho_e-\rho_g)+2\delta\omega\rho_{ge} \\ \Omega(\rho_g-\rho_e)-2\delta\omega\rho_{eg} & \Omega(\rho_{ge}-\rho_{eg}) \end{pmatrix} + \begin{pmatrix} \Gamma_1\rho_e & -\Gamma_2\rho_{ge} \\ -\Gamma_2\rho_{eg} & -\Gamma_1\rho_e \end{pmatrix}. \tag{3.21}$$

Rewriting the density matrix as a vector of length four, we can write a matrix $\mathbf{R}$ that captures the system dynamics as $d\hat{\rho}/dt = \mathbf{R}\hat{\rho}$.

$$\begin{pmatrix} \dot{\rho_g} \\ \dot{\rho_{ge}} \\ \dot{\rho_{eg}} \\ \dot{\rho_e} \end{pmatrix} = \frac{i}{2}\begin{pmatrix} 0 & -\Omega & \Omega & -2i\Gamma_1 \\ -\Omega & 2(i\Gamma_2+\delta\omega) & 0 & \Omega \\ \Omega & 0 & 2(i\Gamma_2-\delta\omega) & -\Omega \\ 0 & \Omega & -\Omega & 2i\Gamma_1 \end{pmatrix}\begin{pmatrix} \rho_g \\ \rho_{ge} \\ \rho_{eg} \\ \rho_e \end{pmatrix}. \tag{3.22}$$

Only three of the four equations are linearly independent. Since we have that $\langle\hat{\sigma}_+\rangle = \mathrm{Tr}[\hat{\rho}\hat{\sigma}_+] = \rho_{ge}$, $\langle\hat{\sigma}_-\rangle = \mathrm{Tr}[\hat{\rho}\hat{\sigma}_-] = \rho_{eg}$ and $\langle\hat{\sigma}_z\rangle = \mathrm{Tr}[\hat{\rho}\hat{\sigma}_z] = \rho_g - \rho_e$, we can reorder (3.22) to give the dynamics of the atomic operators:

$$\begin{pmatrix} \dot{\hat{\sigma}}_- \\ \dot{\hat{\sigma}}_+ \\ \dot{\hat{\sigma}}_z \end{pmatrix} = i\begin{pmatrix} -\delta\omega+i\Gamma_2 & 0 & \frac{\Omega}{2} \\ 0 & \delta\omega+i\Gamma_2 & -\frac{\Omega}{2} \\ \Omega & -\Omega & i\Gamma_1 \end{pmatrix}\cdot\begin{pmatrix} \hat{\sigma}_- \\ \hat{\sigma}_+ \\ \hat{\sigma}_z \end{pmatrix} + \begin{pmatrix} 0 \\ 0 \\ -i\Gamma_1 \end{pmatrix}. \tag{3.23}$$

These equations are known as the optical Bloch equations [Breuer02], and can be summarized as $\dot{\vec{\sigma}} = \mathbf{R}\vec{\sigma} + (0, 0, -i\Gamma_1)$, with $\vec{\sigma}$ the vector of expectation values $(\langle\hat{\sigma}_-\rangle, \langle\hat{\sigma}_+\rangle, \langle\hat{\sigma}_z\rangle)$, and $\mathbf{R}$ the matrix from equation (3.23). Solving for the steady state, we find that

$$\langle\hat{\sigma}_-\rangle_{ss} = i\frac{\Gamma_1(\Gamma_2 - i\delta\omega)\Omega}{2\Gamma_1(\Gamma_2^2+\delta\omega^2)+2\Gamma_2\Omega^2}. \tag{3.24}$$

We can now define the reflection and transmission coefficients (r and t) as $V_{\mathrm{sc}} = -rV_0$, and $V_0 + V_{\mathrm{sc}} = tV_0$, and therefore $r + t = 1$. This last equation might seem counterintuitive as this means that $|r|^2 + |t|^2 \neq 1$, meaning that power in the photonic mode at frequency ω is not conserved. However, as we started from the telegraph equations, the voltages need to obey the Kirchhoff laws, i.e., the current must be conserved.

To get an expression for the reflectance coefficient, we use that $\hbar\Omega = \phi_{\mathrm{tr}}V_0$ so that $V_{\mathrm{sc}} = -r\hbar\Omega/\phi_{\mathrm{tr}}$. The steady state solution for $\langle\hat{\sigma}_-\rangle$ given by (3.24) can then be substituted into equation (3.16), and after some rewriting we get

$$r = \frac{\Gamma_1}{2\Gamma_2} \frac{1 - i\delta\omega/\Gamma_2}{1 + (\delta\omega/\Gamma_2)^2 + \Omega^2/\Gamma_1\Gamma_2}. \tag{3.25}$$

We can now define two distinct decay channels for the qubit: γ_r will denote radiative decay, or decay into the transmission line. There will also be other sources for qubit decay, giving rise to a non-radiative decay γ_nr, where non-radiative does not mean the qubit does not radiate, but merely that the radiation is emitted into other channels than the transmission line. We can then define the ratio of emission into the transmission line compared to total emitted radiation as $\eta \equiv \gamma_\mathrm{r}/(\gamma_\mathrm{r} + \gamma_\mathrm{nr})$. The maximum reflection coefficient is then given by $r_0 \equiv \eta\Gamma_1/2\Gamma_2$. This quantity can be brought very close to one by ensuring a strong coupling between the qubit and the transmission line ($\gamma_\mathrm{r} \gg \gamma_\mathrm{nr}$). The expression for the reflection coefficient of the qubit now can be written in the same form as in [Astafiev10a]:

$$r = r_0 \frac{1 - i\delta\omega/\Gamma_2}{1 + (\delta\omega/\Gamma_2)^2 + \Omega^2/\Gamma_1\Gamma_2}. \tag{3.26}$$

If the pure dephasing rate $\gamma_\varphi = 0$ and $\eta = 1$, the reflection coefficient goes to 1. In other words, the scattered voltage which interferes destructively with the transmitted light (see figure 3.2), has the same magnitude as the input field, such that the destructive interference is complete, and all radiation is reflected. Thus, the qubit functions as a mirror. An obvious application of a single qubit is to make a single-photon router or switch, as also proposed in Astafievs pioneering paper on this topic [Astafiev10a] and realized by Io-Chun Hoi [Hoi11]. A nonzero pure dephasing rate will have the effect that the radiation loses its phase during the time it resides as an exciton in the artificial atom. Upon being emitted, the photon will interfere with the input field with a random phase. When this experiment is repeated, the dephased contribution to the radiation will average out, resulting in $|r|^2 + |t|^2 \neq 1$ – the reflected plus transmitted power do not add up to be equal to the input power. Similarly, when $\Omega \gg 0$, the artificial atom will get saturated, resulting in inelastically scattered radiation. This radiation will have a randomized phase and a different frequency than the input field, and is excluded from the expression for the reflection coefficient.

3.2 Experiments on one qubit in a transmission line

In the first part of this chapter we have seen how to understand the behaviour of a single qubit in an open one-dimensional space from a semi-classical point of view. In this chapter, that theory will be used to explain the experimentally observed behaviour of a transmon qubit in an open transmission line. We want to emphasize that these experiments were not done on a chip containing only one qubit. The interaction effects between qubits will be covered in the next chapters in this thesis, but for now it suffices to state that when multiple qubits are detuned from each other by a frequency much larger than their line width, their interactions can be ignored. An exception to this statement occurs when the qubit under investigation is tuned to frequencies higher than the ignored qubits. In such a case, these lower qubits can form weak standing modes with impedance mismatches in the lines (as discussed in chapter 2), and the harmonics of such standing modes can interact with the qubit under investigation. In this chapter, most of the presented results were measured on the sample which was also used for the paper [vanLoo13] published about two qubits in a transmission line, unless stated otherwise.

3.2.1 Characterizing the qubits

The first step in any experiment involves characterizing the system to be experimented upon. For a multi-qubit system, this involves finding the maximum frequencies of all qubits, their anharmonicities, and the mutual inductances to all the coils used for magnetic flux biasing, which is described in section 2.1. To find the maximum frequencies, the voltage on one of the coils is swept, preferably a coil that couples strongly to all qubits. Such a sweep can be seen in figure 3.3, from which the maximum frequencies were found to be 6.890, 6.835 and 6.310 GHz for the qubits labeled A, B and C respectively.

The anharmonicity of the qubits can be measured by performing continuous-wave two-tone spectroscopy. The qubit is tuned to its maximum frequency, and one microwave source is used to drive the $|g\rangle$-$|e\rangle$ transition continuously. This induces a population in the excited state, the amount of which depends on the drive strength and the relaxation rate. A second microwave source is used simultaneously to perform spectroscopy on the

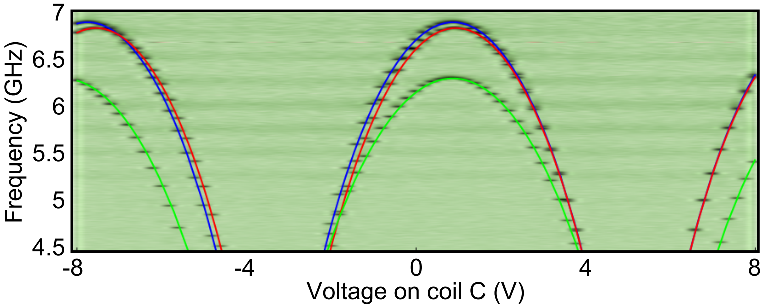

Figure 3.3: Sweeping a coil that couples to all qubits reveals their maximum frequencies. This picture was shown in chapter 2, and is repeated here for convenience.

$|e\rangle$-$|f\rangle$ transition. The anharmonicity α is given by the difference between these transition frequencies. To measure the anharmonicity, we can drive the $|e\rangle$-$|f\rangle$ transition strongly and look at the transmission of the $|g\rangle$-$|e\rangle$ drive tone, resembling an electromagnetically induced transparency experiment. Alternatively, the $|g\rangle$-$|e\rangle$ drive can be strongly driven while observing the transmission of a spectroscopy tone scanning over the $|e\rangle$-$|f\rangle$ transition (Fig. 3.4). The qubit anharmonicities were found to be 338, 337 and 341 MHz for qubits A, B and C respectively. From these numbers, the maximum Josephson energy E_J and the charging energy E_C were calculated; the Josephson energies were found to be 21.5, 21.2 and 18.2 GHz, while the charging energies were 302, 301 and 301 MHz for qubits A, B and C respectively.

3.2.2 Measuring the dipole moment of a transmon qubit

To investigate the various decay rates involved in the qubit dynamics, we can fit the spectrum of elastically scattered radiation with (3.26). The details of that will be discussed in section 3.2.3. However, the dipole moment of the qubit enters equation (3.26) as a parameter, and we will need to find a reliable value for it before we can fit qubit spectra. This dipole moment is given by equation (3.9), and after determining E_J and E_C, for which knowledge of the dipole moment is not needed, the only unknown variable

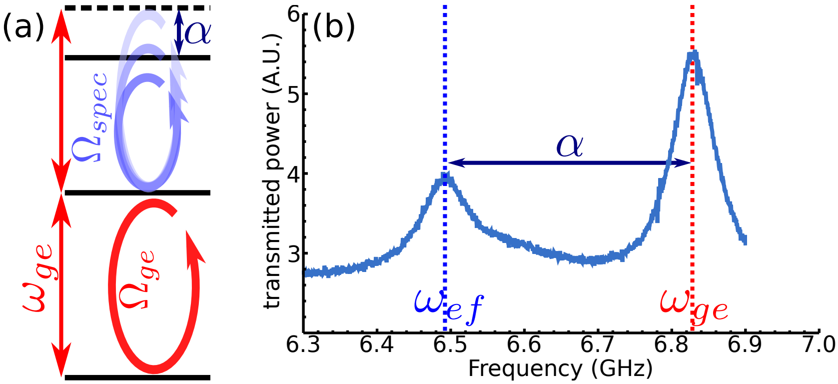

Figure 3.4: (a) The anharmonicity α is measured by means of continuous-wave two-tone spectroscopy: a drive is applied for the $|g\rangle$-$|e\rangle$ transition, and spectroscopy is performed simultaneously on the $|e\rangle$-$|f\rangle$ transition. (b) Both the $|g\rangle$-$|e\rangle$ transition and the $|e\rangle$-$|f\rangle$ transition are visible in a two-tone measurement, with the $|e\rangle$-$|f\rangle$ transition appearing at $\omega_{ge} - \alpha$.

in this equation is β, which is a combination of capacitances determined by the design of the transmon [Koch07].

To determine β, we can use the fact that Γ_1 depends on both ω and the dipole moment ϕ_{tr}. When transmittance is measured at low powers ($\Omega \ll \Gamma_1$), the line width is a good indicator for the relaxation rate of the qubit. Using the inverted coil matrix (see section 2.1), the qubit was moved in a straight line through frequency space as shown in figure 3.5. The transmittance dip was fitted with (3.26) using that $|t|^2 = |1-r|^2$, and using an initial guess for β according to the design of the transmon used in these experiments. These fits result in a series of values for Γ_1 as a function of frequency, which can be fitted with the equation for Γ_1 as a function of frequency (3.15), where β is the fitting parameter. The data and fit are shown in Fig. 3.6. This new value of β is then used anew to fit the qubit spectra, giving a new set of values for Γ_1 as a function of frequency. This process of fitting the qubit line shape and $\Gamma_1(\omega)$ is performed iteratively until the value of β converges. This way, we found that $\beta = 0.151$.

Except for providing a value for β, Fig. 3.6 shows another interesting

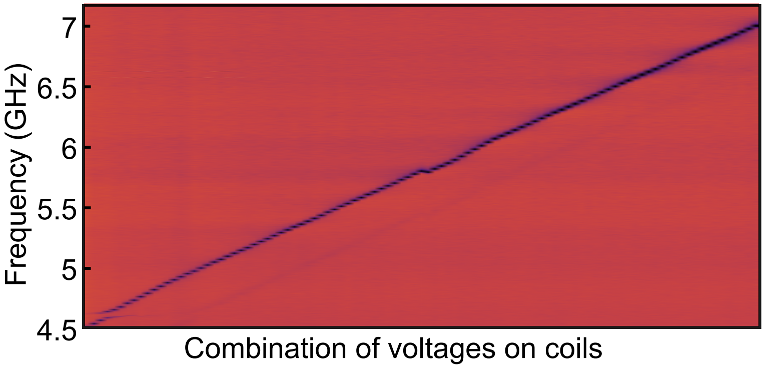

Figure 3.5: The qubit was shifted through frequency space in a straight line (except for the kind in the center of the figure) while the other qubits were tuned out of range. This was done using a combination of voltages on the three coils calculated from the mutual inductance matrix between qubits and coils. The background was subtracted. Red means the transmission is close to 1, while dark blue is close to zero.

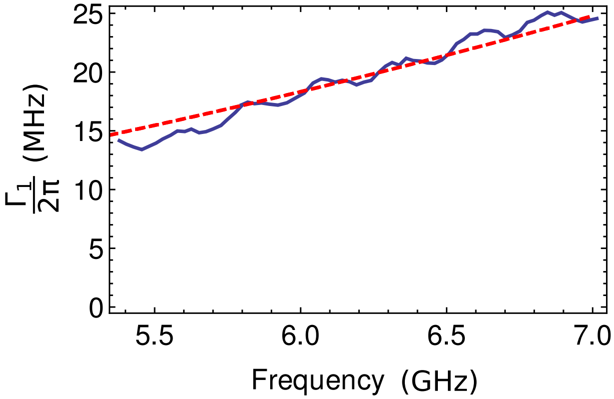

Figure 3.6: Γ_1 is fitted using equation (3.26) for transmittance peaks at different frequencies. The resulting line is then fitted to find ϕ.

feature. We observe that Γ_1 behaves differently as a function of frequency than expected; it fluctuates around the theoretically expected relaxation rate. These fluctuations are probably caused by weak standing waves in our experimental setup as a result of parts that are not perfectly impedance matched. The ripples in Fig. 3.6 are consistent with the ripples observed in background measurements shown in Fig. 2.12 in chapter 2, supporting the hypothesis that they are caused by standing modes in the microwaves lines. The fluctuations have a wavelength of $\sim$ 265 MHz, which corresponds to a piece of transmission line of 0.75 m if the speed of light in the coaxial cables is assumed to be $2c/3$ with c the speed of light in vacuum. The source of these standing waves was not found during the experiments. There are a few equivalent ways for interpreting this effect in a way that ties in with our theoretical description of a qubit in a transmission line. It would for example be valid to say that the impedance causing Johnson Nyquist noise – so far assumed to be a $50\,\Omega$ resistor at a certain temperature – has an effective resistance that fluctuates around 50 Ω with frequency due to impedance mismatches in the lines. The interpretation we prefer, though, is that the density of states observed by the qubit is a function of frequency. It should also be pointed out here that due to the nature of standing waves, this fluctuating density of states is expected to be different for qubits at a different position.

3.2.3 The spectral shape of a qubit

Theoretically, the line shape of a qubit is determined by equation (3.26). In Fig. 3.7, the qubit transmittance and reflectance are shown at various drive powers, for a qubit tuned to its maximum frequency. The powers quoted in the figure are the drive powers at the qubit. Fitting the qubit shape with (3.26) reveals information about the properties of the qubit. The maximum peak in reflectance indicates the strength of the coupling: the pre-factor in formula (3.26), $\eta\Gamma_1/(2\Gamma_2)$ determines the maximum reflection at resonance. As a reminder, η is given by the emission rate of the qubit into the transmission line divided by the total qubit emission rate: $\eta \equiv \gamma_{\mathrm{r}}/(\gamma_{\mathrm{r}} + \gamma_{\mathrm{nr}})$. These decay mechanisms are related to the observed qubit lifetime as $\Gamma_1 = \gamma_{\mathrm{r}} + \gamma_{\mathrm{nr}}$. The ratio $\Gamma_1/2\Gamma_2$ indicates the effect of pure dephasing, as is clear from the definition $\Gamma_2 \equiv \Gamma_1/2 + \gamma_{\varphi}$. The pre-factor giving the maximum reflection coefficient at zero drive power, r_0, can

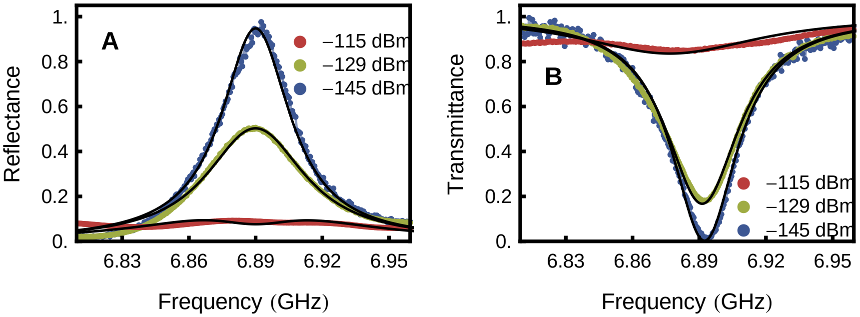

Figure 3.7: The reflectance (a) and transmittance (b) of a single qubit at its sweet spot at 6.89 GHz.

then be written out in the various decay rates as $r_0 = \gamma_{\mathrm{r}}/(\gamma_{\mathrm{r}} + \gamma_{\mathrm{nr}} + 2\gamma_{\varphi})$.

A striking feature in figure 3.7 is that the transmittance approaches zero at low drive powers. Similarly, the reflectance almost reaches unity for the qubit tuned to its sweet spot. The very high reflection coefficient of a qubit in a transmission line makes it a useful tool for quantum communication: the qubit can be used as a switchable mirror. Using a charge gate to switch the qubit between ground and excited state, the qubit can be made to reflect or transmit on demand. This effect was used in [Hoi11] to implement a single-photon router using a qubit and a circulator. It should be emphasized that in their experiment, low-power coherent tones were reflected or transmitted by the qubit, rather than the single photons one might be led to expect from the words ”single-photon router”.

The qubit peaks in Fig. 3.7 seem to have a Lorentzian shape, but, as we can see from (3.26), the expression for the reflectance $|r|^2$ of the spectrum deviates from that of a Lorentzian. Non-radiative decay, pure dephasing and drive power all have the effect of making the peak more blunt than a Lorentzian peak, and these effects are very hard to distinguish. To still get a good estimate for the pure dephasing rate of a qubit and its relaxation rate we used a somewhat elaborate fitting procedure, in which we assumed the non-radiative decay rate to be negligible ($\eta = 1$). This assumption will be validated later in this thesis.

To extract information about the various qubit decay rates at any fixed transition frequency, we measure the reflectance and/or transmittance as a function of power, resulting in traces such as seen in Fig. 3.7. As the background transmittance and reflectance scale with power in a not completely linear manner (the reason for that remains unknown), the background was subtracted separately at each drive power. After that, a three-step method is used for getting reliable information out of the fits. In the first step, the drive power Ω in equation (3.27) is fixed to the experimentally used drive power, and Γ_1, γ_φ and ω_{ge} are fitted using equation (3.26), which we repeat here for convenience:

$$r = \frac{\eta\Gamma_1}{2\Gamma_2}\frac{1 - i\delta\omega/\Gamma_2}{1 + (\delta\omega/\Gamma_2)^2 + \Omega^2/\Gamma_1\Gamma_2}. \tag{3.27}$$

In the second step, ω_{ge} is fixed as per the fit of step one, and it is assumed that the pure dephasing rate γ_φ does not vary with the drive power. At drive powers low enough such that the transmittance peak amplitude does not change with power, the transmittance peak shape (i.e., its width compared to its maximum amplitude, not the maximum amplitude itself) does not depend on pure dephasing. Γ_1 is expected to be constant at a single frequency, and is extracted by fitting these low-power transmittance curves. The pure dephasing rate is subsequently obtained from low-power reflectance measurements. A third step is used to check if the obtained values are consistent: fits are done for transmittance curves at different drive powers keeping the dephasing rate and relaxation rate constant at the values extracted in step 1, while using the drive power Ω as a fit parameter. If the extracted drive rates are correct, the step size in Ω from the fits should be the same as the step size in drive power set at the microwave source. If these step sizes are not consistent, the dephasing rate is changed iteratively until this condition is satisfied. When the stepsize of the applied drive power and drive power found from fits is consistent, we can also obtain the total attenuation between the microwave source and the qubit, as it is given by the offset between fitted drive rates and the experimentally applied drive powers.

Using this fitting method, the data in figures 3.7, 3.8 and 3.9 reveals that the relaxation rate is $\Gamma_1/2\pi = 13 \pm .3$ MHz at 4.8 GHz, 26 ± 1 MHz at 6.4 GHz and 33 ± 1 MHz at 6.89 GHz. From equation (3.15), the relaxation rates are expected to increase by a factor 1.75 rather than a factor 2 between 4.8 GHz and 6.4 GHz. The difference is attributed to weak standing

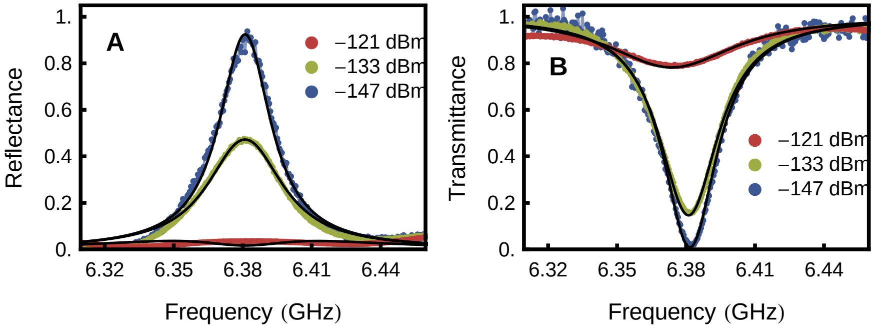

Figure 3.8: The reflectance (a) and transmittance (b) of a single qubit at 6.4 GHz at various powers.

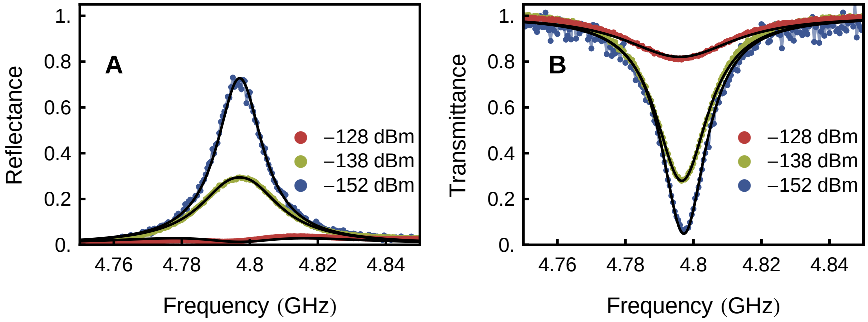

Figure 3.9: The reflectance (a) and transmittance (b) of a single qubit at 4.8 GHz at various powers.

modes in the transmission line, causing a non-flat density of states as was discussed in section 3.2.2. The pure dephasing rate is found to be approximately 1 MHz at 6.4 GHz and 1.5 MHz at 4.8 GHz.

Dephasing can be caused by slow fluctuations in the magnetic field: the fluctuations in magnetic field cause changes in the qubit transition energy, which in turn changes the Larmor precession frequency. Unknown changes in this frequency cause unknown phases at the end of an experiment, when these fluctuations are slower than the duration of one trace in the experiment. Given a source of magnetic fluctuations, the dephasing rate depends on how strong the magnetic fluctuations influence the qubit transition frequency. For transmon qubits, $d\omega_{ge}/d\phi$ is higher at lower transition frequencies, and therefore the dephasing rate is expected to be higher at lower qubit frequencies, which is indeed observed.

There is a way to obtain a lower bound on η. Since qubit dephasing is minimal when $d\omega/d\phi$ is minimal, tuning the qubit to its sweet spot minimizes qubit dephasing. When driving the qubit at very low power and at resonance, the reflectance is given by $r = \eta\Gamma_1/(2\Gamma_2)$, or $r = \gamma_{\mathrm{r}}/(\gamma_{\mathrm{r}} + \gamma_{\mathrm{nr}} + 2\gamma_\varphi)$. In Fig. 3.7A we see that the maximum reflectance is higher than 0.94. This implies that the maximum reflection coefficient exceeds 0.97. Assuming that γ_φ is zero at the qubit sweet spot (an assumption we know not to be valid, but which we will take here in order to find an upper bound on γ_{nr}), we have that $\eta > 0.97$. As η denotes the ratio of radiation emitted by the qubit into the transmission line rather than into other channels, we have that $\eta = \gamma_{\mathrm{r}}/(\gamma_{\mathrm{r}} + \gamma_{\mathrm{nr}})$. Having a lower bound for η thus gives us an upper bound for the non-radiative decay: $\gamma_{\mathrm{nr}} < 0.03\Gamma_1 \approx 1$ MHz.

Another way to quantify the coupling strength between a two-level system and a one-dimensional space is given by the Purcell factor for one dimension as defined in [Chang07]: $P_{1\mathrm{D}} \equiv \gamma_{\mathrm{r}}/\gamma_{\mathrm{nr}} = \eta\Gamma_1$. The upper bound on γ_{nr} now translates into a lower bound on the Purcell factor: $P_{1\mathrm{D}} > 33$. We would like to stress here that we do not expect γ_{nr} to be close to this upper bound, as we know that $\gamma_\varphi \neq 0$. We do expect γ_φ to be close to zero, as the high relaxation rate of our system dictates that $\gamma_\varphi \ll \Gamma_1$, but as it is also true that $\gamma_{\mathrm{nr}} \ll \Gamma_1$, our estimate for the non-radiative decay rate is very sensitive to the pure dephasing rate being nonzero. When investigating a two-qubit system, we will have an opportunity to get a better estimate for γ_{nr}.

The same reasoning can be applied to the transmittance data in Fig. 3.7B. However, there we find that the minimum transmittance $|t|^2$ is about 1.7%, from which we find that $t_{min} = 0.13$, and a Purcell factor $\Gamma_1/\gamma_{\mathrm{nr}} > 7.6$. The reason for the disparity in estimates for γ_{nr} and $P_{1\mathrm{D}}$ is believed to be due to the noise which is added to the signal. In an ideal measurement of elastically scattered radiation, after averaging, the expectation value of the noise in the signal is $\langle h \rangle = 0$. However, when averaging for only a finite amount of time, there will be some contribution to the measured signal by the noise. In our measurements we look at either the absolute amplitude of the signal $\sqrt{I^2+Q^2}$ or the power I^2+Q^2. The signal we expect to measure is a fluctuating voltage due to the transmitted radiation. The power transmitted by any system is always positive. However, the added voltage due to noise can be either positive or negative. As long as the measured signal is larger than zero by more than a few standard deviations of the noise, the observed signal will fluctuate randomly around the expected signal. However, if the signal gets very close to zero (to within a standard deviation of the noise), our method of calculating the signal amplitude as $\sqrt{I^2+Q^2}$ backfires. Suppose we measure the transmitted signal as a function of time, and that we have exactly zero transmission. In that case the noise fluctuates around zero. As we take the absolute amplitude of this measured signal, these fluctuations will show up as positive, and the averagely measured signal will therefore also be positive. Similarly, for signals very close to zero, the noise will add a finite and positive contribution to the signal. Due to the noise setting a lower limit to the minimum transmittance observed, it limits the lower bound on the Purcell factor as calculated from the minimum transmittance.

In Fig. 3.10, the amplitude of the dip in transmittance is fitted for different powers at 4.8 GHz (panel a) and 6.4 GHz (panel b). The points in the figure show the fitted maximum reflectance and transmittance amplitudes. At each power, a single-qubit spectrum was fitted with equation (3.27) to find the maximum in reflectance or minimum in transmittance. The line through them is another fit using equation (3.27) for the power-dependence of this dip. We observe that at low powers, the transmittance dip amplitude is constant and very close to unity (i.e., the transmittance is close to zero). As the drive power increases, the transmittance dip decreases, until the transmittance finally is equal to its baseline of 1 (i.e., the transmittance dip amplitude is zero). This phenomenon can be understood by considering that the qubit is a quantum two-level system: once the qubit has absorbed a photon from the coherent drive tone, the qubit is in the excited state. When the qubit is in the excited state, it cannot absorb another photon of the same frequency, as the system is anharmonic (it can however absorb photons at different frequencies, as was shown in the two-tone measurements used to determine the anharmonicity). The qubit will be able to absorb another photon at the same frequency when it has relaxed into the ground state by emitting a photon at its transition frequency. In other words, the amount of radiation that is maximally scattered by the qubit is bound by its relaxation rate Γ_1. In figure 3.10 this manifests as follows: at very low drive powers ($\Omega \ll \Gamma_1$), all of the incoming radiation can be absorbed and re-emitted by the qubit. When the drive power approaches the relaxation rate, the stochastic nature of spontaneous emission dictates that there will be incidences in which the qubit is still excited when the second photon arrives, such that some of the photons will be transmitted. However, when $\Omega \gg \Gamma_1$, the qubit will not be able to scatter radiation at a rate higher than Γ_1, and therefore the dip size in transmittance will start to decrease, and eventually, under a very strong drive, the scattering rate of the qubit becomes negligible compared to the rate of incoming photons such that the transmittance dip vanishes.

The main difference observed between panels a and b in Fig. 3.10 is the different level at which the reflectance saturates when $\Omega \ll \Gamma_1$. The maximum reflectance is mainly given by the ratio $(\Gamma_1/(\Gamma_1 + 2\gamma_\varphi))^2$, assuming that η does not vary very strongly with frequency. When comparing this ratio for qubits at 4.8 GHz and 6.4 GHz, we see that at the former frequency the pure dephasing rate is higher while the relaxation rate is lower, both of which contribute to a lower maximum reflectance.

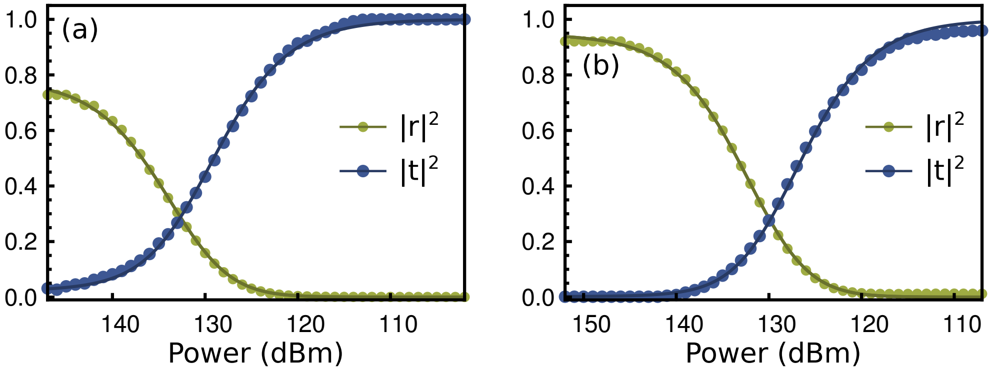

Figure 3.10: Reflectance and transmittance as a function of power at 4.8 GHz (a) and 6.4 GHz (b). Lines are fits with equation (3.26). Note that the x-axes do not have the same range.

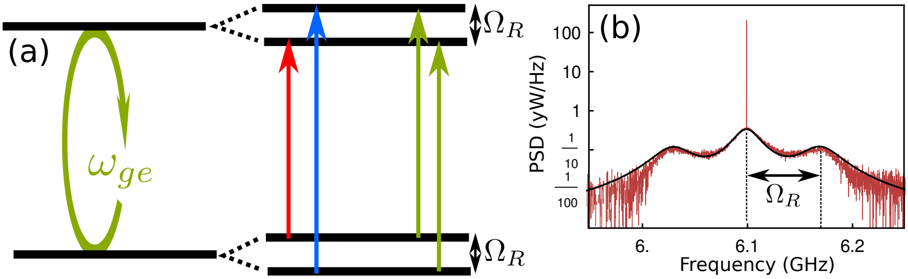

Figure 3.11: (a) A strong coherent tone splits a two-level system into four levels. (b) The power spectral density (PSD) of a strongly driven two-level system results in a Mollow triplet. The black line is a fit with theory, and the sharp peak in the center is the elastically scattered drive tone.

3.2.4 Resonance fluorescence of a single artificial atom

When a two-level system is strongly driven by a coherent field, its two levels ($|g\rangle$ and $|e\rangle$) split into four levels (Fig. 3.11a). This splitting is also often referred to as 'dressing' the qubit states with the coherent drive tone. Within those four levels, the only transitions allowed are those preserving the number of total excitations (atomic and photonic combined), leaving four allowed transitions. Of these four, two have the same frequency as the $|g\rangle$-$|e\rangle$ transition of the qubit (green arrows in Fig. 3.11a), while the other two transitions differ from ω_{ge} by Ω_R and $-\Omega_R$, which is the drive strength or Rabi flopping rate (blue and red arrows in Fig. 3.11a). This results in a three-peak structure known as the Mollow triplet, after the person who first calculated the resonance fluorescence spectrum of a two-level system [Mollow69]. A derivation of the expected shape of the Mollow triplet can be found in any quantum optics text, such as [Scully97, Yamamoto99, Loudon00]. Here we choose to use the same expression as used in Astafiev's paper [Astafiev10a], as that form explicitly includes the qubit dephasing rate.

$$S(\omega) = \frac{1}{2\pi}\frac{\hbar\omega\Gamma_1}{8}\left(\frac{\gamma_s}{(\delta\omega+\Omega_R)^2+\gamma_s^2}+\frac{2\gamma_c}{\delta\omega^2+\gamma_c^2}+\frac{\gamma_s}{(\delta\omega-\Omega_R)^2+\gamma_s^2}\right), \tag{3.28}$$

with $\gamma_s \equiv (\Gamma_1 + \Gamma_2)/2$ the width of the side peaks and $\gamma_c \equiv \Gamma_2$ the width of the main peak. It should be noted that this expression is only valid for strong drives ($\Omega_R > \Gamma_1$), and for a two-level systems. For a weakly anharmonic oscillator such as the transmon, this expression can therefore only be used when $\Gamma_1 < \Omega_R \ll \alpha$.

In Fig. 3.12, the Mollow triplet is shown at different drive powers, showing the dependence of the location of the sidebands on drive power. In this figure, the Rabi rate was fitted for only one curve. Knowing the Rabi rate and the drive power for a single curve, the Rabi rates for the other curves could be calculated from the drive powers. We see in Fig. 3.12 that the measured data shows the same power dependence as the calculated curves, except when $\Omega_R \leq \gamma_s$, where equation (3.28) is invalid.

Measuring the Mollow triplet serves an additional purpose: calibrating the applied power at the qubit. While care can be taken to measure the attenuation in the lines as precisely as possible using a network analyzer, the attenuation of the lines and microwave components changes when the cryostat is cooled down. However, by performing a resonance fluorescence measurement and fitting the outcome with (3.28), the drive power applied to the qubit can be extracted from fitting for the Rabi rate. In the remainder of this thesis, the drive strength will sometimes be stated in MHz instead of dBm. In those cases, a single-qubit Mollow triplet was measured and fitted with (3.28) at the frequency of the experiment to extract which drive power was experienced by the qubit.

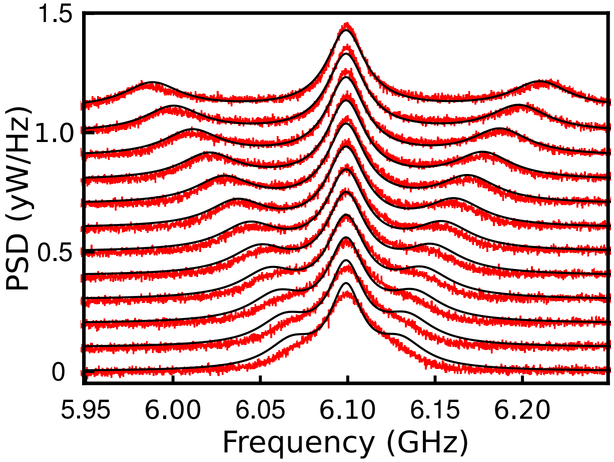

Figure 3.12: Resonance fluorescence of a single artificial atom at different drive powers. The Rabi rate was fitted for one curve, for the other curves the Rabi rate was calculated from the drive power. Red lines are data, black lines theory.

4 Elastic scattering properties of a system of multiple qubits

While the behaviour of single qubits in a transmission line is very interesting, it has already been investigated thoroughly [Astafiev10a, Abdumalikov10, Abdumalikov11, Hoi11, Hoi12, Hoi13a, Hoi13b, Koshino13]. Our work departs from other experimental work for qubits in a transmission line by looking at more than a single qubit. As qubit-qubit interactions are expected to be strongest when the qubits are in resonance, we focus on experiments for qubits close to or in resonance. We start by showing how two qubits behave when tuning them into and out of resonance, and then look at the behaviour of the two-qubit system in resonance. We focus on the qubit frequencies of 4.8 GHz and 6.4 GHz, as these frequencies are equivalent to an effective inter-qubit distance of $3\lambda_r/4$ and λ_r, with λ_r the wavelength of a mode resonant with the qubits (Fig. 4.1), which is where we intuitively expect to see extrema in qubit interaction phenomena. After showing the experimental observations, we discuss two semi-classical models which treat the single qubits as separate quantum systems and takes the interference of the radiation emitted by them into account. These models are used to explain the experimentally observed phenomena.

4.1 Elastic scattering properties for a system of two distant artificial atoms

To investigate the interaction effects for two (or more) qubits, the first experiment is to tune those qubits into resonance, do spectroscopy and observe if an avoided level crossing emerges between the qubit lines. The result of such an experiment at intermediate drive powers is shown in Fig. 4.2. Both qubits were placed at either 4.8 or 6.4 GHz. A coil was chosen that couples much more strongly to one qubit than the other, and the current

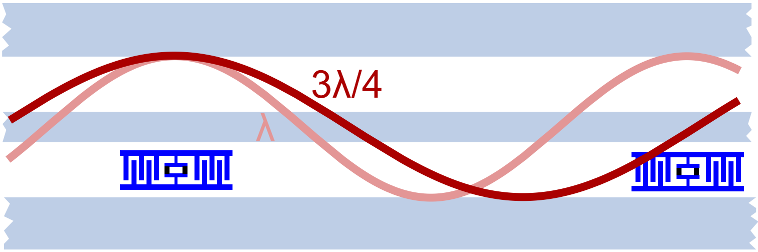

Figure 4.1: In experiment, we cannot change the physical distance between qubits. Instead, we change the frequencies of both qubits, keeping them in resonance, which changes the effective distance – the distance expressed in numbers of wavelengths λ_r, where λ_r is the wavelength of radiation in resonance with the qubits.

through this coil was varied. Hence, one qubit – the one that does not couple strongly to the coil used – is almost fixed in frequency, while the other qubit is tuned from slightly below to slightly above that frequency, resulting in Fig. 4.2.

There are several features in this figure that need explaining. First, the situation seems very different when looking at Figs. 4.2B and D. Whereas in Fig. 4.2B it seems that $|r|^2 + |t|^2 = 1$, in Fig. 4.2D this is obviously not the case. These measurements were done at the same output drive power of the microwave source: -24 dBm at both 4.8 GHz and 6.4 GHz. However, this results in a very different effective drive power for both qubits due to two reasons. The first reason is that the attenuation in the lines is approximately 5 dBm lower at 4.8 than at 6.4 GHz - the drive power at the qubit positions at 4.8 GHz for this experiment is estimated to be -131 dBm, while it is -136 dBm at 6.4 GHz. These rates can be expressed in MHz by measuring a power spectral density for the qubits at high drive, and extracting the Rabi rate from the separation between center and side peaks in the observed Mollow triplet. This has to be done at the same drive frequencies as the measurement for which the power is to be converted to MHz was done at (this procedure was explained in more details in section 3.2.4). The drive rates are found to be 8.7 MHz for qubits tuned to 4.8 GHz, and 7.5 MHz when the qubits are at 6.4 GHz. When discussing the behaviour of a qubit in an open transmission line, a more convenient quantity for de-

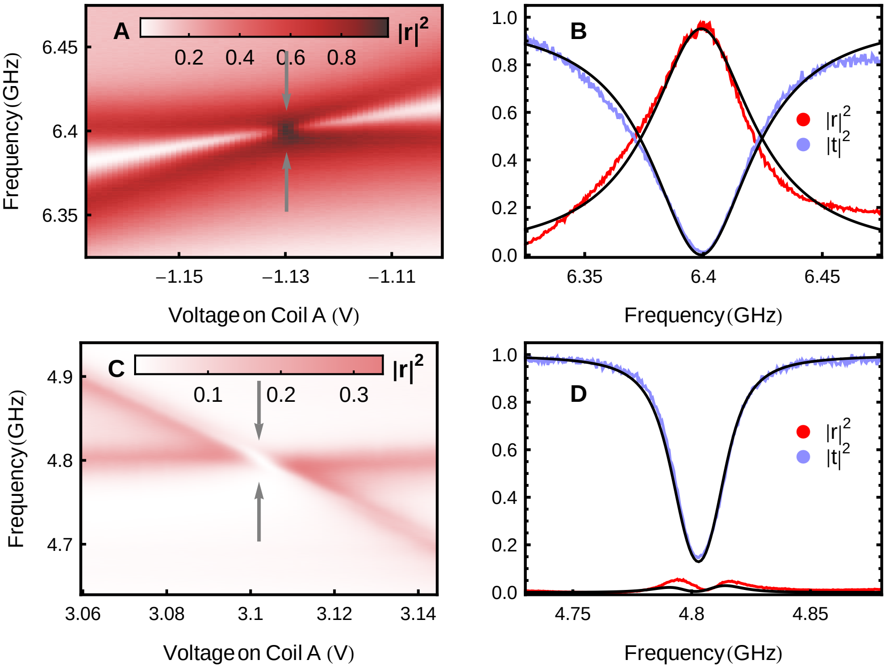

Figure 4.2: Reflectance spectra $|r|^2$ of the two-qubit system at (A,B) $d \sim \lambda_r$ and at (C,D) $d \sim 3\lambda_r/4$ (red data sets). In (B,D) the transmittance $|t|^2$ is also shown (blue data sets). In panels (A,C), the frequency of one qubit is tuned by applying the indicated voltages to mm size coils integrated in the sample mount while the other qubit is kept at a fixed frequency. Close to resonance, interference effects cause the qubit peaks to become asymmetric. (B,D) show spectra at coil voltages indicated by arrows in (A,C). Colored lines are data. Black lines are theory, see text for details.

scribing drive power is Ω_R/Γ_1, as the ratio of these rates shows how close to qubit is to being saturated – its value is an indicator for what fraction of the radiation gets scattered inelastically rather than elastically. As the decay rates are $\Gamma_1^{4.8}/2\pi = 13$ MHz and $\Gamma_1^{6.4}/2\pi = 26$ MHz, we find dimensionless drive strengths of 0.67 and 0.29 at 4.8 and 6.4 GHz respectively.

The latter number being low means that a relatively large amount of light gets scattered elastically such that $|r|^2 + |t|^2 \sim 1$. The much higher drive strength at 4.8 GHz means that a significant fraction of the radiation will be scattered inelastically, such that $|r|^2 + |t|^2$ do not add up to one. The split peak observed in the same figure is due to a dressing the two-qubit system by the strong drive, not a signature of qubit-qubit interaction.

Both in Fig. 4.2B and D, the peak shapes of the qubits are asymmetric. This asymmetry is caused by a small detuning between the qubits. When tuning the frequency of one of the qubits by varying the voltage over a coil, the finite step size of the voltage source results in a finite step size in qubit frequency. Thus, the qubits were very close to resonance at the spots indicated by arrows in Figs. 4.2A and C, but not exactly in resonance, resulting in a slightly asymmetric peak shape. We will investigate if a small detuning leads to the observed asymmetry by simulation in section 4.2.

The reflectance and transmittance away from qubit resonance, which should be 0 and 1 respectively (we will refer to this as the 'baseline'), is highly asymmetric around the qubit in Fig. 4.2B. This was a recurring problem with measurements at high qubit frequencies. Due to the limited maximum frequencies of the qubits in the sample under investigation, the qubits could not be tuned above the range of interest during a background measurement. Instead, the qubits had to be tuned to frequencies below the range of interest. The qubits, being themselves small impedance mismatches in the transmission lines, then form weak standing waves with other impedance mismatches in the circuit. These weak standing modes will therefore be measured in the background measurement but not in the experiment with the qubits tuned to the frequencies of interest. The measured background is therefore different from the background during the experiment. This is thought to be the main cause for the slanted baseline in Fig. 4.2B.

Finally, Fig. 4.2 is not completely symmetric around the qubits in resonance, mostly so in Fig. 4.2A. This is because the qubits do not move in straight lines through the figure, but instead as $\omega \propto \sqrt{\cos(V)^2}$, with V the voltage on the coil.

An experiment was carried out to determine the power arriving at the right qubit when driving two qubits in resonance from the left. It might first be naively assumed that the power at qubit B is given by $|t_1|^2 P_{in}$, but due to the possibility of multiple reflections between the qubits, this is not the case. The transmittance and reflectance of qubit A and qubit B

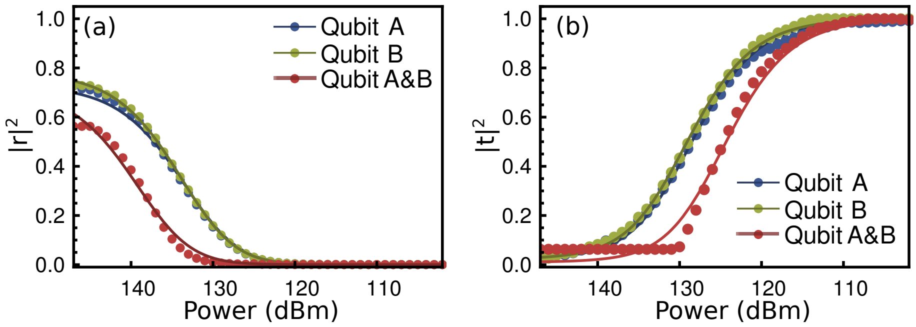

Figure 4.3: Reflectance (a) and transmittance (b) for qubit A, qubit B, and for both qubits in resonance at 4.8 GHz. As fit parameters, we used $\Gamma_1^A/2\pi = \Gamma_1^B/2\pi = 13$ MHz, and $\gamma_\varphi^A/2\pi = \gamma_\varphi^B/2\pi$=1.4 MHz.

were separately measured as a function of drive power and frequency. After that, both qubits were tuned into resonance, and the reflectance and transmittance of the two-qubit system were measured versus drive power and frequency (Figs 4.3 and 4.4). This was done both at 4.8 GHz and 6.4 GHz. For each point in these figures, a transmittance or reflectance curve was measured as a function of drive frequency at a single drive power, and fitted with the formula for reflection (3.26) to find the maximum reflectance or transmittance. This was done for various drive powers to see how the maximum reflectance and transmittance depend on drive power. The resulting curve was fitted once again using equation (3.26), now fitting only for an offset drive power and pure dephasing. The two-qubit spectra (red in the figures) do not have the same shape as a single-qubit reflection curve, resulting in a bad match between the fit and the data.

For two qubits tuned to 4.8 GHz (Fig. 4.3) the two-qubit peak has a lower transmittance and reflectance at a given power when compared to single qubit numbers. The lower transmittance is expected, as there are now multiple locations at which light can be reflected. The lower reflection is more surprising, and is thought to be due to interference: radiation transmitted by qubit A and reflected by qubit B will accumulate a phase of 3π, and will therefore interfere destructively with the directly reflected radiation.

When looking at qubits tuned to 6.4 GHz, radiation transmitted by the

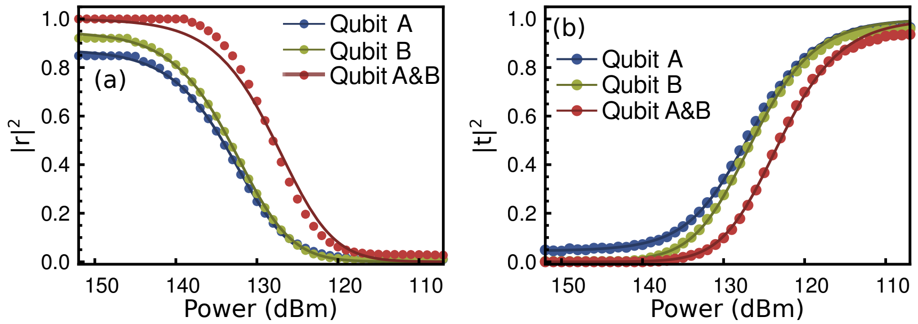

Figure 4.4: Reflectance (a) and transmittance (b) for qubit A, qubit B, and for both qubits in resonance at 6.4 GHz. $\Gamma_1^A/2\pi = 28$ MHz, $\Gamma_1^B/2\pi = 26$ MHz, $\gamma_\varphi^A/2\pi = 0.9$ MHz, $\gamma_\varphi^B/2\pi = 0.4$ MHz.

first and reflected by the second qubit accumulates a phase of 4π, and is therefore expected to interfere constructively with the input field. In Fig. 4.4(a), we see that the reflectance of the two-qubit system is indeed increased compared to single qubits, while transmittance is decreased.

4.2 Multiple qubits in a transmission line: interference effects

Assuming that cooperative two-qubit effects are caused by interference, we can construct a semi-classical model to simulate the transmittance and reflectance of a two-qubit system. We use the steady-state solution of the master equation presented in section 3 to find the reflection and transmission of a single qubit, and construct a scattering matrix for a single qubit. We also construct a scattering matrix for the fixed distance between the two qubits. These scattering matrices can then be transformed to transfer matrices, which have the convenient property that they can be multiplied to give an equivalent two-port system for all components combined. Therefore, the reflection and transmission coefficient of the total system can be obtained from the product of transfer matrices of all subsystems. This approach was inspired by references [Shen05b, Shen05a], but our approach differs in that we do not assume our systems to be lossless, and we allow

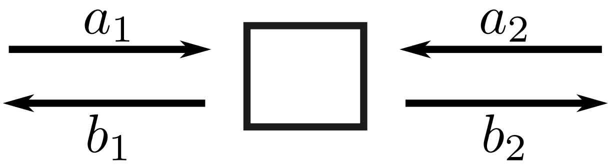

Figure 4.5: The scattering matrix couples outputs b_1 and b_2 to inputs a_1 and a_2.

for high input powers.

4.2.1 Scattering matrices

A scattering matrix connects the outputs of a two-port network to its outputs according to

$$\begin{pmatrix} b_1 \\ b_2 \end{pmatrix} = \begin{bmatrix} S_{11} & S_{12} \\ S_{21} & S_{22} \end{bmatrix} \begin{pmatrix} a_1 \\ a_2 \end{pmatrix}. \tag{4.1}$$

where all variables are as in Fig. 4.5. To construct a scattering matrix for an object, we need to know its reflection and transmission coefficient. The reflection coefficient for radiation coherently scattered by a two-level system in a transmission line is given by (3.26), and the transmission coefficient is $t = 1 - r$.

For a single qubit, we have that $S_{11} = S_{22}^* = -r$, and $S_{12} = -S_{21}^* = t$. To investigate interference effects between two distant qubits, we also need a scattering matrix for this distance, as the applied radiation acquires a phase between the qubits that depends on this distance. The scattering matrix for the distance between the qubits is given by $S_{11} = S_{22} = e^{i2\pi\omega/\omega_d}$, and $S_{12} = S_{21} = 0$. Here ω is the frequency of the input field, and $\omega_d = 2\pi v/d$ is the frequency whose corresponding wavelength is equal to the distance between the qubits.

4.2.2 Transfer matrices

Even when the scattering matrices for all parts of a system are known, it is not trivial to calculate the reflection and transmission coefficients of the total system. Each scattering matrix can however be transformed into a so-called transfer matrix, and these transfer matrices can be multiplied to give the total system response (see Fig. 4.6 for a schematic). To calculate the reflection and transmission of a multi-qubit system, therefore, we need but find the transfer matrices of all components. For a qubit, the transfer matrix has the following shape [Shen05a]:

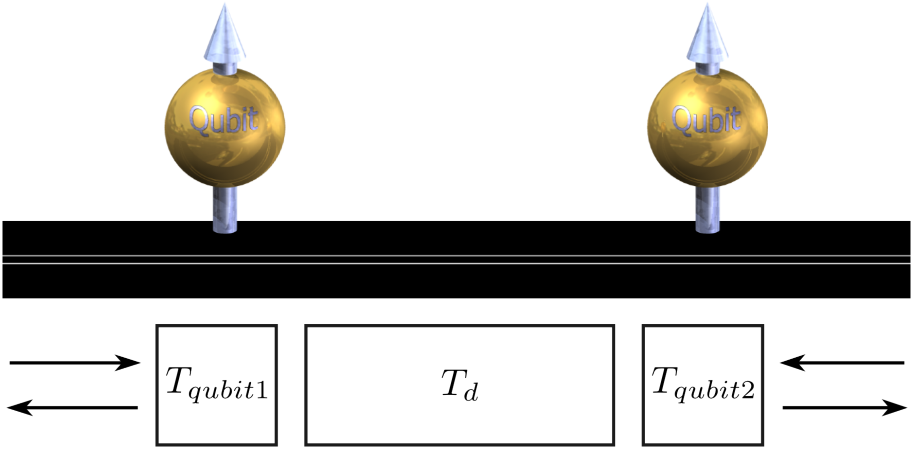

Figure 4.6: The single qubits and the distance between them can each be characterized by a transfer matrix. The product of transfer matrices is equal to the transfer matrix of the total system.

$$T_q = \begin{bmatrix} \frac{|r|^2+|t|^2}{t^*} & \frac{r^*}{t^*} \\ \frac{r}{t} & \frac{1}{t} \end{bmatrix}, \tag{4.2}$$

with $r(\omega, \Omega)$ as in equation (3.26), and $t = 1 - r$. It should be noted here that there are some differences between the definitions we use here and those used in [Shen05b]. In their paper, Shen *et. al.* construct a scattering matrix for a two-level system that is unitary. However, there are three conditions under which we do not expect the scattering to be unitary: when the pure dephasing rate $\gamma_\varphi \neq 0$, part of the radiation couples into the environment, leading to losses. Pure dephasing will cause the scattered radiation to be out of phase with the incoming beam, causing a random phase that is averaged out under multiple measurements, and therefore to a loss in the total amount of detected radiation. Similarly, a nonzero non-radiative decay rate will lead to loss of radiation out of the system. Moreover, when driving the system with $\Omega \not\ll \Gamma_1$, inelastic scattering will start to become important – radiation will be scattered at different frequencies than the drive frequency, and due to the randomized phase and the different frequency of inelastically scattered light these contributions will not be observed, again causing a loss of the total amount of observed radiation. Each of these effects means that our transfer matrix should not be unitary. This is implemented in the transfer matrix by the multiplication of T_{11} with $|r|^2 + |t|^2$.

Moreover, we differ from [Shen05b] in the locations of minus signs in (4.2), but this is merely due to a difference in the definition of the reflection coefficient r, for which we have chosen to follow [Astafiev10a].

The transfer matrix that accounts for the phase accumulated by radiation travelling between the two qubits is given by

$$T_\phi = \begin{bmatrix} e^{i2\pi\frac{\omega}{\omega_d}} & 0 \\ 0 & e^{-i2\pi\frac{\omega}{\omega_d}} \end{bmatrix}. \tag{4.3}$$

As an example, the transfer matrix for a system of three equidistant qubits in a transmission line is now simply given by the product of the transfer matrices of the subsystems

$$T_{total} = T_{qA} T_\phi T_{qB} T_\phi T_{qC}. \tag{4.4}$$

The total transfer matrix is then a function of all parameters determining the qubit reflection and transmission (see equation (3.26)), the distance between the qubits and the frequency of radiation sent into the system. The transmission and reflection coefficients of the total system can be extracted from the total transfer matrix according to equation (4.2).

There are two potential issues with these calculations. The first is that dephasing of the photon is not taken into account. However, photon dephasing is not expected to be important in our experiments. The second issue is more problematic; when using this transfer matrix approach, the output fields which give information about the reflectance and transmittance of the total system, are functions of the input fields when all parameters that go into the system are known. However, these parameters include the reflection and transmission coefficients of qubit A and B, which depend on the local fields at qubit A and B. These local fields are not accessible from the transfer matrix of the total system. For now we will assume that the drive powers at qubits A and B are equal to the input power, and see how well such a model agrees to experiment. Later, in section 4.2.4 we will relinquish the convenience of the transfer matrix approach and calculate the fields at qubits A and B directly, taking into account multiple reflection and transmission events.

In Fig. 4.7 we show the result of using transfer matrices to calculate the reflectance and transmittance of a two-qubit system. These figures were obtained using the same parameters as their experimental counterparts in Fig. 4.2: at 4.8 GHz, $\Gamma_1/2\pi = 13$ MHz, $\gamma_\varphi/2\pi = 2$ MHz, and the drive power at the qubit is -131 dBm. At 6.4 GHz, $\Gamma_1/2\pi = 26$ MHz, $\gamma_\varphi/2\pi = 0.5$ MHz, and the drive power at the qubit is -136 dBm. Comparing the simulation results to the experimental results we observe a good agreement, although there are some differences. One of the more obvious differences between the simulations and the experimental results is the shape of the crossing at 6.4 GHz, in the center of panel a in Fig. 4.7. The experimental crossing is darker (higher reflectance) and sharper than the transfer matrix theory predicts. For qubits tuned to 4.8 GHz, qualitative agreement is good.

The asymmetry in the peaks in reflectance observed in experiment (Fig. 4.2B and D) was thought to be due to a small detuning between the qubits. Introducing a small detuning in the transfer matrix simulations results in asymmetric peaks as shown in Fig. 4.8, confirming the hypothesis that the asymmetry is caused by a small detuning of the qubits.

4.2.3 Simulating reflectance and transmittance for multiple qubits

For all simulations presented below, the qubit parameters were set to be the same as in experiment. The qubits are separated by a distance equal to one wavelength at 6.4 GHz. The pure dephasing rate $\gamma_\varphi/2\pi$ was set to 2 MHz at 4.8 GHz and 0.5 MHz at 6.4 GHz, the qubits relax at rates of $\Gamma_1/2\pi = 12.9$ MHz at 4.8 GHz and 26 MHz at 6.4 GHz. The detuning marked on the horizontal axis for Figs. 4.9, 4.10, 4.11, 4.12, 4.13, 4.14 is the detuning between the center frequency in the figure, and the qubit tuned along the diagonal of the figure. All other qubits are detuned according

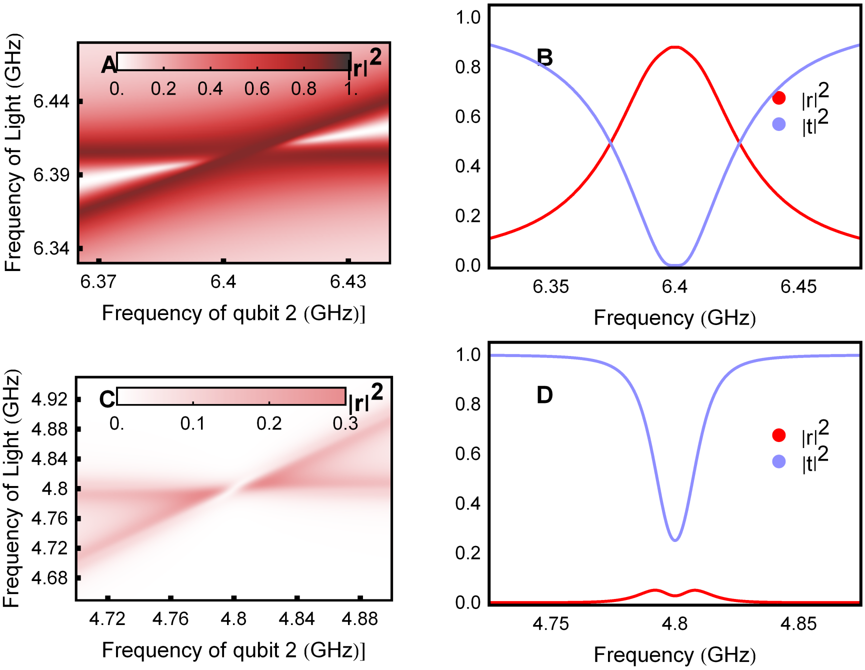

Figure 4.7: Simulation of a two-qubit system using transfer matrices. In (a), One qubit is kept at 6.4 GHz while another qubit is tuned into and out of resonance. The reflectance of the system is shown in color. In (b) the reflectance and transmittance are shown when the qubits are in resonance. (c) and (d) show the same for qubits at 4.8 GHz

to $a_i\delta\omega$, with $\delta\omega$ the detuning of the qubit along the diagonal, and a_i a arbitrarily chosen constant with which qubit i is detuned as a function of the x-axis. This way, all of the qubits are detuned simultaneously with different slopes, which was done in order to increase the visibility of interference effects when the qubits all get close to resonance. The first four of these figures (Figs. 4.9, 4.10, 4.11 and 4.12) show the reflectance and transmittance of three qubits in resonance at 4.8 and 6.4 GHz, first for similar drive powers as the experiments presented in Fig. 4.2, and then for lower powers, at which interference effects are more pronounced because the loss

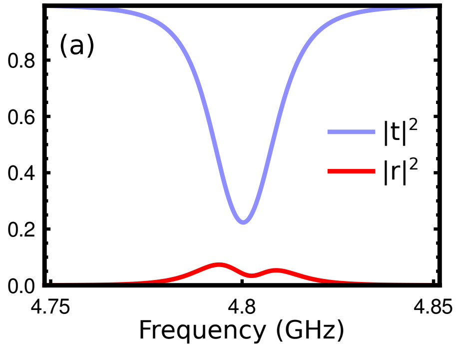

Figure 4.8: Simulation of a two-qubit system using transfer matrices. (a) Two qubits detuned by 1 MHz at 4.8 GHz. (b) Two qubits detuned by 2 MHz around 6.4 GHz.

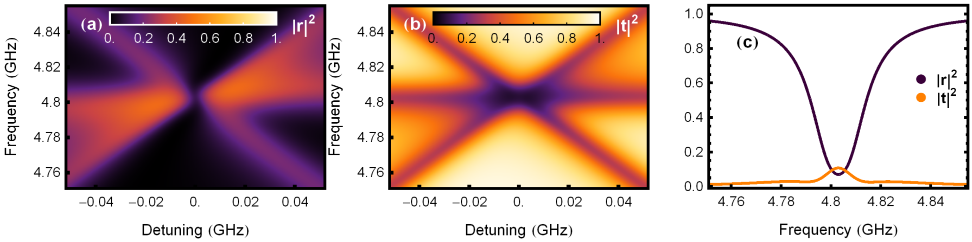

Figure 4.9: The reflectance (a) and transmittance (b) as calculated using transfer matrices for three qubits in resonance at 4.8 GHz, driven at a power of -129 dBm. (c) shows line cuts through the figures in (a) and (b) when all qubits are in resonance.

of radiation from the system when $\Omega \not\ll \Gamma_1$ leads to a decreased contrast. When the number of qubits is further increased (the easiness with which that can be done is one of the main appealing features of using transfer matrices), the interference patterns around resonance for qubits tuned to 4.8 GHz become increasingly more intricate (Fig. 4.13, 4.14).

The transmittance and reflectance at resonance can also be plotted as a function of the number of qubits. The results are shown in Figs. 4.15

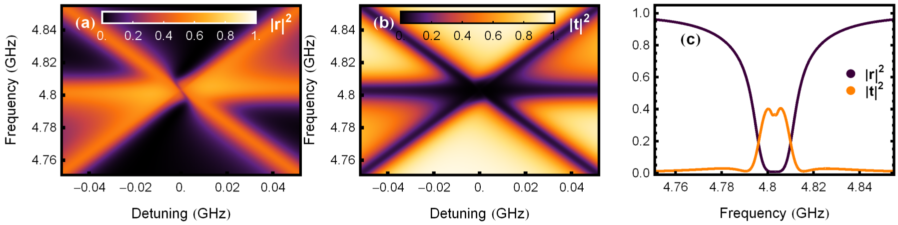

Figure 4.10: As in Fig. 4.9, but with a drive power of -140 dBm.

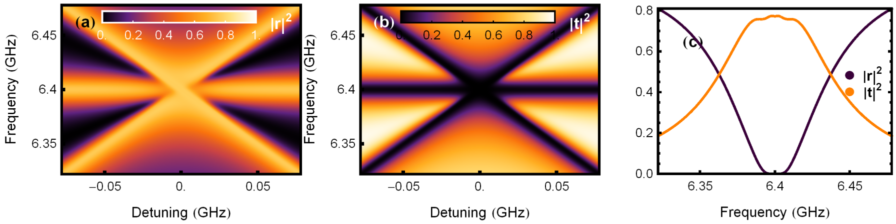

Figure 4.11: As in Fig. 4.9, but the qubits are tuned to be around resonance at 6.4 GHz, and the drive power is -134 dBm.

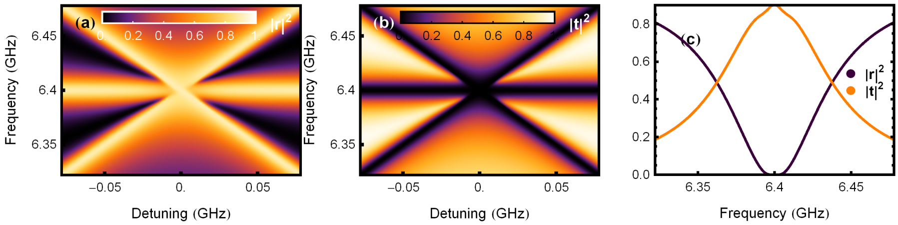

Figure 4.12: As in Fig. 4.11, but applying a drive power of -145 dBm.

and 4.16 for qubits in resonance at 4.8 and 6.4 GHz, respectively. The drive power in these simulations was kept low to keep the interference effects more visible – these effects are most apparent at 4.8 GHz, where the reflectance is very low at higher drive powers. In Fig. 4.15, we observe that whereas

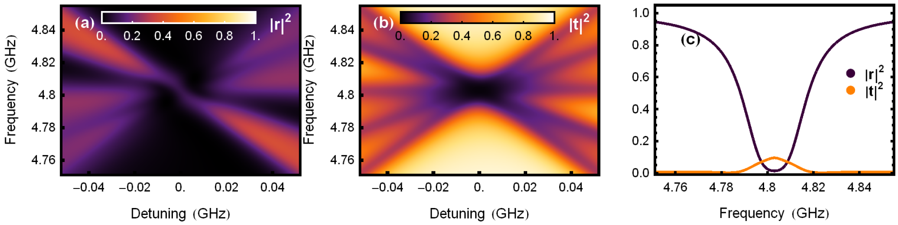

Figure 4.13: Five qubits moving in and out of resonance at 4.8 GHz at a drive power of -129 dBm.

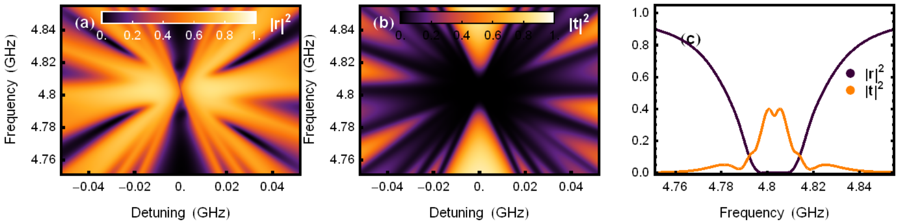

Figure 4.14: Eleven qubits moving in and out of resonance around 4.8 GHz at a drive power of -140 dBm. As the number of qubits is increased, the interference pattern becomes increasingly intricate.

the transmittance mainly shows a slow broadening in its dip with the number of qubits, the reflectance spectrum shows more and more side peaks in elastically scattered radiation. The maximum amplitude of the center reflectance peak, however, does not change with the number of qubits, indicating that for multiple qubits the maximum reflectance is still set by $\eta\Gamma_1/2\Gamma_2$, as for a single qubit. For qubits tuned to 6.4 GHz (Fig. 4.16), the main point of interest is the width of the qubit spectrum, which seems to go up linearly with the number of qubits (this was not quantified explicitly, as the width of a peak is ill-defined for strange peak shapes as in 4.16), unlike the situation at 4.8 GHz where the width of the spectra increases much more slowly.

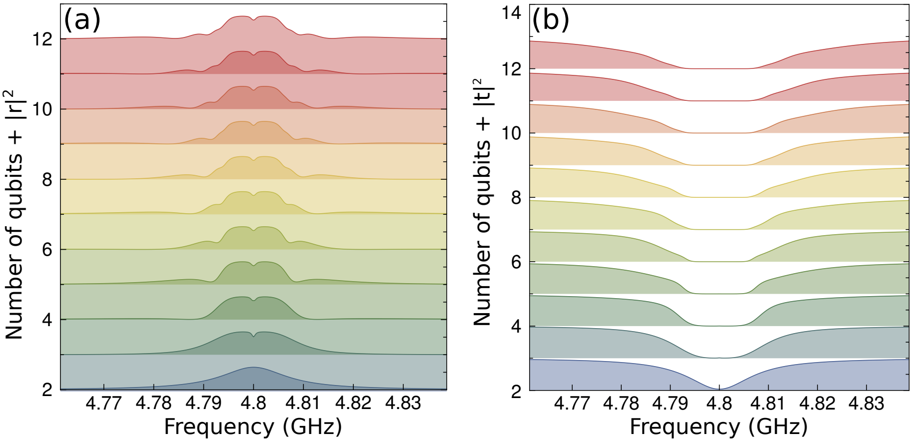

Figure 4.15: The reflectance (a) and transmittance (b) for multiple qubits in resonance at 4.8 GHz. Here, the parameters were chosen to be similar to experiment and to other simulations in this chapter, but at a lower drive power. The drive power is -150 dBm at the qubits, and the pure dephasing rate is set to $\gamma_\varphi/2\pi = 1.5$ MHz.

4.2.4 Simulations for unequal powers at the qubits

Whereas the transfer matrix method is useful in that it is computationally efficient, easily extendible to arbitrary numbers of qubits and replicates the experimentally observed effects to a good degree, it does not capture all the physics involved correctly. Most notably, the drive power used to compute the reflection and transmission coefficients of the qubits is assumed to be the same as the input power. In reality, due to the nonzero reflection coefficient of qubit A, qubit B will see less power than the input power. Besides, due to multiple reflection events between qubits A and B, the field at qubit A is generally not of the same magnitude as input field. Moreover, the difference in field magnitude at both qubits depends strongly on the detuning between drive tone and qubit transition frequency. For a drive tone slightly detuned from qubit A, the transmittance of qubit A will be much higher, and therefore the field magnitude at qubit B will be higher than for a resonant drive tone.

These effects can be calculated numerically. To do so, we define a quantity

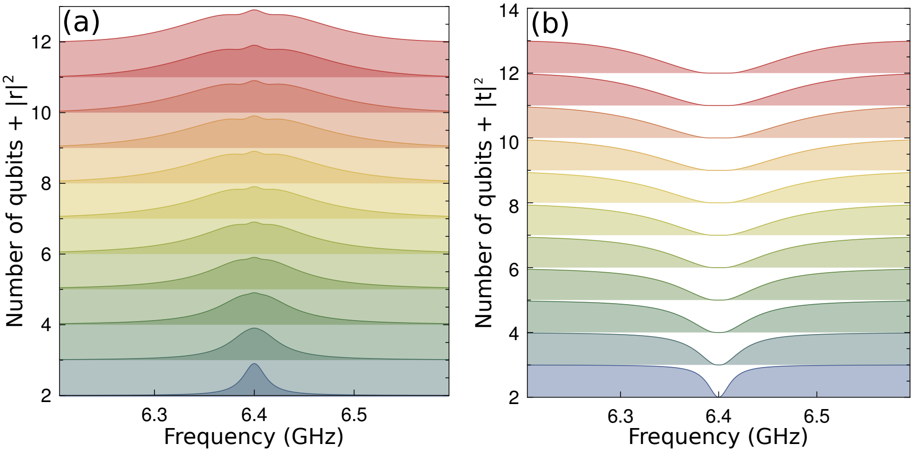

Figure 4.16: The reflectance (a) and transmittance (b) for multiple qubits in resonance at 6.4 GHz. Here, the parameters were chosen to be similar to experiments, but at a lower drive power. The drive power is -150 dBm, and the pure dephasing rate is set to $\gamma_\varphi/2\pi = 0.5$ MHz.

of time δt which is equal to the time needed by radiation to travel from qubit A to qubit B: $\delta t \equiv d/c$, with d the physical distance between the qubits and c the speed of light in the transmission line between them. We switch on the microwave drive such that at $t = \delta t$, the drive arrives from the left at qubit (which we call qubit A), but not yet at qubit B (see Fig. 4.17). To calculate the build-up of the field between the qubits, we make the unphysical assumption that the qubit dynamics are instantaneous. At time $t = 2\delta t$, the transmitted part of the input light arrives from the left at qubit B, while the reflected part of the radiation is absorbed by a detector. At each time step, power is applied from the left to qubit A, as we are investigating the steady state properties of the two-qubit system under a continuous drive from the left. As time progresses, the field builds up between the two qubits. In the schematic example in Fig. 4.17, the total field at qubit A builds up over time, changing the transmission and reflection coefficients of qubit A, which again change the local fields, etc. For the drive powers and qubit parameters as in experiment (Fig. 4.2), the system

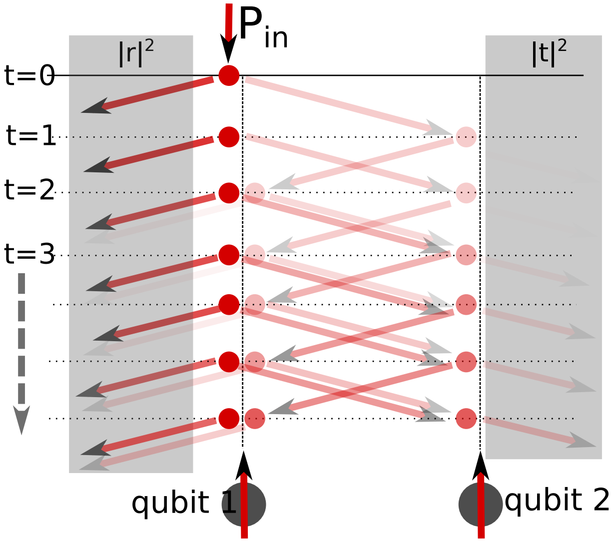

Figure 4.17: The field between the two qubits builds up, altering the reflection and transmission coefficients of both qubits. The circles at the left and right sides of the qubit location denote the field magnitude coming from the left and right sides of the qubits.

reaches a steady state in a few tens of turns, as shown in Fig. 4.18. If the drive power is decreased, the system needs longer to reach a steady state, and vice versa. While the schematic in Fig. 4.17 does not show the effect of phase, the simulations keep track of the phase of the fields as well as their magnitudes. We can now use this model to simulate the experiment shown in Fig. 4.2 again. The results are shown in Fig. 4.19. The agreement with experiment is better than for the transfer matrix model. For qubits close to resonance at 6.4 GHz, we would like to point out two phenomena which are better predicted by this model: the first is the difference in the two-qubit peak height in reflectance compared to single-qubit peaks. The second is the white triangles in Figs. 4.2a and 4.19b caused by interference for nearly-resonant qubits – both the experiment and the simulations presented in this section show sharp white triangles approaching the center of the figure, whereas in the transfer matrix based simulations (Fig. 4.7a) these triangles vanish further away from resonance. This model shows a

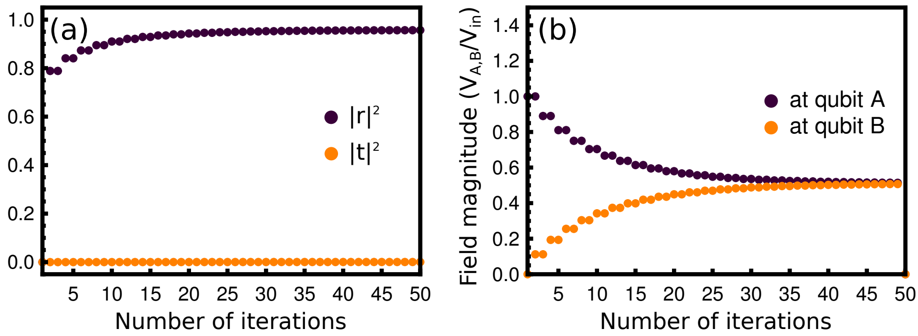

Figure 4.18: Two qubits in resonance at 6.4 GHz, at a drive power of −130 dBm. (a) the reflectance and transmittance change only slightly as the number of iterations go up. (b) We define normalized field magnitudes as $V_{A,B}/V_{in}$ for qubits A and B. These field magnitudes change strongly as a function of the number of iterations. At a drive power of −136 dBm, the fields have converged to a steady state value after some 40 iterations. At 4.8 GHz, the fields converge much quicker, and qubit A sees a larger field than the input field and qubit B (not shown).

high degree of agreement with the experimentally observed elastic scattering properties of a two-qubit system. As this model was constructed while finalizing this thesis, and as it is computationally much less efficient than the transfer matrix model, we have not redone all simulations which were carried out with the transfer matrix model using the model presented in this section.

The most important conclusion to be drawn from the agreement between experiment and both models presented in this section is however of a different nature. As these semi-classical models – in which qubit interactions are of a purely interferometric nature – agree well with the experimentally observed behaviour, we are led to conclude that no quantum-mechanical interactions are necessary to predict the elastically scattered radiation. It is especially surprising that the interference models correctly predict that a two-qubit spectrum is twice as broad as a single-qubit spectrum at 6.4 GHz, while at 4.8 GHz there is no appreciable difference in line width. This ef-

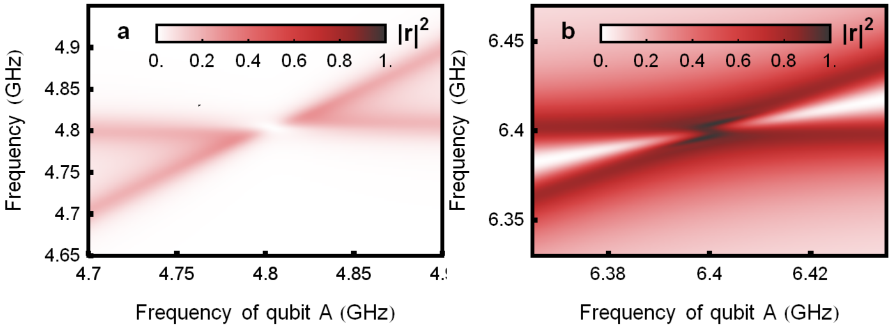

Figure 4.19: (a) A simulation of two qubits being tuned into and out of resonance at 4.8 GHz. Qubit parameters were $\Gamma_1/2\pi = 14$ MHz, $\gamma_\varphi/2\pi = 2$ MHz, drive power at the qubits was -130.5 dBm, and $\eta = 0.92$. (b) At 6.4 GHz, the parameters were chosen to be $\Gamma_1/2\pi = 26$ MHz, $\gamma_\varphi/2\pi = 0.5$ MHz, drive power at the qubits was -136 dBm, and $\eta = 1$. These parameters are in accordance with experimental parameters for the experimental results shown in Fig. 4.2.

fect, as we will see in the next chapter (chapter 5) is also predicted by a full quantum mechanical model, where we will call it ‘correlated decay’. That this effect is predicted here already means that it is not quantum mechanical, but interferometric in nature. To experimentally observe the quantum mechanical interaction effects we will need to include inelastically scattered as well as elastically scattered radiation in the scope of both our measurements and theory, which is the topic of the next chapter.

5 Inelastic scattering properties of a system of distant artificial atoms

In the previous chapter, where we considered elastically scattered radiation from two qubits, we could make do with a semi-classical model, where the qubits could be considered as mirrors (albeit mirrors that can be saturated) and where all interaction effects were caused by interference. In this chapter, we will however look at inelastically scattered radiation, which by its very nature is quantum mechanical. To explain what we observe, we therefore need a quantum-mechanical framework. Such a framework was constructed (based on earlier work by Lehmberg [Lehmberg70]) by our collaborators, and published in [Lalumière13]. The first section of this chapter will consist of explaining this framework, where we will omit only the most technical of details. In the second part of this chapter, results will be shown for resonance fluorescence measurements on a system of two qubits, and they will be compared to and explained by the aforementioned theory.

5.1 A master equation for two distant artificial atoms

In the following, we will theoretically investigate a system of M N-level systems (Fig. 5.1) in an open one-dimensional space. An effective master equation for such a system can be derived, and en route we will find elegant expressions for the interaction effects which manifest between distant artificial atoms. After obtaining this general master equation, which we will further on use for numerical calculations on two multilevel transmon systems, input-output boundary conditions will be used to relate the measurable quantities – the outgoing fields – to the qubit dynamics. Intuitive insights can be gained by looking at the more simple system of two two-level systems in a transmission line, which we will do specifically for inter-qubit distances of $d = \lambda_r$ and $d = 3\lambda_r/4$.

This theoretical framework was constructed by Lalumière and coworkers in

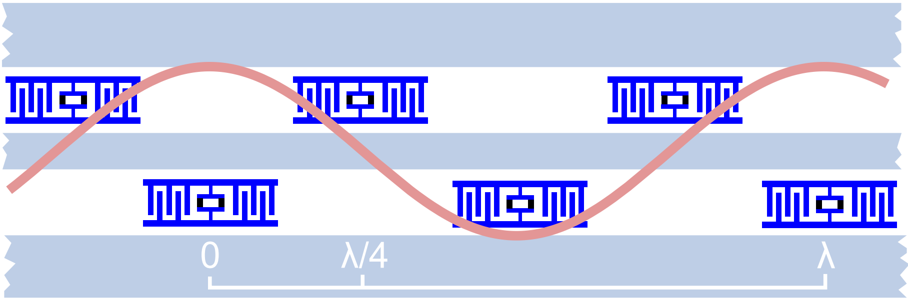

Figure 5.1: Schematic of several qubits (not to scale) in an open transmission line, separated by $\lambda_r/4$.

collaboration with our experimental work. As such, this section will rely heavily on their publication [Lalumière13], which follows the approach of Lehmberg [Lehmberg70] but adapts it for a one-dimensional space. We will therefore adopt the symbols used in [Lalumière13] in most cases. Except for the published theory, we offer some intuitive explanations about the effects of non-radiative decay and different qubit lifetimes which were not covered elsewhere.

It should be noted here that [Lalumière13] does not present the only theory for waveguide QED. Most notably, much theoretical work was done by Zheng, Fang and Baranger, who show how to engineer highly correlated photon-photon pairs and effective repulsive or attractive photon-photon interactions [Zheng10, Zheng12c], how to distribute quantum keys for secure quantum communication using waveguide QED [Zheng12b], how to do quantum computation in waveguide QED [Zheng12d] and how the Markovian approximation breaks down [Zheng13] for a system sized beyond a few wavelengths. One of their latest papers [Fang13] predicts what the second-order correlation function looks like for three artificial atoms as a function of their separation: oscillations between bunching and anti-bunching for qubits half a wavelength apart, and a strong bunching followed by a long anti-bunching time for qubits one quarter wavelength apart. With our setup, we should be able to experimentally verify these predictions.

5.1.1 The Hamiltonian for qubits in a transmission line

For a system of multiple qubits in an open transmission line (Fig. 5.1) the Hamiltonian can be divided into three parts. The first part is the energy contained in the fields in the transmission line [Shen05b]

$$\hat{H}_{\mathrm{F}} = \int_0^\infty d\omega\hbar\omega \left[\hat{a}_{\mathrm{R}}^\dagger(\omega)\hat{a}_{\mathrm{R}}(\omega) + \hat{a}_{\mathrm{L}}^\dagger(\omega)\hat{a}_{\mathrm{L}}(\omega)\right], \tag{5.1}$$

with $\hat{a}_{\mathrm{R/L}}^\dagger$ the creation operator for a right/left moving photon, and $\hat{a}$ the corresponding annihilation operator. The creation and annihilation operators obey the commutator $[\hat{a}_{\mathrm{R/L}}(\omega), \hat{a}_{\mathrm{R/L}}^\dagger(\omega')] = \delta(\omega - \omega')$. The integral goes from 0 to ∞ to take into account all modes in the continuum. A second part of the Hamiltonian comprises the qubits:

$$\hat{H}_{\mathrm{A}} = \sum_{j=0}^{N-1}\sum_{m=0}^{M-1} E_{mj}|m_j\rangle\langle m_j|, \tag{5.2}$$

with E_{mj} the energy of state m of qubit j. The third part of the Hamiltonian describes the interaction between the propagating fields $\hat{\Xi}$ and the qubits

$$\hat{H}_{\mathrm{I}} = \sum_{j=0}^{N-1}\sum_{m=0}^{M-1} \hbar g_j\sqrt{m+1}\left(\hat{\Xi}_j + \hat{\Xi}_j^\dagger\right)\hat{\sigma}_x^{mj}, \tag{5.3}$$

where each term in the sum describes the coupling for qubit j in the m^{th} state. g_j is the dimensionless coupling strength between atom j and the transmission line, given by

$$g_j = \left(\sqrt{\frac{e^2 c}{2\hbar\pi v c_{gj}^2}}\right)\left(\frac{E_{Jj}}{8E_{Cj}}\right)^{(1/4)}, \tag{5.4}$$

which is similar to the expression for a transmon qubit in a cavity as in [Koch07], but with a different pre-factor. Similar to there, the transition dipole moment of a qubit is given by $(2e/\sqrt{2})|\langle i|\hat{n}|i+1\rangle|$, but the pre-factor describing the voltage in the vacuum coupling to the qubit is now described as $(1/2)\sqrt{c/(\hbar\pi v c_{gj}^2)}$, while it is βV_{rms} in circuit QED, where the qubit mainly couples to a single mode of the electromagnetic field. In this expression, c_{gj} is the coupling capacitance per unit length between qubit j

and the line, and c is the capacitance per unit length of the transmission line. v denotes the speed of light in the transmission line. The field at position x_j of qubit j is proportional to

$$\hat{\Xi}_j = -i \int_0^\infty d\omega \sqrt{\omega} \left[\hat{a}_{\mathrm{L}}(\omega) e^{-i\omega x_j/v} + \hat{a}_{\mathrm{R}}(\omega) e^{i\omega x_j/v} \right], \tag{5.5}$$

As seen in (5.3), the field couples to the qubit via $\hat{\sigma}_x^{mj}$, the combination of the lowering and raising operator for a multilevel system

$$\hat{\sigma}_x^{mj} = \hat{\sigma}_-^{mj} + \hat{\sigma}_+^{mj}, \tag{5.6}$$

and

$$\hat{\sigma}_-^{mj} = |m_j\rangle\langle(m+1)_j| = \left(\hat{\sigma}_+^{mj}\right)^\dagger, \tag{5.7}$$

which lowers the j^{th} atom from the $(m+1)^{\mathrm{th}}$ to the m^{th} excited state. Only the transitions between neighbouring excited states are allowed, in accordance with the properties of a transmon qubit [Koch07]. The total Hamiltonian is then given by

$$\hat{H}_{\mathrm{tot}} = \hat{H}_{\mathrm{F}} + \hat{H}_{\mathrm{A}} + \hat{H}_{\mathrm{I}}. \tag{5.8}$$

We omit the derivation of this Hamiltonian starting from a lumped-element model. The interested reader is referred to appendix A of [Lalumière13] and [Devoret97].

5.1.2 Deriving the master equation

The method used here for obtaining a master equation follows the work done for atoms in a three-dimensional free space by [Lehmberg70] more than 40 years ago. We start by finding an expression for the annihilation operators. In the Heisenberg picture, we have that

$$\frac{d\hat{a}_{\mathrm{R}}(\omega)}{dt} = \frac{i}{\hbar}[\hat{H}, \hat{a}_{\mathrm{R}}(\omega)] = -i\omega\hat{a}_{\mathrm{R}}(\omega) + \sum_{mj} g_j \sqrt{m+1}\sqrt{\omega} e^{-i\omega x_j/v} \hat{\sigma}_x^{mj}, \tag{5.9}$$

where the first term is due to $\hat{H}_{\mathrm{F}}$ and the second term due to $\hat{H}_{\mathrm{I}}$. We obtain an explicit time-dependent form of $\hat{a}_{\mathrm{R}}$ by assuming that a time $t = 0$ exists in the past at which no interactions between the atoms and the field had yet taken place. We then integrate from this time onwards:

$$\hat{a}_{\mathrm{R}}(\omega,t)=\hat{a}_{\mathrm{R}}(\omega,0)e^{-i\omega t}+\sum_{mj}g_j\sqrt{m+1}\sqrt{\omega}\int_0^t d\tau e^{-i\omega(t-\tau+t_j)}\hat{\sigma}_x^{mj}(\tau), \tag{5.10}$$

where $t_j=x_j/v$ – the time needed for radiation to reach qubit j. This can be substituted in the expression for $\hat{\Xi}$ (5.5) to obtain

$$\hat{\Xi}_j(t)=\hat{\Xi}_j^{\mathrm{in}}(t)-i\sum_{nk}\sum_{\sigma=\pm1}g_k\sqrt{n+1}\int_0^t d\tau\hat{I}_{nk}(t,\tau,\sigma t_{kj}), \tag{5.11}$$

where t_{kj} is the time light needs to travel from qubit k to qubit j, and where we have defined

$$\hat{\Xi}_j^{\mathrm{in}}(t)=-i\int_0^\infty d\omega\sqrt{\omega}\left[\hat{a}_{\mathrm{L}}(\omega,0)e^{-i\omega(t+t_j)}+\hat{a}_{\mathrm{R}}(\omega,0)e^{-i\omega(t-t_j)}\right]. \tag{5.12}$$

This is a term describing the field at time t due to the input field at time $t=0$ without taking into account contributions to the field due to the qubits. Those alterations are described by the second term in (5.11), where

$$\hat{I}_{nk}(t,\tau,t_{kj})\equiv\int_0^\infty d\omega\omega e^{i\omega(\tau-t-t_{kj})}\hat{\sigma}_x^{nk}(\tau), \tag{5.13}$$

which connects the field dynamics at the position of qubit j to the qubit dynamics of qubit k. This expression is problematic, as the integration over $\hat{\sigma}_x^{nk}(\tau)$ implies that we are required to know the entire history of the qubit. To be able to proceed further, we need a Markov approximation.

The Markov approximation

The trouble with (5.13) is its dependence on τ. The integration over τ from a time before interactions to time t requires knowledge of the state of qubit k during all that time. We can use the evolution operator to write (5.13) out as

$$\begin{aligned}\hat{I}_{nk}(t,\tau,t_{kj})&=\int_0^\infty d\omega\omega e^{i\omega(\tau-t-t_{kj})}\hat{\sigma}_x^{nk}(\tau)\\&=\int_0^\infty d\omega\omega e^{-i\omega(\tau-t-t_{kj})}\left[e^{i\hat{H}_T(\tau-t)/\hbar}\hat{\sigma}_-^{nk}(t)e^{-i\hat{H}_T(\tau-t)/\hbar}+\mathrm{H.c.}\right],\end{aligned} \tag{5.14}$$

in which t is the upper integration limit of τ. Contributions to this integral due to low frequencies can be neglected because the integrand grows with ω. On the other hand, because of the exponential in the first term of (5.14), high frequency components oscillate quickly and average to zero. An exception occurs when $\tau = t + t_{kj}$, where the integrand does not oscillate. In other words, the field at the position of qubit j is mainly affected by the state of qubit k at a time earlier by t_{kj}, the time needed for information about the state of qubit k to travel to qubit j. Furthermore, we will neglect the interaction term $\hat{H}_{\mathrm{I}}$ in the time evolution operators in (5.14) so that the state of qubit k at time $\tau = t - t_{kj}$ can be inferred from the state at time t, corrected by the Larmor precession over t_{kj}. Neglecting the interaction Hamiltonian is necessary because otherwise the state of qubit k at time $\tau = t - t_{kj}$ would depend on the state of qubit j at time $\tau = t - 2t_{kj}$ which would again depend on the state of qubit k at time $\tau = t - 3t_{kj}$, ad infinitum. We omit the calculation showing that the error due to neglecting $\hat{H}_{\mathrm{I}}$ is small, and refer the interested reader to [Lalumière13]. Combining these two approximations, we can rewrite $\hat{\sigma}_{-}^{nk}$ in equation (5.14) as

$$\hat{\sigma}_{-}^{nk}(\tau) \approx \hat{\sigma}_{-}^{nk}(t)e^{-i\omega_{nk}(\tau - t)}, \tag{5.15}$$

where ω_{nk} is the Larmor precession frequency of qubit k for level n. In other words, the only part of the history of qubit k we take into account when calculating its effect on qubit j is its Larmor precession. This is equivalent to a Markov approximation. The validity of this approximation when increasing the distance between the qubits was studied in [Zheng12a], and was found to break down when the qubits are separated by more than a few wavelengths – a situation that will not concern us in this work.

Long-time approximation

In order to proceed with evaluating the expression for $\hat{\Xi}_j(t)$ (5.11), we use that

$$\int_0^\infty dx e^{-ikx} = \pi\delta\left(k\right) - i\mathrm{P}\left(\frac{1}{k}\right), \tag{5.16}$$

with P the Cauchy principal value. To use this identity, we need the time integral in (5.11) to go to infinity instead of t (hence the name long-time approximation). However, as soon as $\omega_{nk}t \gg 1$, the integration already takes place over many oscillations, and the error in letting $\omega_{nk}t$ go to ∞ is very small. For a system such as ours, using superconducting qubits, it means that we need that $t \gg .02$ ns. Given the bandwidth of our measurement setup, it would be impossible to look at dynamics this fast even if we wanted to, and conversely for the dynamics we expect to be able to observe, this approximation ($\omega_{nk}t \gg 1$) is valid. Physically, this approximation should be seen as the qubits interacting instantaneously. As the phase shift acquired by radiation going from one qubit to another is still taken into account, the effect on qubit 2 by qubit 1 at time t is still caused by light emitted at time $t-t_{kj}$. However, there is a problem during transients: when a drive is switched on and reaches qubit 1 at time t, the effects of this drive will be felt by qubit 2 at time t as well, rather than at time $t+t_{kj}$. As such, the calculations using this approximation are only valid when looking at times longer than t_{kj} after switching on the drive. Applying the Markov and long-time approximation to (5.12), we have

$$\hat{\Xi}_j(t) = \hat{\Xi}_j^{\text{in}}(t) - \frac{1}{g_j}\sum_{nk}\left[\Omega_{kj}^{n+}\hat{\sigma}_+^{nk} + \left(\Omega_{kj}^{n-} + i\gamma_{kj}^n/2\right)\hat{\sigma}_-^{nk}\right], \tag{5.17}$$

with the definitions

$$\Omega_{kj}^{n\pm} \equiv 2g_k g_j\sqrt{n+1}\,\mathrm{P}\int_0^\infty \frac{\omega\cos\left(\omega t_{kj}\right)}{\omega \pm \omega_{nk}}d\omega, \tag{5.18}$$

and

$$\gamma_{kj}^n \equiv 4\pi g_k g_j \omega_{nk}\sqrt{n+1}\cos\left(\omega_{nk}t_{kj}\right). \tag{5.19}$$

With the goal of obtaining a master equation, we define a hypothetical operator $\hat{Q}$ that acts only on the qubits. Going back to the definition of $\hat{\Xi}$ (5.5) which contains no atomic operators, we see that $[\hat{Q}(t), \hat{\Xi}(t)] = 0$. We then have for $\hat{Q}$

$$\frac{d\hat{Q}}{dt} = \frac{i}{\hbar}\left([\hat{H}_{\mathrm{A}}, \hat{Q}] + [\hat{H}_{\mathrm{I}}, \hat{Q}] + [\hat{H}_{\mathrm{F}}, \hat{Q}]\right), \tag{5.20}$$

where the last term must be zero as the operator acts only on the qubits. Substituting (5.3) and (5.17) into (5.20) we get

$$\begin{aligned}\frac{d\hat{Q}}{dt} =& \frac{i}{\hbar}\left[\left[\hat{H}_A, \hat{Q}\right] + \left[\hbar\sum_{mj}\sqrt{m+1}g_j\left(\hat{\Xi}_j^{\text{in}} + \text{H.c.}\right)\sigma_x^{mj}, \hat{Q}\right]\right] \\ &+ \left[\sum_{mj}\sum_{nk}\sqrt{m+1}\left(\Omega_{kj}^{n+}\hat{\sigma}_+^{nk} + \left(\Omega_{kj}^{n-} + i\gamma_{kj}^{n}/2\right)\hat{\sigma}_-^{nk} + \text{H.c.}\right)\hat{\sigma}_x^{mj}, \hat{Q}\right],\end{aligned} \tag{5.21}$$

which after writing out and reshuffling the order of the various operators can be rewritten as

$$\begin{aligned}\frac{d\hat{Q}}{dt} =& \frac{i}{\hbar}\left[\hat{H}_A + \hbar\sum_{mj}\sqrt{m+1}g_j\left(\hat{\Xi}_j^{\text{in}} + \text{H.c.}\right)\hat{\sigma}_x^{mj}, \hat{Q}\right] \\ &+ \sum_{mj}\sum_{nk}\sqrt{m+1}\Big[-i\Omega_{kj}^{n+}\left(\hat{\sigma}_x^{mj}\hat{Q}\hat{\sigma}_+^{nk} - \hat{Q}\hat{\sigma}_x^{mj}\hat{\sigma}_+^{nk} - \text{H.c.}\right) \\ &\qquad - i\Omega_{kj}^{n-}\left(\hat{\sigma}_x^{mj}\hat{Q}\hat{\sigma}_-^{nk} - \hat{Q}\hat{\sigma}_x^{mj}\hat{\sigma}_-^{nk} - \text{H.c.}\right) \\ &\qquad + \frac{\gamma_{kj}^{n}}{2}\left(\hat{\sigma}_x^{mj}\hat{Q}\hat{\sigma}_-^{nk} - \hat{Q}\hat{\sigma}_x^{mj}\hat{\sigma}_-^{nk} + \text{H.c.}\right)\Big].\end{aligned} \tag{5.22}$$

We want to obtain a reduced density matrix of the atoms only. However, the above expression still contains parts that are photonic rather than atomic in nature, such as the term containing $\hat{\Xi}_j^{\text{in}}$. We will need to evaluate these terms in more detail.

5.1.3 The drive term

Here we try to find an expression for an effective drive term that does not include the annihilation and creation operators. To that end, we define a drive superoperator $\mathcal{D}$ that, when applied on the density matrix $\hat{\rho}$, results in the drive term of (5.21):

$$\begin{aligned}\mathrm{Tr}_{\mathrm{A}}\left[\hat{Q}\mathcal{D}[\hat{\rho}]\right] =& i\sum_{mj} g_j\sqrt{m+1}\mathrm{Tr}_A\left[\mathrm{Tr}_P\left[\left(\left[\hat{\sigma}_x^{mj},\hat{Q}\right]\hat{\Xi}_j^{\mathrm{in}} - \mathrm{H.c.}\right)\hat{\rho}_T\right]\right] \\ =& \left\langle i\sum_{mj} g_j\sqrt{m+1}\left(\left[\hat{\sigma}_x^{mj},\hat{Q}\right]\hat{\Xi}_j^{\mathrm{in}} - \mathrm{H.c.}\right)\right\rangle, \end{aligned} \tag{5.23}$$

with $\mathrm{Tr}_{\mathrm{P(A)}}$ the partial trace over the photonic (atomic) part of the system. Since all operators here are evaluated at time t, causality dictates there can be no correlations between the input field operators $\hat{\Xi}_j^{\mathrm{in}}$ and the atomic operators. Hence,

$$\begin{aligned}\mathrm{Tr}_A\left[\hat{Q}\mathcal{D}[\hat{\rho}]\right] =& i\sum_{mj} g_j\sqrt{m+1}\left(\left\langle\left[\hat{\sigma}_x^{mj},\hat{Q}\right]\right\rangle\left\langle\hat{\Xi}_j^{\mathrm{in}}\right\rangle - \mathrm{H.c.}\right) \\ =& i\sum_{mj} g_j\sqrt{m+1}\times\mathrm{Tr}_A\left[\left[\left(\left\langle\hat{\Xi}_j^{\mathrm{in}}\right\rangle + \mathrm{c.c.}\right)\hat{\sigma}_x^{mj},\hat{Q}\right]\hat{\rho}\right]. \end{aligned} \tag{5.24}$$

We now define an expression for the drive strength $d_{mj}(t)$ as

$$d_{mj}(t) = g_j\sqrt{m+1}\left(\left\langle\hat{\Xi}_j^{\mathrm{in}}(t)\right\rangle + \left\langle\hat{\Xi}_j^{\mathrm{in}}(t)\right\rangle^*\right). \tag{5.25}$$

Driving from both sides with a coherent state $|\{\alpha\}\rangle$ [Loudon00] described by

$$\hat{a}_{\mathrm{L(R)}}(\omega,0)|\{\alpha\}\rangle = \sqrt{\frac{P_{\mathrm{L(R)}}}{\hbar\omega_d}}e^{-i\omega_d\theta_{\mathrm{L(R)}}}\delta(\omega-\omega_d)|\{\alpha\}\rangle, \tag{5.26}$$

with $P_{\mathrm{L(R)}}$ and $\theta_{\mathrm{L(R)}}$ the power and phase of the drive to the left (right). The expectation values of the input fields can be calculated to be

$$\begin{aligned}\left\langle\hat{\Xi}_j^{\mathrm{in}}(t)\right\rangle =& \langle\{\alpha\}|\hat{\Xi}_j^{\mathrm{in}}|\{\alpha\}\rangle \\ =& -i\left[e^{-i\omega_d(t+t_j+\theta_{\mathrm{L}})}\sqrt{2\pi P_{\mathrm{L}}/\hbar} + e^{-i\omega_d(t-t_j+\theta_{\mathrm{R}})}\sqrt{2\pi P_{\mathrm{R}}/\hbar}\right], \end{aligned} \tag{5.27}$$

such that the drive strength can be written as

$$\begin{aligned}d_{mj}(t) = -2\sqrt{\frac{\gamma_{mj,mj}}{2}}\Bigg(&\sqrt{\frac{P_{\mathrm{L}}}{\hbar\omega_{mj}}}\sin\left[\omega_d(t+t_j+\theta_{\mathrm{L}})\right] \\ &+\sqrt{\frac{P_{\mathrm{R}}}{\hbar\omega_{mj}}}\sin\left[\omega_d(t-t_j+\theta_{\mathrm{R}})\right]\Bigg). \end{aligned} \tag{5.28}$$

We can now rewrite the second term of (5.22) in a much simpler form, which no longer contains any operators acting on the field.

$$
\begin{aligned}
\frac{d\hat{Q}}{dt} =& \frac{i}{\hbar}\left[\hat{H}_A + \hbar\sum_{mj} d_{mj}(t)\hat{\sigma}_x^{mj}, \hat{Q}\right] \\
&+ \sum_{mj}\sum_{nk}\sqrt{m+1}\Bigg[-i\Omega_{kj}^{n+}\left(\hat{\sigma}_x^{mj}\hat{Q}\hat{\sigma}_+^{nk} - \hat{Q}\hat{\sigma}_x^{mj}\hat{\sigma}_+^{nk} - \text{H.c.}\right) \\
&\qquad - i\Omega_{kj}^{n-}\left(\hat{\sigma}_x^{mj}\hat{Q}\hat{\sigma}_-^{nk} - \hat{Q}\hat{\sigma}_x^{mj}\hat{\sigma}_-^{nk} - \text{H.c.}\right) \\
&\qquad + \frac{\gamma_{kj}^n}{2}\left(\hat{\sigma}_x^{mj}\hat{Q}\hat{\sigma}_-^{nk} - \hat{Q}\hat{\sigma}_x^{mj}\hat{\sigma}_-^{nk} + \text{H.c.}\right)\Bigg].
\end{aligned}
\tag{5.29}
$$

5.1.4 The Ω coefficients

The other terms in need of attention are the various Ω coefficients. From the way they enter equation (5.29), these terms seem to represent other mechanisms for changing the qubit population than the drive, such as decay. For the reader seeking the shortest path to the effective master equation for the qubits, we can reveal already that some of these terms will be absorbed into the qubit Hamiltonian while most terms will be omitted later either because they are small or because of the rotating wave approximation. For those who wish to see this proven, we start by recalling the expression for $\Omega_{nk}^{n\pm}$

$$
\Omega_{kj}^{n\pm} \equiv 2g_k g_j\sqrt{n+1}\,\mathrm{P}\int_0^\infty \frac{\omega\cos\left[\omega t_{kj}\right]}{\omega \pm \omega_{nk}}d\omega. \tag{5.30}
$$

In order to solve this integral, we first perform a variable transformation: $x = (\omega \pm \omega_{nk})/\omega_{nk}$ and $y = x \mp 1$. We then have

$$
\begin{aligned}
\Omega_{kj}^{n\pm} =& 2g_k g_j \omega_{nk}\sqrt{n+1}\left(\int_0^\infty dy\cos\left(\omega_{nk}t_{kj}y\right)\right. \\
&\left.\mp \mathrm{P}\int_{\pm 1}^\infty dx\frac{\cos\left(\omega_{nk}t_{kj}(x\mp 1)\right)}{x}\right).
\end{aligned}
\tag{5.31}
$$

In the first term, the integration limit at infinity presents a problem. However, as we will be concerned with real transmon qubits rather than ideal point-like atoms, we have reasons not to concern ourselves with infinitely high frequencies. The most important of these reasons is that when frequencies are very high, the corresponding wavelengths of modes at these frequencies will be smaller than the system size of the qubit. When wavelengths get shorter than the qubit, the average voltage on the capacitor plate of the qubit will go to zero, and therefore the qubit will not couple to modes at these frequencies. Moreover, the qubit being a real physical system, there will be limits to its dynamics. Frequencies faster than the limiting timescales of the qubit dynamics will not affect the qubit, and can therefore be ignored. We can mathematically impose a frequency limit by adding a factor that makes the expression converge at high frequencies

$$\lim_{\eta\to 0^+} \int_0^\infty dy \cos\left(\omega_{nk} t_{kj} y\right) e^{-\eta y} = \lim_{\eta\to 0^+} \frac{\eta}{\left(\omega_{nk} t_{kj}\right)^2 + \eta^2} = 0. \tag{5.32}$$

For the second term in (5.31), on the other hand, we have

$$\begin{aligned} &\mathrm{P}\int_{\pm 1}^\infty dx \frac{\cos\left(\omega_{nk} t_{kj} (x \mp 1)\right)}{x} \\ &= \cos\left(\omega_{nk} t_{kj}\right) \mathrm{P}\int_{\pm 1}^\infty dx \frac{\cos\left(\omega_{nk} t_{kj} x\right)}{x} \\ &\quad \pm \sin\left(\omega_{nk} t_{kj}\right) \mathrm{P}\int_{\pm 1}^\infty dx \frac{\sin\left(\omega_{nk} t_{kj} x\right)}{x} \\ &= -\cos\left(\omega_{nk} t_{kj}\right) \mathrm{Ci}\left(\left|\omega_{nk} t_{kj}\right|\right) \\ &\quad + \frac{\sin\left(\omega_{nk} t_{kj}\right)}{2} \Big(\pm\pi \mathrm{Sign}\left(\omega_{nk} t_{kj}\right) - 2\mathrm{Si}\left(\omega_{nk} t_{kj}\right)\Big), \end{aligned} \tag{5.33}$$

where $\mathrm{Ci}\,(x)$ and $\mathrm{Si}\,(x)$ are the cosine and sine integral functions defined as

$$\mathrm{Ci}\,(x) \equiv -\int_x^\infty dt \frac{\cos(t)}{t}, \qquad \mathrm{Si}\,(x) \equiv \int_0^x dt \frac{\sin(t)}{t}. \tag{5.34}$$

Substituting these in equation (5.31) results in

$$\Omega_{kj}^{n\pm} = 2\pi g_k g_j \omega_{nk} \sqrt{n+1} \left[\mp p(\omega_{nk} t_{kj}) + \sin\left(\omega_{nk} t_{kj}\right) \left(\frac{\pm 1 - 1}{2}\right)\right], \tag{5.35}$$

where $p(x)$ is defined as

$$p(x) \equiv \frac{\sin\left(|x|\right)\left[\pi - 2\mathrm{Si}\left(|x|\right)\right] - 2\cos\left(x\right)\mathrm{Ci}\left(|x|\right)}{2\pi}. \tag{5.36}$$

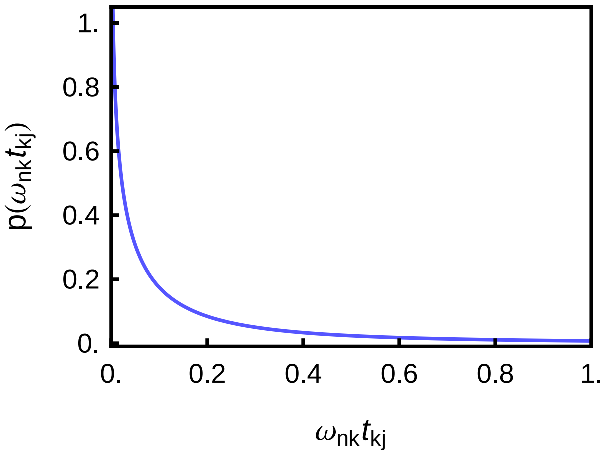

Figure 5.2: The function defined in (5.36) as a function of the distance between the qubits. We are mainly interested in $\omega_{nk}t_{kj} = 3/4$ and 1.

We plot this function in Fig. 5.2. The value of $p(x)$ goes to infinity when $x \rightarrow 0$, and approaches zero when $x \rightarrow 1$. That means it goes to infinity when the qubit separation approaches 0, which is of no concern as the qubits have finite size and can therefore not be at zero distance. We will be concerned with distances of the order of a wavelength. For qubits one wavelength apart, $p = 0.007$, and for qubits 3/4 wavelength apart $p = 0.012$. We see that the other factor in $\Omega_{kj}^{n+} = 0$, so that $p(x)$ determines the magnitude of the $n+$ terms. To interpret the meaning of these terms, we first collect the diagonal elements of the Ω-coefficient matrix and see how they enter equation (5.29) which governs the dynamics of an arbitrary qubit-only operator. We get the expression

$$L_{mj} = -\left(\sqrt{m+1}\Omega_{jj}^{m+} - \sqrt{m}\Omega_{jj}^{(m-1)-}\right). \tag{5.37}$$

From equations (5.35) and (5.36) we see that these terms present a problem, as (5.36) goes to ∞ when $\omega_{nk}t_{kj}$ goes to zero, which is the case for diagonal elements as they refer to the effect of a qubit on itself. This would mean the qubit causes an infinite shift of its own frequency by emitting and then reabsorbing photons at all frequencies - an infinite Lamb shift. This

problem is caused by the fact that so far we have considered the qubits to be pointlike. The lack of a finite size means the qubit can interact with arbitrarily high frequencies. In reality, the qubit has a finite spatial extent, and will not interact with modes of the continuum which correspond to wavelengths much smaller than the qubit size. As these diagonal Ω terms only present a shift in the qubit energy levels, we will later absorb this shift into the atomic part of the Hamiltonian.
Now that we found expressions for the drive strength and $\Omega_{jk}^{n\pm}$ coefficients which do not contain photonic operators, we can trace out the modes in the one-dimensional continuum from equation (5.29) to end up with an atom-only expression for the time-derivative of the atom-only operator $\hat{Q}$. We can then replace $\hat{Q}$ with $\hat{\rho}$, the atomic part of the density operator $\mathrm{Tr}_{\mathrm{P}}\left[\hat{\rho}_{\mathrm{T}}\right]$ obtained by performing a partial trace over the photonic modes on the complete density matrix $\hat{\rho}_{\mathrm{T}}$. This results in an expression for the dynamics of the reduced density matrix of the atoms:

$$
\begin{aligned}
\frac{d\hat{\rho}}{dt} =& \frac{i}{\hbar}\left[\hat{H}_A + \hbar\sum_{mj} d_{mj}(t)\hat{\sigma}_x^{mj}, \hat{\rho}\right] \\
&+ \sum_{mj}\sum_{nk}\sqrt{m+1}\Big[-i\Omega_{kj}^{n+}\left(\hat{\sigma}_x^{mj}\hat{\rho}\hat{\sigma}_+^{nk} - \hat{\rho}\hat{\sigma}_x^{mj}\hat{\sigma}_+^{nk} - \text{H.c.}\right) \\
&\qquad\qquad - i\Omega_{kj}^{n-}\left(\hat{\sigma}_x^{mj}\hat{\rho}\hat{\sigma}_-^{nk} - \hat{\rho}\hat{\sigma}_x^{mj}\hat{\sigma}_-^{nk} - \text{H.c.}\right) \\
&\qquad\qquad + \frac{\gamma_{kj}^{n}}{2}\left(\hat{\sigma}_x^{mj}\hat{\rho}\hat{\sigma}_-^{nk} - \hat{\rho}\hat{\sigma}_x^{mj}\hat{\sigma}_-^{nk} + \text{H.c.}\right)\Big].
\end{aligned}
\tag{5.38}
$$

5.1.5 Rotating wave approximation

The next step towards an effective multi-qubit master equation is to apply the rotating wave approximation. In (5.38), we have several terms containing combinations like $\hat{\rho}\hat{\sigma}_x^{mj}\hat{\sigma}_-^{nk}$, where $\hat{\sigma}_x^{mj} = \hat{\sigma}_+^{mj} + \hat{\sigma}_-^{mj}$. These terms can be written out as $\hat{\rho}(\hat{\sigma}_+^{mj}\hat{\sigma}_-^{nk} + \hat{\sigma}_-^{mj}\hat{\sigma}_-^{nk})$. Under the rotating wave approximation, only the first of these terms is preserved. Another justification for skipping the $\hat{\sigma}\_\hat{\sigma}\_$ term is that it does not preserve the number of excitations in the system and is therefore not allowed.

After the rotating wave equation, we have

$$\begin{aligned}\frac{d\hat{\rho}}{dt} =& -i\left[\frac{\hat{H}_A}{\hbar} + \sum_{mj} L_{mj}|m_j\rangle\langle m_j|, \hat{\rho}\right] \\ & - i\left[\sum_{mj} d_{mj}(t)\hat{\sigma}_x^{mj} + \sum_{mj}\sum_{nk} J_{mj,nk}\hat{\sigma}_+^{nk}\hat{\sigma}_-^{mj}, \hat{\rho}\right] \\ & + \sum_{mj}\sum_{nk}\left[\gamma_{mj,nk}\left(\hat{\sigma}_-^{mj}\hat{\rho}\hat{\sigma}_+^{nk} - \frac{1}{2}\left\{\hat{\sigma}_+^{nk}\hat{\sigma}_-^{mj}, \hat{\rho}\right\}\right)\right. \\ & \left. + \Omega_{mj,nk}\left(\hat{\sigma}_+^{mj}\hat{\rho}\hat{\sigma}_-^{nk} + \hat{\sigma}_-^{nk}\hat{\rho}\hat{\sigma}_+^{mj} - \left\{\hat{\sigma}_-^{nk}\hat{\sigma}_+^{mj}, \hat{\rho}\right\}\right)\right]. \end{aligned} \tag{5.39}$$

Several terms were combined to improve readability. The Ω^+ terms were combined to:

$$\Omega_{mj,nk} \equiv -i\left(\sqrt{n+1}\Omega_{jk}^{m+} - \sqrt{m+1}\Omega_{kj}^{n+}\right), \tag{5.40}$$

whereas all Ω^- terms have been omitted due to the rotating wave approximation. The magnitude of the remaining Ω terms at distances of the order of a wavelength is small due to the shape of (5.36), which is small for $\omega_{nk}t_{kj} \sim 1$, and we will neglect them. The magnitude of the error introduced by making the rotating-wave approximation and neglecting the Ω coefficients is discussed in appendix C3 of [Lalumière13], and was found to be small.

The γ terms in (5.38) are now split into $\gamma_{mj,nk}$ and $J_{mj,nk}$ terms, which we define according to

$$\frac{\gamma_{mj,nk}}{2\pi} \equiv g_k g_j \sqrt{(m+1)(n+1)}\left(\chi_{mkj} + \chi_{nkj}^*\right), \tag{5.41}$$

$$\frac{J_{mj,nk}}{2\pi} \equiv -i\frac{g_k g_j}{2}\sqrt{(m+1)(n+1)}\left(\chi_{njk} - \chi_{mkj}^*\right), \tag{5.42}$$

where we have defined $\chi_{mjk} \equiv \omega_{mj}e^{i\omega_{mj}t_{kj}}$, a factor related to the strength of the atom-atom interaction due to the mode resonant to them.

Absorbing the Lamb shift and neglecting the Ω terms, we finally arrive at an effective master equation for the qubits

$$\frac{d\hat{\rho}}{dt} = -\frac{i}{\hbar}\left[\hat{H}, \hat{\rho}\right] + \sum_{mj,nk}\gamma_{mj,nk}\left[\hat{\sigma}_-^{mj}\hat{\rho}\hat{\sigma}_+^{nk} - \frac{1}{2}\left\{\hat{\sigma}_+^{nk}\hat{\sigma}_-^{mj}, \hat{\rho}\right\}\right], \tag{5.43}$$

with the effective Hamiltonian

$$\hat{H} = \hat{H}_A + \hbar \sum_{mj} d_{mj}(t)\hat{\sigma}_x^{mj} + \hbar \sum_{mj,nk} J_{mj,nk}\hat{\sigma}_-^{mj}\hat{\sigma}_+^{nk}. \tag{5.44}$$

We will now take a closer look at the exchange interaction terms $J_{mj,nk}$ and the decay terms $\gamma_{mj,nk}$. When $j = k$, equation (5.41) denotes the single-qubit relaxation rate. Things become more interesting when $j \neq k$. We will be especially interested in the case where $\omega_{mj} = \omega_{nk}$, such that (5.41) is of the form

$$\gamma_{mj,nk} = 4\pi g_k g_j \omega_{mj} \sqrt{(m+1)(n+1)} \cos\left(\omega_{mj} t_{kj}\right), \tag{5.45}$$

which shows an oscillatory dependence on the distance between qubits j and k. This decay rate, which we will refer to as correlated decay of the qubits, is maximal whenever the qubits are an integer multiple of half wavelengths apart. The single-qubit decay rates, given by the diagonal elements $\gamma_{mj,nj}$, do not depend on distance as $t_{jj} = 0$.
The exchange interaction (5.42) for qubits in resonance is of the form

$$J_{mj,nk} = 2\pi g_k g_j \omega_{mj} \sqrt{(m+1)(n+1)} \sin\left(\omega_{mj} t_{kj}\right). \tag{5.46}$$

which has the same periodicity as correlated decay but with a different phase. The consequences are that whenever correlated decay is maximal, the exchange interaction is zero, and vice versa.

These equations, most notably (5.43) with (5.44), (5.41) and (5.42) represent the main theoretical results. In the remainder of this discussion, we will focus on simplifying these results for a two-qubit system, and look specifically at what is expected to happen at inter-qubit distances of $d = \lambda_r$ and $3\lambda_r/4$, in order to later compare the experiments performed for those distances to theoretical predictions.

5.1.6 Input-output theory

To relate theory to experiment, a connection must be made between the observed quantities and the qubit dynamics. We use input-output theory to obtain such a connection. When going from equation (5.9) to (5.10), we assumed that a time $t = 0$ exists at which no interactions have taken place yet, such that we could get the annihilation operator as a function of time

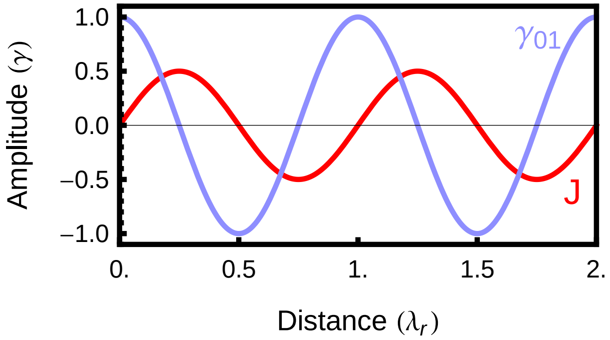

Figure 5.3: The correlated decay $\gamma_{01} = \gamma_{00,01}$ and the exchange interaction J oscillate as a function of the inter-qubit distance. Here we plotted both for transitions between the first two levels of two qubits.

by integrating the dynamics from this ‘time zero’ to the time of interest. Using the standard input-output theory approach [Gardiner85], we also do the opposite – we assume there is a final time t_f at which interactions have stopped, and integrate backwards from there to get an expression for the annihilation operator at time t:

$$\hat{a}_{\mathrm{R}}(\omega, t) = \hat{a}_{\mathrm{R}}(\omega, t_f)e^{-i\omega t} - \sum_{mj} g_j \sqrt{m+1}\sqrt{\omega} \int_t^{t_f} d\tau e^{-i\omega(t-\tau+x_j/v)} \hat{\sigma}_x^{mj}(\tau). \tag{5.47}$$

Combining this result with the result we got from integrating from t_0 to t (equation (5.10)), we get

$$\hat{a}^{\mathrm{R}}_{\mathrm{out}}(t) = \hat{a}^{\mathrm{R}}_{\mathrm{in}}(t) + \sum_{mj} g_j \sqrt{m+1} \int_0^{\infty} \frac{d\omega}{\sqrt{2\pi}} \sqrt{\omega} \int_0^{t_f} d\tau e^{-i\omega(t-\tau+x_j/v)} \hat{\sigma}_x^{mj}(\tau), \tag{5.48}$$

where $\hat{a}^{\mathrm{R}}_{\mathrm{in}}(t)$ and $\hat{a}^{\mathrm{R}}_{\mathrm{out}}(t)$ are inverse Fourier transforms of their frequency-domain counterparts:

$$\hat{a}^{\mathrm{R}}_{\mathrm{in}}(t) = \int_0^{\infty} \frac{d\omega}{\sqrt{2\pi}} \hat{a}_{\mathrm{R}}(\omega, 0)e^{-i\omega t}, \tag{5.49}$$

$$\hat{a}^{\mathrm{R}}_{\mathrm{out}}(t) = \int_0^{\infty} \frac{d\omega}{\sqrt{2\pi}} \hat{a}_{\mathrm{R}}(\omega, t_f)e^{-i\omega t}. \tag{5.50}$$

The suffix 'in' denotes radiation before interaction with the multi-qubit system, whereas 'out' denotes radiation that has interacted with the qubits and is now propagating away from the system. Using the Markov and long-time approximations as outlined in section (5.1.2), we can get rid of the τ-dependence of the $\hat{\sigma}$ terms, and using the definition of $\gamma_{mj,nk}$ (5.41) we can rewrite (5.48) to read

$$\hat{a}^{\mathrm{R}}_{\mathrm{out}}(t) = \hat{a}^{\mathrm{R}}_{\mathrm{in}}(t) + \sum_{mj} e^{-i\omega_{mj}t_j} \sqrt{\frac{\gamma_{mj,mj}}{2}} \hat{\sigma}^{mj}_{-}, \tag{5.51}$$

and, similarly, for the left-moving field,

$$\hat{a}^{\mathrm{L}}_{\mathrm{out}}(t) = \hat{a}^{\mathrm{L}}_{\mathrm{in}}(t) + \sum_{mj} e^{+i\omega_{mj}t_j} \sqrt{\frac{\gamma_{mj,mj}}{2}} \hat{\sigma}^{mj}_{-}. \tag{5.52}$$

When an experiment is carried out, we measure the reflectance and transmittance. These are connected to the input and output fields according to

$$|t|^2 = \left| \frac{\left\langle \hat{a}^{\mathrm{L}}_{\mathrm{out}} \right\rangle}{\left\langle \hat{a}^{\mathrm{L}}_{\mathrm{in}} \right\rangle} \right|^2, \qquad |r|^2 = \left| \frac{\left\langle \hat{a}^{\mathrm{R}}_{\mathrm{out}} \right\rangle}{\left\langle \hat{a}^{\mathrm{L}}_{\mathrm{in}} \right\rangle} \right|^2. \tag{5.53}$$

Furthermore, for power spectral densities we have the following relation between the measured spectrum and the fields [Clerk10]

$$S^{\alpha}[\omega] = \int_{-\infty}^{\infty} dt e^{i\omega t} \langle \hat{a}^{\alpha\dagger}_{\mathrm{out}}(t) \hat{a}^{\alpha}_{\mathrm{out}}(0) \rangle, \tag{5.54}$$

where $\alpha \in \{\mathrm{R}, \mathrm{L}\}$.

5.1.7 Two two-level systems

We have obtained an effective master equation for a system of N M-level systems in equation (5.43), which will allow us to numerically calculate how the qubits will behave even when the transmon cannot be approximated as a two-level system. However, the general validity of the model does not help for developing an intuitive understanding. Limiting the system to two qubits which have only two levels each will allow for analytical results.

Taking the master equation (5.43), restricting it to two two-level systems and moving to a frame rotating at a drive frequency ω_d results in

$$\frac{d\hat{\rho}}{dt} = -\frac{i}{\hbar}\left[\hat{H}, \hat{\rho}\right] + \sum_{jk} \gamma_{jk} \left[\hat{\sigma}_-^j \hat{\rho} \hat{\sigma}_+^k - \frac{1}{2}\left\{\hat{\sigma}_+^k \hat{\sigma}_-^j, \hat{\rho}\right\}\right]. \tag{5.55}$$

The Hamiltonian is now given by

$$\hat{H}/\hbar = \sum_j \Delta_j |e_j\rangle\langle e_j| + \sum_j \left(\epsilon_j \hat{\sigma}_+^j + \mathrm{H.c.}\right) + J(\hat{\sigma}_-^1 \hat{\sigma}_+^2 + \hat{\sigma}_+^1 \hat{\sigma}_-^2). \tag{5.56}$$

Here, Δ_j is the detuning between qubit j and the drive, $J = J_{01,02}$ is the exchange interaction between qubit 1 and 2, and $\gamma_{jk} \equiv \gamma_{0j,0k} + \gamma_{\mathrm{nr}}^j \delta_{jk}$ where we have introduced the non-radiative decay rate γ_{nr}, the rate at which radiation couples into other channels than the transmission line. In chapter 3, we have experimentally confirmed an upper limit to this rate showing that $\gamma_{\mathrm{nr}} \ll \gamma_{\mathrm{r}}$, with γ_{r} the rate of decay into the transmission line.
In experiment, the system is driven by a coherent tone from one side, which is here chosen to be the left side. Moving equation (5.28) to the rotating frame, applying the rotating wave approximation and using that $\sqrt{P_L} = \sqrt{\hbar\omega_d}\langle \hat{a}_{\mathrm{in}}^{\mathrm{L}} \rangle$, we get a more simple equation for the drive strength:

$$\epsilon_j = -i\sqrt{\frac{\gamma_{0j,0j}\omega_d}{2\omega_{0j}}} \left\langle \hat{a}_{\mathrm{in}}^{\mathrm{L}} \right\rangle e^{-i\omega_d t_j}. \tag{5.57}$$

To get the dressed master equation into the standard Lindblad form, a basis transformation is performed that diagonalizes the matrix of decay terms γ_{jk}. The details of this this diagonalization are omitted here, but can be found in appendix G in [Lalumière13]. In the new basis, the dissipator in (5.55) has the standard form

$$\sum_{\mu=B,D} \Gamma_\mu \mathcal{D}\left[\hat{\sigma}_-^\mu\right] \hat{\rho}, \tag{5.58}$$

with $\mathcal{D}[\hat{x}]\hat{\rho} = \hat{x}\hat{\rho}\hat{x}^\dagger - \left\{\hat{x}^\dagger \hat{x}, \hat{\rho}\right\}/2$ the usual dissipation superoperator. The atomic operators, under this basis transformation, are now defined as

$$\hat{\sigma}_-^\mu = \frac{\left(\Gamma_\mu - \gamma_{22}\right)\hat{\sigma}_-^1 + \gamma_{12}^* \hat{\sigma}_-^2}{\sqrt{\left(\Gamma_\mu - \gamma_{22}\right)^2 + |\gamma_{12}|^2}}, \tag{5.59}$$

where we have chosen the suffixes $\mu \in \{B, D\}$ for reasons that will become clear later. The decay rates Γ_μ are given by

$$\Gamma_{B/D} = \frac{\gamma_{11} + \gamma_{22}}{2} \pm \sqrt{\left(\frac{\gamma_{11} - \gamma_{22}}{2}\right)^2 + |\gamma_{12}|^2}, \tag{5.60}$$

The interaction effects between two qubits are best summarized by the joint decay rate (5.45) and the exchange interaction (5.46). For two two-level systems in resonance ($\omega_r = \omega_1 = \omega_2$), these can be simplified to

$$\frac{\gamma_{j,k}}{2\pi} = 2 g_k g_j \omega_r \cos\left(\omega_r t_{kj}\right), \tag{5.61}$$

and

$$\frac{J}{2\pi} = g_k g_j \omega_r \sin\left(\omega_r t_{kj}\right). \tag{5.62}$$

We will now look in detail at the situations which were most thoroughly investigated in experiment: two qubits are tuned into resonance, and we will express the inter-qubit distance, as before, in units of this resonant wavelength λ_r. Below we will focus on distances of $d = \lambda_r$ and $d = 3\lambda_r/4$ of the wavelength at their transition frequency.

5.1.8 Two qubits one wavelength apart – super- and subradiance

For two two-level systems one wavelength apart (Fig. 5.4A), the mathematical description of the system can be significantly simplified. Apart from limiting ourselves to two levels for each qubit, we will also assume that the non-radiative decay rates for both qubits are identical $\gamma_{\mathrm{nr}}^1 = \gamma_{\mathrm{nr}}^2$. The correlated decay rate for this situation is given by the off-diagonal elements of the decay matrix given by (5.61) while remembering that $\gamma_{jk} = \gamma_{0j,0k} + \gamma_{\mathrm{nr}}^j \delta_{jk}$. We then get

$$\gamma_{12} = \pm\sqrt{(\gamma_{11} - \gamma_{\mathrm{nr}})(\gamma_{22} - \gamma_{\mathrm{nr}})}. \tag{5.63}$$

from this in combination with (5.60) we get the decay rates for the eigenstates $|B\rangle$ and $|D\rangle$

$$\Gamma_D = \gamma_{\mathrm{nr}} \ll \Gamma_B = \gamma_{11} + \gamma_{22} - \gamma_{\mathrm{nr}}. \tag{5.64}$$

The decay rate $|D\rangle$ being equal to the non-radiative decay rate γ_{nr} means that this state only relaxes into channels other than the transmission line.

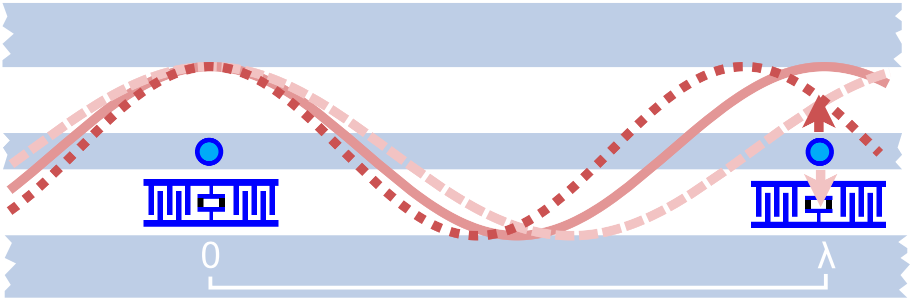

Figure 5.4: Schematic for two qubits at one wavelength distance. The continuous line shows that both qubits see the same phase of the field of a resonant drive tone or vacuum fluctuation.

In other words, the state is dark. $|B\rangle$, on the other hand, decays nearly twice as fast as a single qubit, and we call this state bright. States that radiate more or less than a single qubit state are also known as super- and subradiant states, respectively [DeVoe96, González-Tudela13]. To understand this phenomenon, we start by observing that for two resonant qubits separated by λ_r, the expression for the exchange interaction (5.62) predicts J to be zero. This implies that the four-level system formed by the two qubits has two levels exactly in resonance: $|ge\rangle$ and $|eg\rangle$, which are therefore indistinguishable. The eigenstates in this situation are then the symmetric and antisymmetric combinations of $|ge\rangle$ and $|eg\rangle$:

$$|B\rangle = (|ge\rangle + |eg\rangle)/\sqrt{2}, \qquad |D\rangle = (|ge\rangle - |eg\rangle)/\sqrt{2}. \tag{5.65}$$

When driving the system with a coherent tone of the same frequency as the two-qubit system, the drive has the same phase at the position of both qubits (Fig. 5.4, continuous line). This can also be seen from equation (5.57): $\omega_d(t_k - t_j) = 2\pi$. The bright state, which has the same phase difference between the single-qubit excited states $|ge\rangle$ and $|eg\rangle$, therefore couples strongly to the drive, but the dark state, having opposite symmetry, does not. This causes the dark state not to be driven by the drive tone, while the bright state is strongly driven. Similarly, relaxation of the qubit is caused by vacuum fluctuations in the mode resonant with the qubits, which also have the same phase relation between the two qubits as the drive tone, such that the dark state cannot decay into the resonant vacuum mode. This causes the dark state to be long-lived. A similar phenomenon was observed in circuit QED [Filipp11] and with directly coupled superconducting flux qubits [deGroot10].

Another way to see that the dark state can neither be driven nor decay to first order follows from the dressed Hamiltonian (5.56). When the drive is resonant to the qubits, $\Delta_j = 0$, and as stated before J is also 0 at this qubit separation. Furthermore, we can arbitrarily take the phase of the drive at the first qubit to be $3\pi/2$, such that the drive at qubit j simplifies to $\epsilon_j = \sqrt{\gamma_{0j,0j}/2}\left\langle \hat{a}_{\text{in}}^{\text{L}} \right\rangle$, and the Hamiltonian simplifies to

$$\hat{H}_{simp}/\hbar = \epsilon_1 \hat{\sigma}_x^1 + \epsilon_2 \hat{\sigma}_x^2. \tag{5.66}$$

Calculating the transition matrix elements $|\langle gg|\hat{H}|D\rangle|$ between the dark state and the ground state (or doubly excited state) then gives 0 when $\gamma_{00,00} = \gamma_{01,01}$. When the decay rates are not the same, this is not the case. Some of the transition matrix elements as a function of drive asymmetry are shown in Fig. 5.5b. Unequal qubit decay rates can cause the dark state to be populated from the ground state $|gg\rangle$ and the doubly excited state $|ee\rangle$. There are other reasons than decay asymmetry for the state to not be perfectly dark. Nonzero pure dephasing causes transitions between $|B\rangle$ and $|D\rangle$. Nonzero non-radiative decay is decay due to resonant modes outside the transmission line, and therefore does not need to couple to both qubits with the same phase. Non-radiative decay mechanisms have been (and still are) under much investigation for superconducting qubits [Bylander11, Gustavsson11]. The origin of non-radiative decay is thought to be microscopic, and this microscopic noise has been observed to be local [Yoshihara10] (i.e., the noise causing correlated decay at qubit one is thought to be uncorrelated to the noise causing non-radiative decay at qubit two). Therefore, non-radiative decay in our system is expected to contribute to an asymmetry in the single-qubit decay rates.

We should emphasize at this point that the presented predictions, although specifically stated for an inter-qubit distance of one wavelength, will be valid for every distance that is an integer multiple of half a wavelength ($N\lambda_r/2$ for $N \in \mathbb{N}$), but only at integer multiples ($N\lambda_r$) of the wavelength will the symmetric state be bright and the antisymmetric dark. At the other distances that are multiples of half a wavelength ($(2N-1)\lambda_r/2$), the antisymmetric

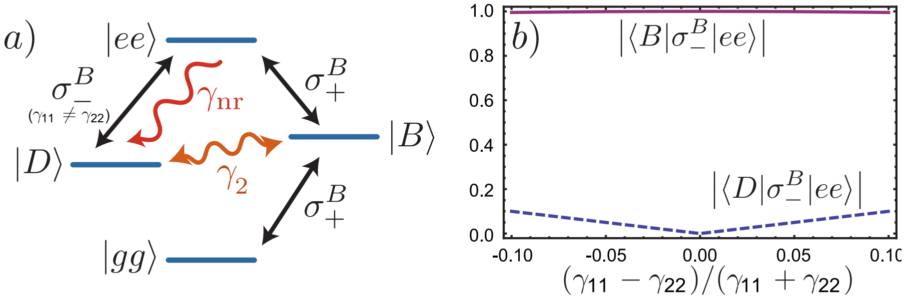

Figure 5.5: (a) When two qubits are exactly in resonance, exchange interaction is absent and the two two-level systems form a dark and a bright state. (b) Transition elements between the doubly excited state and the bright and dark state become nonzero when the decay rates of both qubits are not identical. Figure adapted from [Lalumière13].

state will be bright and the symmetric state dark.

Elastically scattered radiation

In experiment, we either measure the transmittance or reflectance of elastically scattered radiation, or power spectral densities. We will now focus on elastically scattered radiation. Assuming that the decay rates for both qubits are identical $\gamma = \gamma_{00} = \gamma_{11}$, we work out (5.51) and (5.52) for two resonant two-level systems at a distance of $d = \lambda_r$ to get:

$$\hat{a}_{\text{out}}^{\text{R/L}} = \hat{a}_{\text{in}}^{\text{R/L}} \pm i\sqrt{\gamma_{\text{r}}}\hat{\sigma}_-^B. \tag{5.67}$$

where $\gamma_{\text{r}} = \gamma - \gamma_{\text{nr}}$ as before. The expectation value of $\hat{\sigma}_-^B$ can be obtained by calculating the steady-state solution of the master equation (5.55). The expectation values of the outgoing fields are then, to first order in the input fields

$$\left\langle \hat{a}_{\text{out}}^{\text{R}} \right\rangle = \left\langle \hat{a}_{\text{in}}^{\text{L}} \right\rangle \frac{-i(\Gamma_B - \gamma_{\text{nr}})/2}{\Delta - i\Gamma_B/2}, \tag{5.68}$$

$$\left\langle \hat{a}_{\text{out}}^{\text{L}} \right\rangle = \left\langle \hat{a}_{\text{in}}^{\text{L}} \right\rangle \left(1 - \frac{-i(\Gamma_B - \gamma_{\text{nr}})/2}{\Delta - i\Gamma_B/2}\right). \tag{5.69}$$

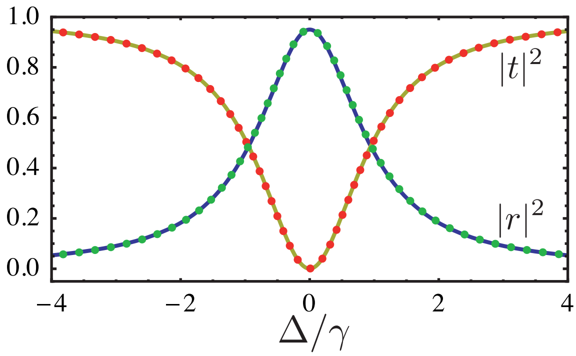

Figure 5.6: Transmittance and reflectance for two qubits one wavelength apart for at low drive powers. The width of reflectance and transmittance peaks are given by $\Gamma_B \sim 2\gamma$. Numerical calculations using the full model are plotted in dots, while continuous lines are due to analytical results. Here we chose $\gamma_\mathrm{r} = 0.95\gamma$. Figure from [Lalumière13].

These fields are plotted in Fig. 5.6, where the dots represent numerical calculations using the master equation (5.43) for 2 M-level systems, while the lines represent analytical results obtained from (5.67) and (5.69). The agreement between these two models is excellent for low drive powers. The results resemble those for a single qubit. Under low drive powers (so that $|ee\rangle$ remains unpopulated) and as long as the non-radiative decay and pure dephasing rate are low compared to the radiative decay rate (such that $|D\rangle$ does not get populated), the four-level system can be seen as being reduced to only consisting of the ground $|gg\rangle$ and bright $|B\rangle$ states, where the bright state has a decay rate twice that of a single qubit.

Inelastically scattered radiation

In the limit of low drive power, no pure dephasing and no non-radiative decay, such that the system can be seen as consisting only of the ground and bright states, the power spectral density for the four-level is of the same shape as for a two-level system [Walls08]:

$$S^{R/L}[\omega] = \frac{8{\epsilon_B^{\text{eff}}}^4}{[(\Gamma_B/2)^2 + \omega^2]^2}, \tag{5.70}$$

where ϵ_B^{eff} is the effective drive amplitude for the bright state. The power spectral density under these assumptions is plotted in Fig. 5.7a using both the full model according to (5.43) and the above formula. The agreement between numerical and analytic results is again excellent. However, as soon as any of these approximations is not valid, the analytical results for the power spectral density cannot be used, and the full numerical calculation based on (5.43) is the only recourse. In Fig. 5.7b, the same spectrum is plotted for two nonzero values of the non-radiative decay rate: $\gamma_{\text{nr}}/\gamma_{\text{r}} = 0.1$ and 0.01. For the latter condition, a narrow peak emerges out of the wide peak of the bright state, its narrow shape indicating its long lifetime. This sharp peak should not be confused with the elastically scattered contribution, which is of vanishing width and which has been removed in these figures. When the non-radiative decay is increased, the discernibility of the dark state decreases (note that curves in panels (a) and (b) have been normalized such that their maxima are 1; the total power observed does not increase with $\gamma_{\text{nr}}/\gamma_{\text{r}}$ as one might otherwise be led to conclude). The visibility of the dark state is shown to vary with $\gamma_{\text{nr}}/\gamma_{\text{r}}$ in figure 5.7c. Assuming that the non-radiative decay is caused by microscopic mechanisms coupling to the qubits in an uncorrelated way, it causes the two-qubit system to decay for example from the dark state $(|ge\rangle - |eg\rangle)/\sqrt{2}$ to states like $(|ge\rangle - |gg\rangle)/\sqrt{2}$. This new state, and other states due to single-qubit decay into other channels than the transmission line, have nonzero matrix elements towards the ground state. The effect of non-radiative decay can then be seen as simultaneously decreasing the lifetime of the dark state and increasing the lifetime of the bright state, effectively pulling the two-qubit system from this asymmetric dark-bright state configuration towards a more symmetric one where the states have equal lifetimes. Only when non-radiative decay rates are low ($\gamma_{\text{r}} \gg \gamma_{\text{nr}}$), such as in a system of transmon qubits in an open transmission line, we have that $\Gamma_B \gg \Gamma_D$.

The visibility of the dark state is also affected by the asymmetry in the qubit decay rates $\gamma_{jj} = \gamma_{0j,0j} + \gamma_{\text{nr}}^j$, which were taken to be equal in Fig. 5.7. Taking $\gamma_{\text{nr}}/\gamma_{\text{r}} = 0.01$, which rendered the dark state highly visible in Fig. 5.7b, the effect of asymmetry in the qubit decay rates on the dark state is explored in Fig. 5.8. Using the simplified model from above (5.66) where qubits are driven with the same phase but a different amplitude (since ϵ_j depends on $\gamma_{0j,0j}$, that is implied when decay rates are unequal), it can be immediately seen that the dark state can be driven: $|\langle D|\hat{H}_{simp}|gg\rangle| = |\epsilon_2 - \epsilon_1|/\sqrt{2}$, even in the absence of γ_{nr} and γ_φ. The nonzero transition matrix element also means that the dark state can now decay, albeit with a rate much lower than Γ_B, which widens the peak of the dark state.

5.1.9 Qubits three quarter wavelengths apart – exchange interaction

The situation is very different for two qubits spaced three quarters of a wavelength apart (5.9). The qubits are now driven $\pi/2$ out of phase, which kills correlated relaxation ($\gamma_{12} = 0$). On the other hand, the exchange interaction J is maximal at this distance (and other distances equal to $d = (2N+1)\lambda_r/4$, $N \in \mathbb{N}$), with $|J| = \gamma_r/2$.
Here too, it is possible to understand intuitively why J is maximal at these distances, and why it is zero at distances $d = N\lambda_r$. As with any exchange interaction, here too J is caused by virtual processes - the qubits interact with modes not at their resonance frequency. Each mode in the one-dimensional continuum contributes to the exchange interaction, but the strength of the contribution depends both on the detuning between the mode and the two-qubit system, and the different phase which both qubits experience from this mode as $J_i = g_1 g_2/\Delta_i$, with J_i the contribution to the exchange interaction by mode i, and $g_1 g_2$ the relative coupling of the two-qubit system to this mode due to the phase difference the mode develops between the locations of the qubit. This last argument is very similar to the argument presented when discussing the super- and subradiant state (see Fig. 5.4). However, where we looked at the coupling of the resonant mode to the qubits for correlated decay, for exchange interaction we look at the off-resonant modes.

We first look at the situation where $d = \lambda_r$. In Fig. 5.4, except for the resonant mode indicated by the continuous line, two other modes are indicated which are detuned by δ and $-\delta$. The fact that both qubits see the same field magnitude for the positively and negatively detuned modes signifies that the product $g_1 g_2$ is the same for these modes. However, since the detuning

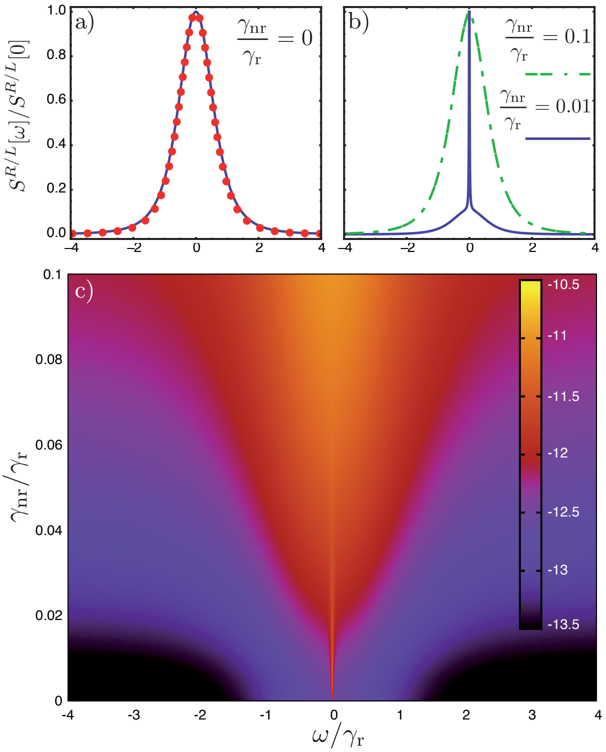

Figure 5.7: Power spectral density of two qubits one wavelength apart as a function of frequency in units of γ_{r}, driven by a weak coherent tone ($\epsilon_B = \gamma_{\mathrm{r}}/200$). In (a), the pure dephasing rate and non-radiative decay rates are set to zero. The analytical (continuous line) and numerical results (dots) agree well in that situation. Introducing a finite non-radiative decay rate (b) introduces features not captured by the analytics – the narrow peak shows the presence of the dark state. The curves were rescaled to the full range of the y-axes in panels (a) and (b). In (c), the logarithm of the power spectral density is plotted in color as a function of the magnitude of non-radiative decay. Pure dephasing was kept to zero. Figure from [Lalumière13].

is of opposite sign, the contribution of these modes to the total exchange interaction is also of opposite sign $J_\delta = -J_{-\delta}$, and their contribution to

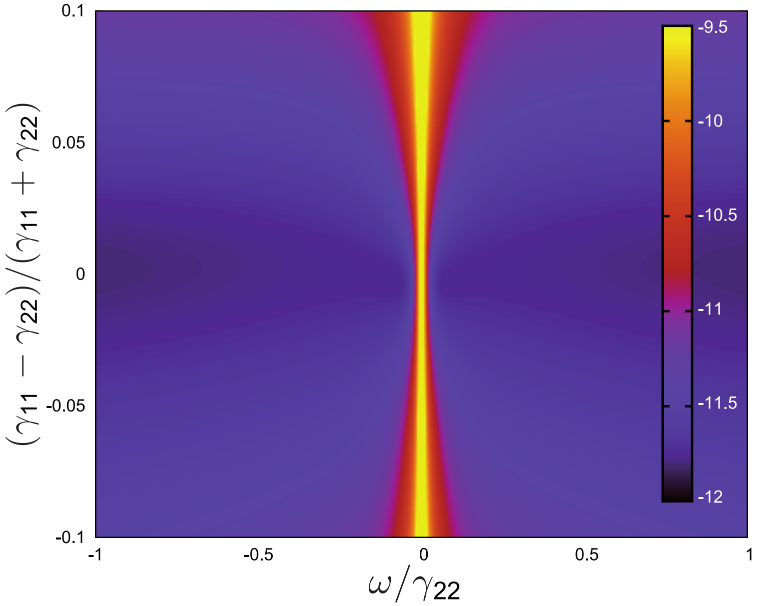

Figure 5.8: Logarithm of the power spectral density (color) for two qubits at a distance of one wavelength driven by a weak coherent tone ($\epsilon_B = \gamma_{\rm r}/200$) as a function of the asymmetry in the qubit decay rates $(\gamma_{11}-\gamma_{22})/(\gamma_{11}+\gamma_{22}$. $\gamma_{\rm nr}/\gamma_{\rm r} = 0.01$. The line in the center is the dark state. Increasing the asymmetry between qubit relaxation rates increases the width of this state. Figure adapted from [Lalumière13].

the total exchange interaction $J = \sum_i J_i$ cancels out. This reasoning can be applied for any set of positively and negatively detuned modes, and it is found that the total exchange interaction is exactly zero for qubits $d = \lambda_r$ apart.

The same reasoning applies to qubits $3\lambda_r/4$ apart. However, as can be seen in figure 5.9, the qubits now experience equal but opposite fields due to modes detuned by δ and $-\delta$, resulting in $J_\delta = J_{-\delta}$. All contributions to the total exchange interaction now add up, resulting in $|J|$ reaching its maximum value of $\gamma_{\rm r}/2$. The distance-dependence of J thus showcases the importance of interference in virtual processes.

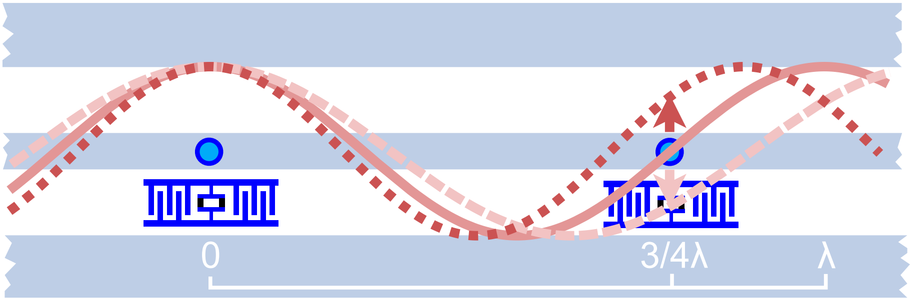

Figure 5.9: Schematic of a system of two qubits three quarters of a wavelength apart. The continuous line shows the resonant mode, while the dashed lines represent a positively and negatively detuned mode.

Elastically scattered radiation

Rewriting (5.51) (5.52) for two qubits $3\lambda_r/4$ apart, the output fields are given by

$$\hat{a}^{\mathrm{R}}_{\mathrm{out}}(t) = \sqrt{\frac{\gamma_{\mathrm{r}}}{2}} e^{-i\omega_1 t_1} \left[\hat{\sigma}^1_- - i\mathrm{Sign}\left(J\right)\hat{\sigma}^2_-\right], \tag{5.71}$$

$$\hat{a}^{\mathrm{L}}_{\mathrm{out}}(t) = \hat{a}^{\mathrm{L}}_{\mathrm{in}} + \sqrt{\frac{\gamma_{\mathrm{r}}}{2}} e^{i\omega_1 t_1} \left[\hat{\sigma}^1_- + i\mathrm{Sign}\left(J\right)\hat{\sigma}^2_-\right]. \tag{5.72}$$

which, by solving the master equation of the dressed system (5.55) for a steady state and writing the terms to first order in $\left\langle \hat{a}^{\mathrm{L}}_{\mathrm{in}} \right\rangle$, gives

$$\left\langle \hat{a}^{\mathrm{L}}_{\mathrm{out}} \right\rangle = \left\langle \hat{a}^{\mathrm{L}}_{\mathrm{in}} \right\rangle \frac{J^2 - (\Delta - i\gamma/2)\left(\Delta + i(\gamma_{\mathrm{r}} - \gamma/2)\right)}{J^2 - (\Delta - i\gamma/2)^2}, \tag{5.73}$$

$$\left\langle \hat{a}^{\mathrm{R}}_{\mathrm{out}} \right\rangle = \left\langle \hat{a}^{\mathrm{L}}_{\mathrm{in}} \right\rangle \frac{-|J|\gamma_{\mathrm{r}}}{J^2 - (\Delta - i\gamma/2)^2}. \tag{5.74}$$

The transmittance and reflectance expected from these equations are plotted for two different powers in Fig. 5.10. For low powers (panel a), where the above expressions are valid, we again find that transmittance goes to zero and reflectance to one. However, a big difference between the case of qubits separated by λ_r and $3\lambda_r/4$ is that the latter distance results in a peak width of γ, instead of the 2γ observed for the former at low drive powers. This is because the 2γ found for qubits λ_r apart was due to correlated decay being maximal, while it is absent at $d = 3\lambda_r/4$. This difference was also predicted by the semi-classical transfer matrix model 4.2.2, which leads us to conclude that correlated relaxation is predicted by transfer matrix theory. The flatness of the peaks in Fig. 5.10a is due to the exchange interaction – as the maximum exchange interaction is $\gamma_\mathrm{r}/2$, it will not result in a level splitting with two distinguishable peaks, but instead to a single flattened peak. The analytical results (continuous line in Fig. 5.10a) and numerical results (dots in the same) once again agree very well for low drive powers. At higher drive powers, only the numerical calculations can be used, results of which are shown in Fig. 5.10b for similar parameters as used in experiments presented earlier (in section 4.1, most notably Fig. 4.2). We stress again that the splitting seen in reflectance in Fig. 5.10 is not due to exchange interaction, but due to the two-qubit system being dressed by the strong drive, resulting in an Autler-Townes splitting. The strong deviation of $|t|^2 + |r|^2$ from 1 is also an effect of the increased inelastic scattering in a strongly driven system - inelastic scattering causes the two-qubit system to redistribute power from the resonant mode to modes at the surrounding frequencies, decreasing the power in the mode observed when measuring elastically scattered radiation.

Inelastically scattered radiation

In this section we present numerical calculations of the power spectral densities for a system of 2 qubits $3\lambda_r/4$ apart, based on equation (5.43). The power spectral densities are calculated both for the reflected and transmitted field, and are plotted in Fig. 5.11. In panel a, the power spectral density at low drive power is reflected and transmitted fields, and their sum. For simplicity, the single qubit decay rates were chosen to be equal, and pure dephasing and non-radiative decay were set to zero. The power spectral density shows two peaks, which is a fingerprint of the exchange interaction. The total spectrum shows a splitting of $2J$, but the reflected and transmitted field show a slightly smaller and bigger splitting, respectively. These numerical results can be replicated by introducing an angle ϕ, such that

$$\hat{A}(t,\phi) = \hat{\sigma}_-^B(t) + e^{i\phi}\hat{\sigma}_-^D(t). \tag{5.75}$$

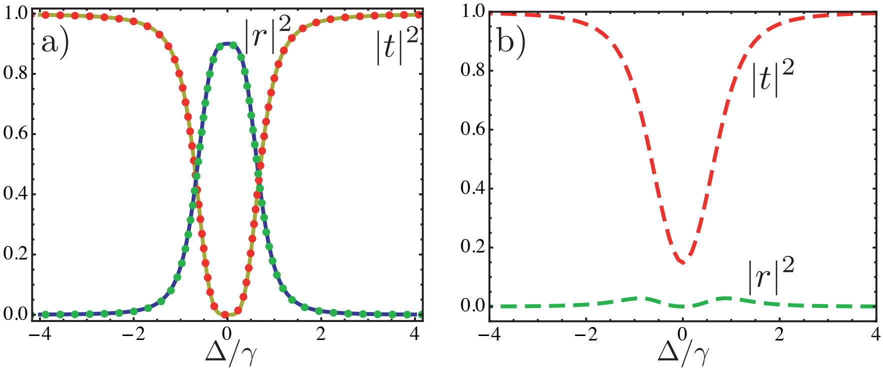

Figure 5.10: Elastically scattered light for qubits $3\lambda_r/4$ apart at different powers. In (a), the drive power is set to $\epsilon_0 = \gamma/200$. Continuous lines represent the analytical results from (5.74) and (5.73), while the dots result from numerical calculation based on the full master equation model (5.43). In (b) the drive is increased to $\epsilon = 0.35\gamma$. Figure from [Lalumière13].

where $\hat{\sigma}_-^{B/D} = (\hat{\sigma}_-^2 \pm \hat{\sigma}_-^1)/\sqrt{2}$ are the lowering operators obtained when diagonalizing the dressed Hamiltonian for $d = 3\lambda_r/4$. It should be stressed here that while we kept the B, D labels, the states are not bright or dark. These new simplified operators serve as simplified versions of $\hat{a}_{\text{out}}^{\text{R/L}}$, where the angle defines if we are looking at the output field in reflectance, transmittance, or under another angle. Comparison with equations (5.71) and (5.72) shows that $\hat{A}(t, \pi/2)$ is similar to $\hat{a}_{\text{out}}^{\text{L}}(t)$ and $\hat{A}(t, 3\pi/2)$ resembles $\hat{a}_{\text{out}}^{\text{R}}$. We now introduce the angle-dependant power spectral density function according to

$$S[\omega, \phi] = \frac{\gamma_{\text{r}}}{2} \int_{-\infty}^{\infty} dt e^{i\omega t} \langle \hat{A}^\dagger(t, \phi) \hat{A}(0, \phi) \rangle, \tag{5.76}$$

where the contribution due to $\langle \hat{a}_{\text{in}} \rangle$ was removed to improve readability. The transmitted and reflected power spectral densities are then given by $S[\omega, \pi/2]$ and $S[\omega, 3\pi/2]$, respectively. The spectrum is plotted as a function of this angle in Fig. 5.11c. In Fig. 5.11b, the spectrum is plotted for two values of asymmetry between the single qubit relaxation rates (red and green lines), which affect the contrast between the dip at the center and the peaks at the sides of the spectrum, while non-radiative decay rate decreases both this contrast and the total power measured.

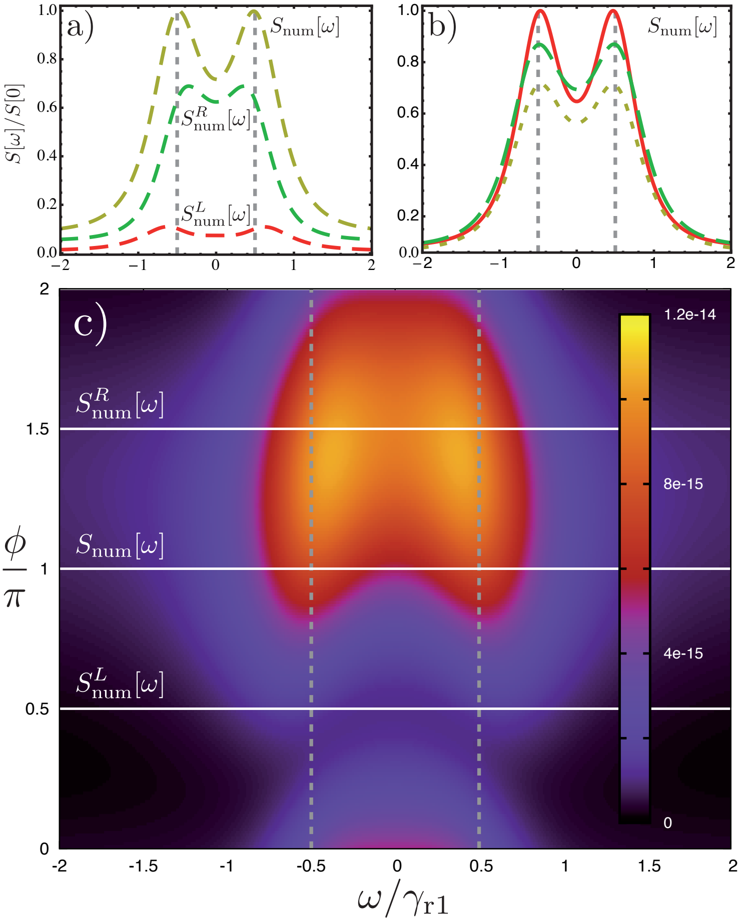

Figure 5.11: Power spectral densities for two qubits in resonance at a distance of $3\lambda/4$. (a) The reflected, transmitted and total power spectral density for $\gamma_{\mathrm{nr}} = 0$. (b) The shape of the power spectral density depends on the asymmetry in the single qubit decay rates, as shown in the red and green lines for $(\gamma_{11}-\gamma_{22})/(\gamma_{11}+\gamma_{22}) = (0.9, 1.1)$ respectively. The yellow line shows the effect of non-radiative decay $\gamma_{\mathrm{nr}}/\gamma_{\mathrm{r}} = 0.1$ when the qubit decay rates are the same. (c) The power spectral density (color) is plotted as a function of detuning and the angle ϕ (see text). Figure from [Lalumière13].

5.2 Inelastic scattering properties of a system of two distant qubits

A careful analysis of the process of observation in atomic physics has shown that the subatomic particles have no meaning as isolated entities, but can only be understood as interconnections between the preparation of an experiment and the subsequent measurement. - Erwin Schrödinger

In this section, we will show the results of resonance fluorescence measurements on a system of two distant qubits in an open transmission line. Resonance fluorescence measurements, done here according to the method described in chapter 2, reveal the full spectrum of radiation scattered by the qubits into the transmission line, including the inelastically scattered radiation. As such, these measurements give us additional insights into the properties of the two-qubit system and allow us to see the interaction phenomena predicted by theory. The main results in this chapter were published in [vanLoo13].

5.2.1 Power spectral density measurements for two qubits at 4.8 and 6.4 GHz

Two single-qubit Mollow triplets were measured at 6.1 GHz to determine the difference in coupling between these qubits. Fitting the Mollow triplets at a drive power of -118 dBm with equation (3.28), the Rabi rates were found to be nearly identical: 65.7 MHz for qubit A, and 66.1 MHz for qubit B (Fig. 5.12). The qubits therefore couple to the transmission line with nearly equal strength.

To investigate the two-qubit interactions, the two qubits were first tuned to 4.8 GHz ($d = 3\lambda_r/4$). A strong continuous-wave drive was applied through the transmission line, and the resonance fluorescence spectrum of the two-qubit system was recorded (Fig. 5.13) in transmission. At high drive powers, the resulting spectrum looks similar to that of a single qubit under a strong drive - a Mollow triplet emerges. When the drive power is reduced, the side peaks become unresolvable from the center peak (yellow line in Fig. 5.13), and at even lower powers a two-peak structure appears. This splitting of the spectrum into two peaks is the fingerprint of the exchange interaction, which is expected to be maximal at this effective inter-qubit distance. The observed size of the splitting is 15 MHz. Theory predicts that a splitting

which is observed in transmission will be slightly larger than $2J$. A fit with the full master equation of the system (5.43) (details of the fitting procedure are discussed separately in section 5.2.2) reveals that the strength of the exchange interaction between the two qubits is $2J/2\pi = 13$ MHz. The full splitting $2J$ is therefore equal in magnitude to the single-qubit relaxation time, as predicted in equation (5.62). As far as the author is aware, this exchange interaction is the first observation of a coherent exchange of energy between distant quantum systems in an open space.
Due to the small magnitude of J, the exchange splitting was not detected in elastically scattered radiation. As $J < \Gamma_1$, the peak due to $|ge\rangle$ and $|eg\rangle$ could not be resolved. As we know that the maximum value of J is $\Gamma_1/2$ (see equation (5.62)), the exchange splitting should not be observable in elastically scattered radiation for any system that can be described by (5.43), it can however result in a broadened peak. In the power spectral density, the splitting can only be observed for limited values of the 'observation angle' introduced in equation 5.75. As can be seen in fig. 5.11, the splitting is visible for some angles, but not for all. Another reason that the splitting can be observed in power spectral density is that the width of the resonance fluorescence peak is described by equation 5.70, which is a squared Lorentzian and therefore has half the width of a Lorentzian. The reduced peak width of the power spectrum of a single qubit is the reason for the resolvability of the splitting at low drive powers.

The resonance fluorescence spectrum was also recorded for two qubits tuned into resonance at 6.4 GHz, where $\lambda_r = d$. The results are shown in Fig. 5.14. In this case, except for a Mollow triplet observed at high drive powers, a narrow peak emerges at the frequency both qubits are tuned to. This peak is due to the dark state, which has a much longer life time and therefore a much narrower peak. From fitting with (5.43), we find that the dark state lifetime depends on power, but is always much longer than the bright state lifetime $\Gamma_B/\Gamma_D \geq 100$.

5.2.2 Details of the fitting procedure for power spectral densities

As all of the power spectral densities were measured at powers such that $\Omega \not\ll \Gamma_1$, the full master equation (5.43) had to be used in order to calculate the power spectral densities. For the traces in which the two-qubit

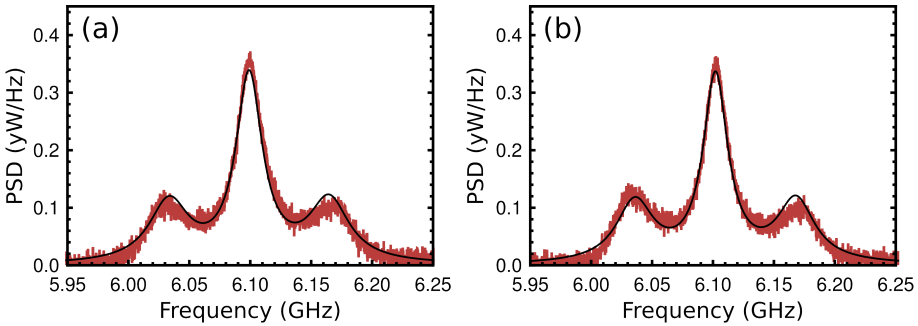

Figure 5.12: Resonance fluorescence spectra for qubit A (a) and B (b) tuned to 6.1 GHz at a drive power of -118 dBm. The continuous black line is a fit with (3.28).

system starts to resemble a Mollow triplet, the third level of the transmon qubit had to be taken into account, while for lower drive powers two levels sufficed. The various parameters needed to calculate the power spectral densities were known from single qubit measurements, except for the non-radiative decay rates for which we only found a weak upper bound. The coupling of the qubits to the transmission line was assumed to be identical for both qubits, and has the value of $g_j = 0.0146$ at 4.8 GHz and 0.0180 at 6.4 GHz, using the definition of coupling as given in equation (5.4). When implementing the fitting routine for resonance fluorescence data, it was found that the power needed in the theoretical fits was not equal to the power used in experiment. A reason for that could be the buildup of the fields between the qubits, which is not taken fully into account due to neglecting the interaction Hamiltonian when finding the effect of qubit k acting on qubit j (see section 5.1.2 for details).

Fitting 4.8 GHz resonance fluorescence measurements

At 4.8 GHz, γ_φ and γ_{nr} where determined from a single resonance fluorescence trace each. They were found to be $\gamma_\varphi/2\pi = 1.8$ MHz and $\gamma_{\mathrm{nr}}/2\pi = 1.2$ MHz. As the raw data were provided for fitting, the y-axis was not rescaled to have physical units, and one trace was used to fit a

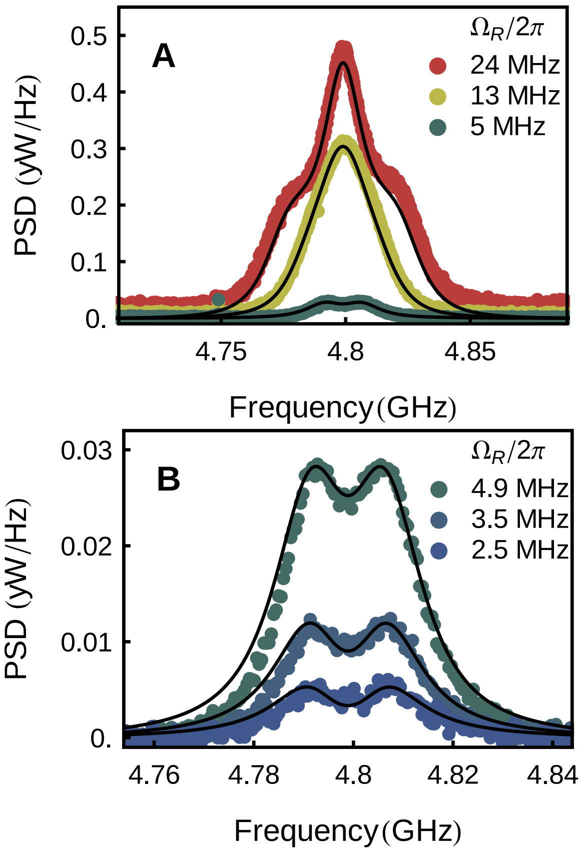

Figure 5.13: The power spectral density of the two-qubit system is measured in transmission for $d = \lambda_r$ at different drive powers. The splitting of the peak at low powers (b) is due to exchange interaction. Solid lines are numerical calculations of which the details are given in section 5.2.2.

global rescaling factor to the fits. Furthermore, as pointed out before, the input power in theory and experiment differed in such a way that it had to be fitted according to $P_{th} = aP_{exp} + b$. Here, we found that $a = 0.68$ and $b = -13.3$ dBm. The reason for the large value of b is still unknown, but is thought to be due to a mistake in one of the calculations. The fact

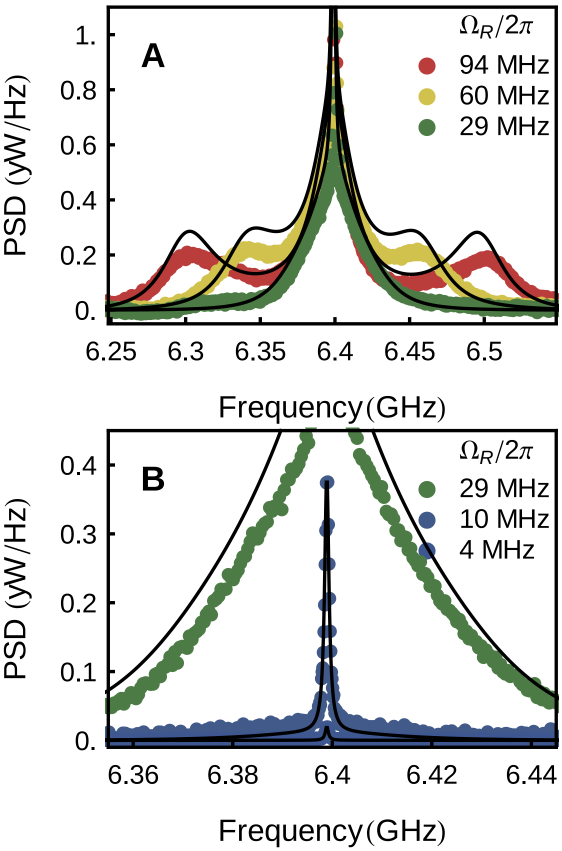

Figure 5.14: The power spectral density for the two-qubit system is measured in reflection for $d = \lambda_r$ at the indicated drive powers. The narrow peak in the center is due to the dark state. The peak due to elastically scattered radiation was removed for clarity. Solid lines are numerical calculations of which the details are given in section 5.2.2.

that $a \neq 0$ could have something to do with the field building up between the two qubits - the ratio between the fields at the qubits differs drastically through the range of powers covered in 5.13. We would like to stress that this explanation is pure speculation. Finally, a free fit parameter is left for the small offsets observed in each power spectral density trace, which are thought to be due to (as yet unknown) details in the experimental setup.

Fitting 6.4 GHz resonance fluorescence measurements

Most of the fitting details for the curves at 6.4 GHz are the same as at 4.8 GHz. An important difference is that γ_{nr} was found to vary linearly with power, and therefore needs two traces to be fitted. The power-dependence of γ_{nr} can be understood as follows. In the fits, the coupling to the line and decay rates for both single qubits are assumed to be equal. Hence only γ_{nr} determines the width of the dark state peak, which is not expected to depend on power. In practice, there is a finite difference between the single qubit decay rates and coupling strengths to the transmission line. These differences open up a drive channel to the dark state as discussed in section 5.1.8. Due to this extra drive channel, the dark state now becomes sensitive to power broadening. The sharp peak is therefore expected to widen with drive power, which is what is observed in the fits and data. The fits find a $\gamma_{\mathrm{nr}}/2\pi$ which varies from 0.17 MHz at the lowest power to 0.59 MHz at the highest power. As this increase of width with power is due to unequal single-qubit decay rates and/or unequal coupling, the lowest value for γ_{nr} should be considered an upper bound on the actual non-radiative decay rate.

The life time of the dark state is given by the width of the narrow peak. As the bright state has a width of 52 MHz, for most drive powers we have that $\Gamma_B/\Gamma_D \geq 100$. The life time of the dark state at low powers is $T_1 \sim 1\,\mu$s, comparable to lifetimes of qubits in circuit QED, and it is expected that higher dark state lifetimes are achievable by making sure the qubits are more similar and are subject to the same electromagnetic environment by eliminating weak standing modes in the experimental setup. A single trace was fitted to determine the pure dephasing rate, which was found to be $\gamma_\varphi/2\pi = 0.2$ MHz. Pure dephasing is therefore much less significant than at 4.8 GHz, as expected. The power used in theory was fitted as $P_{th} = aP_{exp} + b$, with $a = 1$ and $b = 1.6$ dBm. Offsets on the power spectral density traces were again left as free fit parameters.

5.2.3 Two-qubit interactions versus distance

It was found that the dark state could be observed separately when subtracting single-qubit Mollow triplets for each qubit from the two-qubit Mollow triplets. In chapter 4 we found that that when driving a two-qubit system, the qubits will not both see a drive power equal to the input power. Similarly, to isolate the dark state, we have to subtract single-qubit Mollow triplets measured at different powers from the two-qubit Mollow triplet. The difference between these drive powers depends on the frequency of both qubits compared to the distance between them and on the magnitude of the input power. In Fig. 5.15, we show the result of subtracting two separately measured spectra from a two-qubit spectrum. By repeating this procedure, we can observe how the dark state peak behaves as a function of power (Fig. 5.16).

The dark state peak can also be observed as a function of frequency. The dark state is expected to be 'most dark', or most protected from relaxation, when $\lambda_r = d$, and therefore will be narrowest at the corresponding qubit

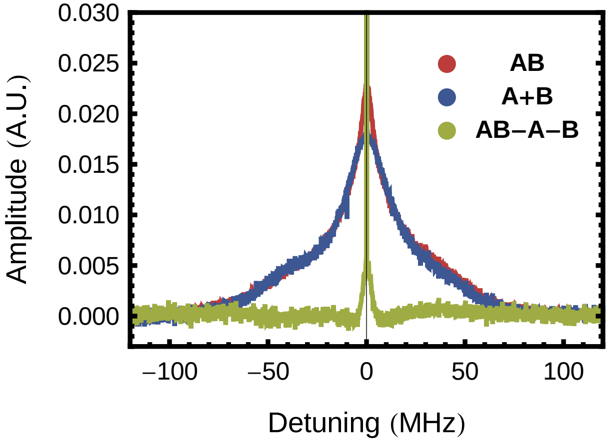

Figure 5.15: The resonance fluorescence spectrum of both qubits A and B in resonance, of qubit A and B measured separately and superimposed afterwards, and of the difference between these. This plot was done at 6.1 GHz, where the dark state is clearly visible but not very narrow.

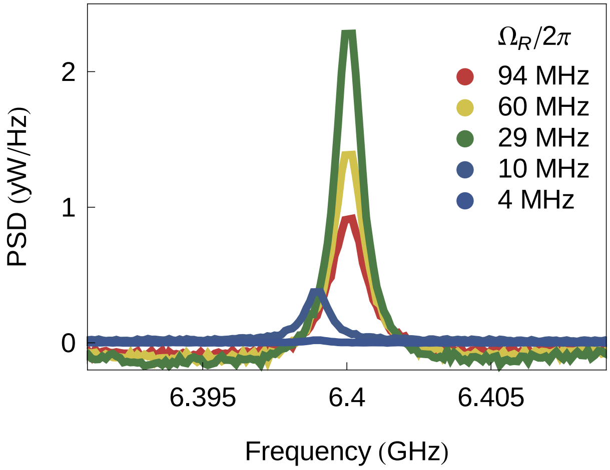

Figure 5.16: The dark state peak at the indicated drive powers, which were chosen to be the same as in 5.14. From comparing the y-axes of these figures, it can be seen that the dark state peak is much higher than the bright state Mollow triplet. As the center of the dark state coincides with the coherently scattered peak, which was removed by setting it equal to the average of the two neighbouring points, it is not possible to see the full height of the dark state peak. The two low-power traces were measured separately at a slightly different frequency.

frequencies. If we assume the population of the dark state to vary slowly around this frequency, the total power in the dark state peak will also vary slowly. The dark state peak will then be highest when its life time is longest. Therefore, by finding the qubit frequency at which the dark state peak is highest, we can confirm the value of d. The measurements for this are shown in 5.17, and we find that $d \sim 6.4$ GHz.

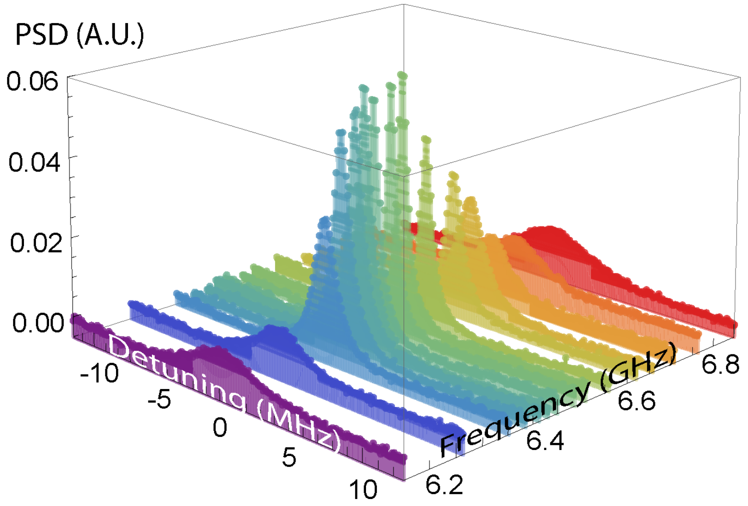

Figure 5.17: The dark state peak shape varies as the frequency of the two resonant qubits is varied across the frequency commensurate to their distance.

6 Outlook

The work presented in this thesis is the first step into the world of many-qubit waveguide QED. A host of experiments is possible, and several very interesting experiments are well within the reach of current quantum technology.

Starting with the basics, an experiment which should be carried out is to measure the reflection of single photons off a qubit in a transmission line. So far, while a single photon router has been claimed to be implemented [Hoi11], only weak coherent tones were scattered off qubits. But as can be seen from the derivation of r in section 3.1, the high reflection coefficient is obtained when solving the optical Bloch equations for a steady state under a continuous drive. How a single qubit scatters a single photon has not yet been experimentally investigated, and is of the utmost importance for using the qubits as single-photon mirrors in a quantum communication or computing context.

More interestingly, the scaling of the lifetime of the dark state with the number of qubits in the system should be investigated in the context of decoherence-free subspaces. Similarly, second order correlation functions should be measured to investigate the properties of both the dark and the bright state. A state in an open system which has a lifetime orders of magnitude higher than other states might have applications for both quantum communication and quantum computing.

Another phenomenon that should be investigated in a waveguide QED system is stimulated emission. To measure stimulated emission, the population of the qubits) must be inverted, after which a resonant photon is sent into the transmission line. For a single artificial atoms, stimulated emission has been shown to occur in a proof-of-principle experiment in [Astafiev10b]. It would be interesting to investigate the properties of the radiation emerging due to stimulated emission from a multi-qubit system. Depending on the coherence properties of the emerging radiation, such a system might prove useful as a multi-photon source, which could again be used to study

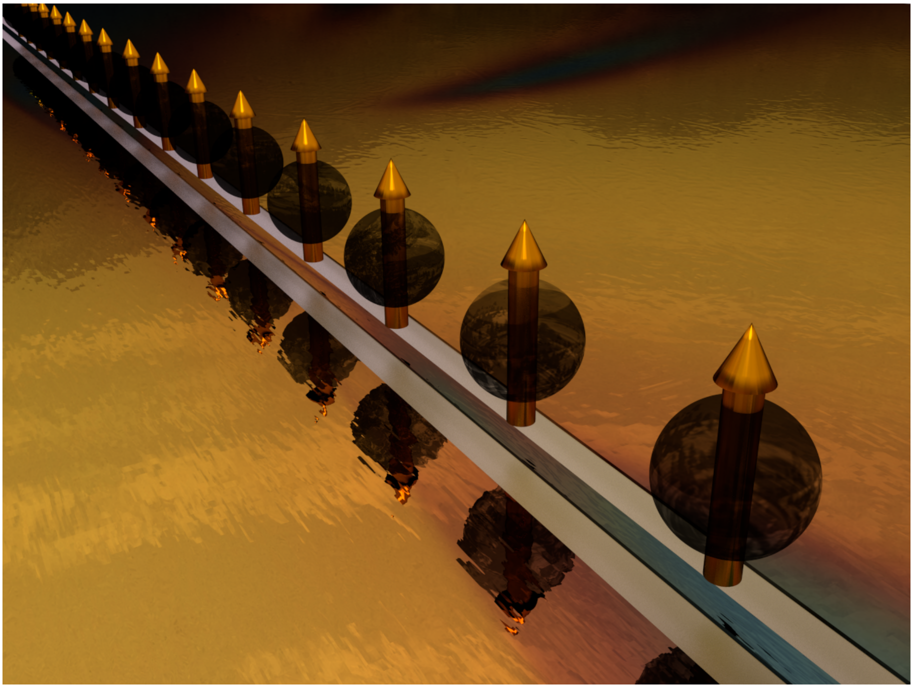

Figure 6.1: Many qubits in a transmission line coupling to a field.

the strong photon-photon correlations produced by scattering a two-photon state off an artificial atom in one dimension [Zheng10, Zheng12c].

There has been a proposal for a quantum memory using waveguide QED [Leung12]. This proposal is based on multiple (at least a dozen) distant qubits in a transmission line, driving a strong pump tone at the transition of first to second excited state to make the qubits transparent (EIT), and then switching the transparency off when a photon which we want to store is located in the qubit grid. The photon can then be released again by switching the transparency of the qubits back on.

Finally, a proposal was published to use waveguide-QED to implement a Quantum Computer using photons as flying qubits [Zheng12d], using four-level atoms to perform gates on the flying qubits, and three-level systems as single-photon routers.

Bibliography

[Abdumalikov10] A. A. Abdumalikov, O. Astafiev, A. M. Zagoskin, Y. A. Pashkin, Y. Nakamura, and J. S. Tsai. "Electromagnetically induced transparency on a single artificial atom." *Phys. Rev. Lett.*, **104**, 193601 (2010). 7, 21, 71

[Abdumalikov11] A. A. Abdumalikov, O. V. Astafiev, Y. A. Pashkin, Y. Nakamura, and J. S. Tsai. "Dynamics of coherent and incoherent emission from an artificial atom in a 1d space." *Phys. Rev. Lett.*, **107**, 043604 (2011). 21, 71

[Astafiev10a] O. Astafiev, A. M. Zagoskin, A. A. Abdumalikov Jr., Y. A. Pashkin, T. Yamamoto, K. Inomata, Y. Nakamura, and J. S. Tsai. "Resonance fluorescence of a single artificial atom." *Science*, **327**, 840–843 (2010). 7, 20, 21, 49, 56, 68, 71, 79

[Astafiev10b] O. V. Astafiev, A. A. Abdumalikov, A. M. Zagoskin, Y. A. Pashkin, Y. Nakamura, and J. S. Tsai. "Ultimate on-chip quantum amplifier." *Phys. Rev. Lett.*, **104**, 183603 (2010). 133

[Bell64] J. S. Bell. "On the Einstein Podolsky Rosen paradox." *Physics (N. Y.)*, **1**, 195 (1964). 2

[Bouchiat98] V. Bouchiat, D. Vion, P. Joyez, D. Esteve, and M. H. Devoret. "Quantum coherence with a single Cooper pair." *Phys. Scr.*, **T76**, 165–170 (1998). 11

[Bozyigit11] D. Bozyigit, C. Lang, L. Steffen, J. M. Fink, C. Eichler, M. Baur, R. Bianchetti, P. J. Leek, S. Filipp, M. P.

da Silva, A. Blais, and A. Wallraff. “Antibunching of microwave-frequency photons observed in correlation measurements using linear detectors.” *Nat. Phys.*, **7**, 154–158 (2011). 7

[Breuer02] H. P. Breuer and F. Petruccione. *The theory of open quantum systems*. Oxford University Press (2002). 55

[Büttiker87] M. Büttiker. “Zero-current persistent potential drop across small-capacitance Josephson junctions.” *Phys. Rev. B*, **36**, 3548–3555 (1987). 11

[Bylander11] J. Bylander, S. Gustavsson, F. Yan, F. Yoshihara, K. Harrabi, G. Fitch, D. G. Cory, Y. Nakamura, J.-S. Tsai, and O. W. D. “Noise spectroscopy through dynamical decoupling with a superconducting flux qubit.” *Nat. Phys.*, **7**, 565–570 (2011). 111

[Caldeira83] A. O. Caldeira and A. J. Leggett. “Quantum tunnelling in a dissipative system.” *Annals of Physics*, **149**, 374–456 (1983). 33

[Chang07] D. E. Chang, A. S. Sorensen, E. A. Demler, and M. D. Lukin. “A single-photon transistor using nanoscale surface plasmons.” *Nat. Phys.*, **3**, 807–812 (2007). 65

[Clarke08] J. Clarke and F. K. Wilhelm. “Superconducting quantum bits.” *Nature*, **453**, 1031–1042 (2008). 3

[Clerk10] A. A. Clerk, M. H. Devoret, S. M. Girvin, F. Marquardt, and R. J. Schoelkopf. “Introduction to quantum noise, measurement, and amplification.” *Rev. Mod. Phys.*, **82**, 1155–1208 (2010). 107

[Cooley65] J. W. Cooley and J. W. Tukey. “An Algorithm for the Machine Calculation of Complex Fourier Series.” *Mathematics of Computation*, **19**, 297–301 (1965). 46

[Cottet02] A. Cottet, D. Vion, A. Aassime, P. Joyez, D. Esteve, and M. H. Devoret. “Implementation of a combined charge-phase quantum bit in a superconducting circuit.” *Physica C*, **367**, 197–203 (2002). 14

[deGroot10] P. C. de Groot, J. Lisenfeld, R. N. Schouten, S. Ashhab, A. Lupaşcu, C. J. P. M. Harmans, and J. E. Mooij. “Selective darkening of degenerate transitions demonstrated with two superconducting quantum bits.” *Nat. Phys.*, **6**, 763– 766 (2010). 111

[DeVoe96] R. G. DeVoe and R. G. Brewer. “Observation of superradiant and subradiant spontaneous emission of two trapped ions.” *Phys. Rev. Lett.*, **76**, 2049–2052 (1996). 21, 110

[Devoret97] M. H. Devoret. “Quantum fluctuations in electrical circuits.” In S. Reynaud, E. Giacobino, and J. Zinn-Justin, editors, “Quantum Fluctuations: Les Houches Session LXIII,” 351–386. Elsevier (1997). 33, 94

[Doherty13] M. W. Doherty, N. B. Manson, P. Delaney, F. Jelezko, J. Wrachtrup, and L. C. Hollenberg. “The nitrogen-vacancy colour centre in diamond.” *Physics Reports*, **528**, 1–45 (2013). 3

[Eichler11] C. Eichler, D. Bozyigit, C. Lang, L. Steffen, J. Fink, and A. Wallraff. “Experimental state tomography of itinerant single microwave photons.” *Phys. Rev. Lett.*, **106**, 220503–4 (2011). 7

[Einstein35] A. Einstein, B. Podolsky, and N. Rosen. “Can quantum-mechanical description of physical reality be considered complete?” *Phys. Rev.*, **47**, 777–780 (1935). 4

[Fang13] Y. L. Fang, H. Zheng, and H. U. Baranger. “One-dimensional waveguide coupled to multiple qubits: Photon-photon correlations.” *arXiv:1308.6551* (2013). 92

[Feynman82] R. P. Feynman. “Simulating physics with computers.” *Int. J. Theor. Phys.*, **21**, 467–488 (1982). 6

[Filipp11] S. Filipp, A. F. van Loo, M. Baur, L. Steffen, and A. Wallraff. “Preparation of subradiant states using local qubit control in circuit qed.” *Phys. Rev. A*, **84**, 061805 (2011). 111

[Fragner08] A. Fragner, M. Göppl, J. M. Fink, M. Baur, R. Bianchetti, P. J. Leek, A. Blais, and A. Wallraff. “Resolving vacuum fluctuations in an electrical circuit by measuring the Lamb shift.” *Science*, **322**, 1357–1360 (2008). 7

[Gardiner85] C. W. Gardiner and M. J. Collett. “Input and output in damped quantum systems: Quantum stochastic differential equations and the master equation.” *Phys. Rev. A*, **31**, 3761–3774 (1985). 106

[Gauss66] C. F. Gauss. *Carl Friedrich Gauss, Werke, Band 3*. Königlichen Gesellschaft der Wissenschaften (1866). 46

[Gödel31] Gödel. “über formal unentscheidbare sätze der principia mathematica und verwandter systeme, i.” *Monatshefte für Mathematik und Physik*, **38**, 173–98 (1931). 1

[González-Tudela13] A. González-Tudela and D. Porras. “Mesoscopic entanglement induced by spontaneous emission in solid-state quantum optics.” *Phys. Rev. Lett.*, **110**, 080502 (2013). 110

[Grover96] L. K. Grover. “A fast quantum mechanical algorithm for database search.” In “Proceedings of the twenty-eighth annual ACM symposium on Theory of computing,” 212–219. ACM, Philadelphia, Pennsylvania, United States (1996). 5

[Gustavsson11] S. Gustavsson, J. Bylander, F. Yan, W. D. Oliver, F. Yoshihara, and Y. Nakamura. "Noise correlations in a flux qubit with tunable tunnel coupling." *Phys. Rev. B*, **84**, 014525– (2011). 111

[Hanson08] R. Hanson and D. D. Awschalom. "Coherent manipulation of single spins in semiconductors." *Nature*, **453**, 1043–1049 (2008). 3

[Haroche89] S. Haroche and D. Kleppner. "Cavity quantum electrodynamics." *Physics Today*, 24 (1989). 17

[Harrow09] A. W. Harrow, A. Hassidim, and S. Lloyd. "Quantum algorithm for linear systems of equations." *Phys. Rev. Lett.*, **103**, 150502 (2009). 5

[Hoi11] I.-C. Hoi, C. M. Wilson, G. Johansson, T. Palomaki, B. Peropadre, and P. Delsing. "Demonstration of a single-photon router in the microwave regime." *Phys. Rev. Lett.*, **107**, 073601– (2011). 21, 56, 62, 71, 133

[Hoi12] I.-C. Hoi, T. Palomaki, J. Lindkvist, G. Johansson, P. Delsing, and C. M. Wilson. "Generation of nonclassical microwave states using an artificial atom in 1D open space." *Phys. Rev. Lett.*, **108**, 263601– (2012). 21, 71

[Hoi13a] I.-C. Hoi, A. F. Kockum, T. Palomaki, T. M. Stace, B. Fan, L. Tornberg, S. R. Sathyamoorthy, G. Johansson, P. Delsing, and C. M. Wilson. "Giant cross-kerr effect for propagating microwaves induced by an artificial atom." *Phys. Rev. Lett.*, **111**, 053601– (2013). 21, 71

[Hoi13b] I.-C. Hoi, C. M. Wilson, G. Johansson, J. Lindkvist, B. Peropadre, T. Palomaki, and P. Delsing. "Microwave quantum optics with an artificial atom in one-dimensional open space." *New J. Phys.*, **15**, 025011 (2013). 71

[Jaynes63] E. Jaynes and F. Cummings. "Comparison of quantum and semiclassical radiation theories with application to the beam maser." **51**, 89–109 (1963). 18

[Jordan12] S. P. Jordan, K. S. M. Lee, and J. Preskill. "Quantum algorithms for quantum field theories." *Science*, **336**, 1130–1133 (2012). 6

[Josephson62] B. D. Josephson. "Possible new effects in superconductive tunnelling." *Physics Letters*, **1**, 251–253 (1962). 7

[Koch07] J. Koch, T. M. Yu, J. Gambetta, A. A. Houck, D. I. Schuster, J. Majer, A. Blais, M. H. Devoret, S. M. Girvin, and R. J. Schoelkopf. "Charge-insensitive qubit design derived from the Cooper pair box." *Phys. Rev. A*, **76**, 042319 (2007). 11, 15, 17, 52, 59, 93, 94

[Kok07] P. Kok, W. J. Munro, K. Nemoto, T. C. Ralph, J. P. Dowling, and G. J. Milburn. "Linear optical quantum computing with photonic qubits." *Rev. Mod. Phys.*, **79**, 135–174 (2007). 3

[Koshino13] K. Koshino, H. Terai, K. Inomata, T. Yamamoto, W. Qiu, Z. Wang, and Y. Nakamura. "Observation of the three-state dressed states in circuit quantum electrodynamics." *Phys. Rev. Lett.*, **110**, 263601– (2013). 71

[Lalumière13] K. Lalumière, B. C. Sanders, A. F. van Loo, A. Fedorov, A. Wallraff, and A. Blais. "Input-output theory for waveguide qed with an ensemble of inhomogeneous atoms." *Phys. Rev. A*, **88**, 043806 (2013). 91, 92, 94, 96, 104, 108, 112, 113, 116, 117, 120, 122

[Lang11] C. Lang. "Model for measuring correlation functions." Technical report (2011). Email Okt. '11. 42

[Lang13] C. Lang, C. Eichler, L. Steffen, J. M. Fink, M. J. Woolley, A. Blais, and A. Wallraff. "Correlations, indistinguishability and entanglement in Hong-Ou-Mandel experiments at microwave frequencies." *Nat. Phys.*, **9**, 345–348 (2013). 7

[Lehmberg70] R. H. Lehmberg. "Radiation from an n-atom system. i. general formalism." *Phys. Rev. A*, **2**, 883– (1970). 91, 92, 94

[Leung12] P. M. Leung and B. C. Sanders. "Coherent control of microwave pulse storage in superconducting circuits." *arXiv:1205.0637* (2012). 134

[Lloyd13] S. Lloyd, M. Mohseni, and P. Rebentrost. "Quantum algorithms for supervised and unsupervised machine learning." *arXiv:1307.0411* (2013). 5

[Loudon00] R. Loudon. *The Quantum Theory of Light.* Oxford U (2000). 43, 68, 99

[Manucharyan09] V. E. Manucharyan, J. Koch, L. I. Glazman, and M. H. Devoret. "Fluxonium: Single cooper-pair circuit free of charge offsets." *Science*, **326**, 113–116 (2009). 11

[Mollow69] B. R. Mollow. "Power spectrum of light scattered by two-level systems." *Phys. Rev.*, **188**, 1969–1975 (1969). 68

[Motzoi09] F. Motzoi, J. M. Gambetta, P. Rebentrost, and F. K. Wilhelm. "Simple pulses for elimination of leakage in weakly nonlinear qubits." *Phys. Rev. Lett.*, **103**, 110501 (2009). 15

[Nielsen00] M. A. Nielsen and I. L. Chuang. *Quantum Computation and Quantum Information.* Cambridge University Press (2000). 3, 6

[Oppenheim97] A. S. Oppenheim, A. S. Willsky, and S. H. Nawab. *Signals and Systems.* Prentice Hall (1997). 46

[Orlando99]	T. P. Orlando, J. E. Mooij, L. Tian, C. H. van der Wal, L. S. Levitov, S. Lloyd, and J. J. Mazo. "Superconducting persistent-current qubit." *Phys. Rev. B*, **60**, 15398– (1999). 11
[Paik11]	H. Paik, D. I. Schuster, L. S. Bishop, G. Kirchmair, G. Catelani, A. P. Sears, B. R. Johnson, M. J. Reagor, L. Frunzio, L. I. Glazman, S. M. Girvin, M. H. Devoret, and R. J. Schoelkopf. "Observation of high coherence in Josephson junction qubits measured in a three-dimensional circuit QED architecture." *Phys. Rev. Lett.*, **107**, 240501 (2011). 19
[Pechal13]	M. Pechal, C. Eichler, S. Zeytinoglu, S. Berger, A. Wallraff, and S. Filipp. "Microwave-controlled generation of shaped single photons in circuit quantum electrodynamics." *arXiv:1308.4094* (2013). 7
[Peropadre13]	B. Peropadre, J. Lindkvist, I.-C. Hoi, C. M. Wilson, J. J. Garcia-Ripoll, P. Delsing, and G. Johansson. "Scattering of coherent states on a single artificial atom." *New J. Phys.*, **15**, 035009 (2013). 49
[Pozar93]	D. M. Pozar. *Microwave Engineering*. Addison-Wesley Publishing Company (1993). 50
[Purcell46]	E. M. Purcell. "Spontaneous emission probabilties at radio frequencies." *Phys. Rev.*, **69**, 681 (1946). 18
[Rebentrost13]	P. Rebentrost, M. Mohseni, and S. Lloyd. "Quantum support vector machine for big feature and big data classification." *arXiv:1307.0471* (2013). 5
[Rigetti12]	C. Rigetti, J. M. Gambetta, S. Poletto, B. L. T. Plourde, J. M. Chow, A. D. Córcoles, J. A. Smolin, S. T. Merkel, J. R. Rozen, G. A. Keefe, M. B. Rothwell, M. B. Ketchen, and M. Steffen. "Superconducting qubit in a waveguide cavity with a coherence time approaching 0.1 ms." *Phys. Rev. B*, **86**, 100506 (2012). 20

[Ritsch13] H. Ritsch, P. Domokos, F. Brennecke, and T. Esslinger. "Cold atoms in cavity-generated dynamical optical potentials." *Rev. Mod. Phys.*, **85**, 553–601 (2013). 3

[Sakurai10] J. J. Sakurai and J. J. Napolitano. *Modern quantum mechanics*. Addison-Wesley, 2nd edition (2010). 53

[Salathé11] Y. Salathé. *Towards Gigahertz Bandwidth Digital Signal Processing in Circuit Quantum Electrodynamics*. Master's thesis, ETH Zurich (2011). 47

[Scully97] M. O. Scully and M. S. Zubairy. *Quantum Optics*. Cambridge University Press (1997). 43, 68

[Shen05a] J. T. Shen and S. Fan. "Coherent photon transport from spontaneous emission in one-dimensional waveguides." *Opt. Lett.*, **30**, 2001–2003 (2005). 76, 78

[Shen05b] J.-T. Shen and S. Fan. "Coherent single photon transport in a one-dimensional waveguide coupled with superconducting quantum bits." *Phys. Rev. Lett.*, **95**, 213001– (2005). 20, 76, 78, 79, 93

[Shor97] P. W. Shor. "Polynomial-time algorithms for prime factorization and discrete logarithms on a quantum computer." *SIAM Journal on Scientific and Statistical Computing*, **26**, 1484 (1997). 4

[Srinivasan13] S. J. Srinivasan, N. M. Sundaresan, D. Sadri, Y. Liu, J. M. Gambetta, T. Yu, S. M. Girvin, and A. A. Houck. "Time-reversal symmetrization of spontaneous emission for high fidelity quantum state transfer." *arXiv:1308.3471* (2013). 7

[Steffen13] L. Steffen, Y. Salathe, M. Oppliger, P. Kurpiers, M. Baur, C. Lang, C. Eichler, G. Puebla-Hellmann, A. Fedorov, and A. Wallraff. "Deterministic quantum teleportation with feed-forward in a solid state system." *Nature*, **500**, 319–322 (2013). 20

[Tavis68] M. Tavis and F. W. Cummings. “Exact solution for an N-molecule-radiation-field Hamiltonian.” *Phys. Rev.*, **170**, 379–384 (1968). 18

[Tinkham96] M. Tinkham. *Introduction to Superconductivity*. McGraw-Hill International Editions (1996). 3, 9

[vanLoo13] A. van Loo, A. Fedorov, K. Lalumière, B. Sanders, A. Blais, and A. Wallraff. “Photon-mediated interactions between distant artificial atoms.” *Science*, **342**, 1494–1496 (2013). 57, 123

[Wallraff04] A. Wallraff, D. I. Schuster, A. Blais, L. Frunzio, R.-S. Huang, J. Majer, S. Kumar, S. M. Girvin, and R. J. Schoelkopf. “Strong coupling of a single photon to a superconducting qubit using circuit quantum electrodynamics.” *Nature*, **431**, 162–167 (2004). 7, 11

[Walls08] D. F. Walls and G. J. Milburn. *Quantum Optics*. Springer Verlag, Berlin, 2nd edition (2008). 114

[Wendin05] G. Wendin and V. Shumeiko. “Superconducting quantum circuits, qubits and computing.” *arXiv:cond-mat/0508729* (2005). 11

[Xilinx11] Xilinx. *Xilinx LogiCORE IP Fast Fourier Transform v7.1*. Xilinx (2011). 47

[Yamamoto99] Y. Yamamoto and A. Imamoğlu. *Mesoscopic Quantum Optics*. Wiley (1999). 43, 44, 68

[Yoshihara10] F. Yoshihara, Y. Nakamura, and J. S. Tsai. “Correlated flux noise and decoherence in two inductively coupled flux qubits.” *Phys. Rev. B*, **81**, 132502– (2010). 111

[Zheng10] H. Zheng, D. J. Gauthier, and H. U. Baranger. “Waveguide qed: Many-body bound-state effects in coherent and fock-state scattering from a two-level system.” *Phys. Rev. A*, **82**, 063816 (2010). 92, 134

[Zheng12a] H. Zheng and H. U. Baranger. "Persistent quantum beats and long-distance entanglement from non-markovian processes." *arXiv:1206.4442v1* (2012). 96

[Zheng12b] H. Zheng, D. J. Gauthier, and H. U. Baranger. "Decoy-state quantum key distribution with nonclassical light generated in a one-dimensional waveguide." *arXiv:1210.1113* (2012). 92

[Zheng12c] H. Zheng, D. J. Gauthier, and H. U. Baranger. "Strongly correlated photons generated by coupling a three- or four-level system to a waveguide." *Phys. Rev. A*, **85**, 043832 (2012). 92, 134

[Zheng12d] H. Zheng, D. J. Gauthier, and H. U. Baranger. "Waveguide-qed-based photonic quantum computation." *arXiv:1211.1711* (2012). 92, 134

[Zheng13] H. Zheng and H. U. Baranger. "Persistent quantum beats and long-distance entanglement from waveguide-mediated interactions." *Phys. Rev. Lett.*, **110**, 113601 (2013). 92

List of Publications

1. **A. F. van Loo**, A. Fedorov, K. Lalumière, B. C. Sanders, A. Blais and A. Wallraff, *Photon-mediated interactions between distant artificial atoms*, Science **342**, 6165 (2013).
2. K. Lalumière, B. C. Sanders, **A. F. van Loo**, A. Fedorov, A. Wallraff, and A. Blais, *Input-output theory for waveguide QED with an ensemble of inhomogeneous atoms*, Physical Review A **88**, 043806 (2013).
3. J. A. Mlynek, A. A. Abdumalikov, J. M. Fink, L. Steffen, M. Baur, C. Lang, **A. F. van Loo** and A. Wallraff, *Demonstrating W-type entanglement of Dicke states in resonant cavity quantum electrodynamics*, Physical Review A **86**, 053838 (2012).
4. S. Filipp, **A. F. van Loo**, M. Baur, L. Steffen and A. Wallraff, *Preparation of subradiant states using local qubit control in circuit QED*, Physical Review A **84**, 061805 (2011).
5. P. C. de Groot, **A. F. van Loo**, J. Lisenfeld, R. N. Scouten, A. Lupaşcu, C. J. P. M. Harmans and J. E. Mooij, *Low-crosstalk bifurcation detectors for coupled flux qubits*, Applied Physics Letters **96**, 123508 (2010).

Acknowledgements

Science is, on the whole, an informal activity, a life of shirt sleeves and coffee served in beakers. - George Porter

A PhD thesis is written by one author, but a PhD is not done alone. During the course of my PhD there have been many people who helped to make life – be it work or leisure – more easy and more fun.

My first task in the lab was to prepare for and install a new Triton dilution system. Romeo, being experienced in everything fridge-related, was of invaluable help with that. My first experiments were done under the guidance of Matthias, who introduced me to the black art of Cleansweep. Soon afterwards I joined an experiment with Stefan on preparing subradiant states, which I enjoyed a lot. After a few discussions about possible next projects with Andreas, I decided on the project discussed in this thesis. I thank Andreas for giving me the freedom to not only let me choose my project, but also for giving me much freedom in choosing how to do it. During this project I could rely on Arkady for advice when I got stuck. Also of invaluable help were Christian and Yves, who developed FPGA firmware I needed for my experiments. The fact that I almost never needed to ask for help when it was implemented is a testament to the great job you did. A quantitative explanation of the data would not have been possible without the hard work of Kevin Lalumière, Alexandre Blais and Barry Sanders.

During my PhD I inhabited several offices (D11, D5, D17, D19 and G7) . I started in D11 with Stefan and Simon, where I enjoyed many long physics discussions. After a very short stint in D5, I spent most of my PhD in legendary office D17, which had more or less everything one could wish for in an office, including coffee breaks and random sounds. I would like to specifically mention the ‘core’ of D17, who contributed most to making it a great place to be: ‘screwmaster’ TobidoT who never managed to get rid of his fruit salad, Simon the amazing linguist and fan of everything Japanese or Korean, Marek the great sage who can explain everything but is nerd-

sniped so easily, Anna the assistant kicker, and honorary member Lars. Apart from making D17 such a great place, this team (helped at times by Yves and Farruh) also managed to win the AMP PubQuiz four times in a row, i.e., every time we participated. The running breaks in any weather with Simon and Arkady, and occasionally Lars and Marek, helped to refresh the mind when bogged down with Mathematica problems or problematic experimental setups.
During the writing of this thesis, Arkady, Marek and Simon helped me by proofreading the first and second versions. Tobias provided me with a German translation of the abstract.
During my stay in Switzerland, I have had a lot of help from Gaby in navigating the confusing waters of Swiss buraucracy.
Outside of the lab, my roommates helped me enjoy the nonscientific parts of life. Stassos, Uli, Mandy and Marek helped me enjoy life out of the lab. Susanna has been especially skillful at helping me relax by instigating balcony dinners, numerous excursions into the Limmat, and many other things. Finally, I would like to thank my family for being so quick in learning that 'How much longer until your PhD is done' and similar questions should never be asked, especially late in the PhD, and for not holding my rather spartan communication style against me.
To all the people mentioned above, and to those I forgot to mention explicitly: you have my gratitude. These 4+ years would not have been the same without you.

ETH zürich

Diss. ETH No. 21838